Development and Testing of a Polycentric Knee Joint for Powered Walking Assist Exoskeletons

Émélie Séguin

Thesis submitted to the University of Ottawa

in partial fulfillment of the requirements for the

Master of Applied Science in Biomedical Engineering

Ottawa – Carleton Institute for Biomedical Engineering

Department of Mechanical Engineering

Faculty of Engineering

University of Ottawa

ABSTRACT

Loss of mobility and independence directly affects the quality of life of many vulnerable individuals. To address this, researchers have developed wearable walking assist exoskeletons to aid users with their daily activities. While this technology has advanced tremendously in the past decade, current exoskeletons cause discomfort and injuries to the user, leading to device rejection.

This research intends to develop a kinematically compatible knee joint suitable for exoskeletons. The proposed knee design can be adapted to accommodate an offset and optimize force delivery. This is achieved by ensuring that the mechanical and biological joint rotation axes are aligned and that the moment arm varies throughout flexion. Model simulations and mechanical testing of fabricated prototypes were achieved to analyze and validate the design. The results confirm the kinematic compatibility of the design and that the moment arm could be varied throughout flexion to achieve optimal and effective moment transfer.

ACKNOWLEDGEMENTS

This work would not have been possible without the support I have received from so many people. Firstly, I want to thank Dr. Marc Doumit for supervising and reviewing this work from beginning to end. Thank you to my parents for being excited for me whenever I make the smallest bit of progress and for getting me this far. Thank you to Nathan for always being there for all my highs and lows, and for agreeing to bring a puppy into our lives in the middle of it all. Freyja, (though I know she will never read this since she is the puppy in question), thank you for getting me outside every day and ensuring that I never go a day without laughter and lots of kisses. Amanda, thank you for bringing me positive energy when I need it and for making stay-at-home quarantine so much more fun. Thank you to the University of Ottawa and the Natural Sciences and Engineering Research Council of Canada for the financial support. I am more grateful than any of you will ever know.

Table of Contents

List of Figures

List of Tables

Nomenclature

Symbol	Units	Definition
γ	°, degrees	rotation of offset exoskeleton brace
θ	°, degrees	knee flexion in degrees
θ_2	°, degrees	angle between the $d_{1\rightarrow2}$ vector and the y-axis
θ_3	°, degrees	angle between the $d_{1\rightarrow3}$ vector and the y-axis
θ_{rotate}	°, degrees	rotation angle for images in MATLAB
ACL	N/A	anterior cruciate ligament
$d_{1\rightarrow2}$	mm	distance from pin 1 to pin 2
$d_{1\rightarrow3}$	mm	distance from pin 1 to pin 3
$d_{experimental}$	mm	distance from the experimental pin center to the origin
$d_{theoretical}$	mm	distance from the theoretical pin center to the origin
DOF	N/A	degree of freedom
F	°, degrees	flexion angle
ICR	N/A	instantaneous center of rotation
L	mm	displacement of brace on offset exoskeleton
M	mm	magnitude of moment arm
M_M	mm	magnitude of moment arm of the offset joint
PCL	N/A	posterior cruciate ligament
PLA	N/A	polylactic acid
r	mm	radius of gears in Double-Hinge Gear Joint
ROM	N/A	range of motion
S	mm/pixels	ratio of mm to pixels in image
T	Nm	applied torque
w_f	mm	width of the femoral component
WAE	N/A	walking assist exoskeleton
x	N/A	horizontal axis
x_1	mm	translation of the ICR in the anterior-posterior direction x-coordinate for path i = 1,2,3 for no offset
$x_{contact}$	pixels	x-coordinate of last point of contact between cable and pulley
$x_{contact\ new}$	mm	$x_{contact}$ translated and normalized

$x_{hinge\ ICR}$	mm	x coordinate of the ICR of the Double-Hinge Gear Joint
$x_{i\ pin}$	pixels	x-coordinate of pin i = 1,2,3 from image identified in MATLAB
$x_{i\ pin\ new}$	mm	x-coordinate of pin i = 1,2,3 translated and normalized
$x_{i\ Diff}$	mm	x-coordinate of pins i = 2,3 with respect to pin 1 for no offset
$x_{i\ Diff\ M}$	mm	x-coordinate of pins i = 1,2,3 at 0° flexion for the offset joint
x_{iM}	mm	x-coordinate for paths i = 1,2,3 for the offset joint
x_{p1}	mm	x-coordinate for the first iteration of the pulley shape
x_{p2}	mm	x-coordinate for the final pulley shape
x_{pM}	mm	x-coordinate for the final offset pulley shape
x_{TL}	pixels	x-coordinate of the top left corner identified in MATLAB
x_{TLnew}	pixels	x-coordinate of the top left corner after rotation by θ_{rotate}
x_{TR}	pixels	x-coordinate of the top right corner identified in MATLAB
x_{TRnew}	pixels	x-coordinate of the top right corner after rotation by θ_{rotate}
y	N/A	vertical axis
y_1	mm	translation of the ICR in the proximal-distal direction y-coordinate for path i = 1,2,3 for no offset
$y_{contact}$	pixels	y-coordinate of last point of contact between cable and pulley
$y_{contact\ new}$	mm	$y_{contact}$ translated and normalized
$y_{hinge\ ICR}$	mm	y coordinate of the ICR of the Double-Hinge Gear Joint
$y_{i\ pin}$	pixels	y-coordinate of pin i = 1,2,3 from image identified in MATLAB
$y_{i\ pin\ new}$	mm	y-coordinate of pin i = 1,2,3 translated and normalized
$y_{i\ Diff}$	mm	y-coordinate of pins i = 2,3 with respect to pin 1 for no offset
$y_{i\ Diff\ M}$	mm	y-coordinate of pins i = 1,2,3 at 0° flexion for the offset joint
y_{iM}	mm	y-coordinate for paths i = 1,2,3 for the offset joint
y_{p1}	mm	y-coordinate for the first iteration of the pulley shape
y_{p2}	mm	y-coordinate for the final pulley shape
y_{pM}	mm	y-coordinate for the final offset pulley shape
y_{TL}	pixels	y-coordinate of the top left corner identified in MATLAB
y_{TLnew}	pixels	y-coordinate of the top left corner after rotation by θ_{rotate}

y_{TR}	pixels	y-coordinate of the top right corner identified in MATLAB
y_{TRnew}	pixels	y-coordinate of the top left corner after rotation by θ_{rotate}
Y_{DIS}	mm	distal-proximal translation of the ICR
Z_{DIS}	mm	anterior-posterior translation of the ICR
% error	%	percent error between theoretical and experimental results

Chapter 1. Introduction

1.1 Introduction

Walking Assist Exoskeletons (WAEs) are devices that directly interact with the human body to assist with locomotion, typically when the individual has limited strength. As the demographic of elderly individuals is expected to grow in the coming years, the need for assistance is anticipated to increase accordingly. Due to muscle weakness associated with ageing, the elderly typically need assistance at the knee joint. As a complex joint, the knee of the WAE must be equipped to handle intricate movements. Unfortunately, there are high user rejection rates due to oversimplification in joint design and the resulting discomfort experienced while wearing WAEs. Thus, it is essential to dedicate research efforts to improving the ergonomics of these devices and thereby improve user retention. A promising solution is to ensure that the kinematics and kinetics of the WAE knee joint are congruent with those of the biological knee. The following thesis details the development and testing of a novel polycentric knee joint compatible with powered WAEs.

1.2 Rationale

Among several considerations, the ageing population is a motivating factor for improvements in WAE knee ergonomics. Often used to support the elderly with daily activities, the demand for WAEs is growing. In 2020, approximately 6.8 million senior individuals (i.e. 65 years of age or older) made up 18% of the Canadian population [1]. This number is expected to increase to 24% by 2036 [2]. As life expectancy increases and the senior population grows, mobility challenges associated with ageing become a significant concern. A reduction in mobility leads to loss of independence and has been directly linked to diminished quality of life [3]. Individuals with mobility challenges must rely on others for help living their daily lives, inevitably burdening society and the healthcare system.

In comparison to younger individuals, the elderly are more prone to develop mobility problems. In the lower limb, the knee is responsible for flexion and extension of the lower leg relative to the thigh. Muscle weakness around the knee joint can render mobility difficult, making staying mobile and active challenging or even impossible. As individuals age, they often develop knee pain, instability and buckling [4] brought about by weak muscles and poor balance. Knee-buckling can lead to falls, potentially causing severe injuries and hesitance to walk independently in the future.

Mobility aids such as canes, walkers and wheelchairs have been used for centuries, but human mobility challenges require novel technological solutions. As research and technology developed, orthoses became more prominent. Recently, researchers have been developing WAEs. Exoskeletons are wearable devices found in user augmentation and rehabilitation markets with two primary focuses: augmentation or assistance. Augmentation exoskeletons aim to enhance a healthy individual's strength and endurance [5]. This is especially useful for soldiers, factory workers, and firefighters, as they may need to carry heavy loads. Assistive exoskeletons can be classified into two categories: those used to aid rehabilitation processes and those that support individuals' mobility in their daily activities. Rehabilitation exoskeletons aim to assist a patient's neuromusculoskeletal function after an injury or surgery [5]. These devices are typically stationary and are designed to operate strictly in clinical environments. Powered assistive exoskeletons are designed to be self-sufficient and to deliver substantial and beneficial force to the individual.

Traditional exoskeletons frequently encounter problems relating to their biological joint constraints and uncomfortable contact points [6], [7]. Whilst powered exoskeleton technologies have recently progressed significantly, their mechanical designs do not adequately consider the complexity of human joint articulations; most importantly, the knee, which plays a significant role in human mobility. Great ergonomic advancements have been made in orthotics and passive systems, but powered exoskeletons are delayed in this respect. The human knee joint, a three-dimensional joint, is often over-simplified during powered exoskeleton design processes. In powered devices, the knee is typically modelled as a single degree of freedom (DOF) hinge joint [8], [9], [10], resulting in kinematic and kinetic challenges at the user-device interface. The decision to use a single-axis joint such as a hinge joint can likely be attributed to the complexity of transferring force through a joint that can maintain kinematic compatibility with the biological knee. This oversimplification restricts the natural motion of the user, causes discomfort, reduces the efficiency of the device, and can lead to user rejection.

Moreover, the anatomy of the biological knee plays an essential role in delivering distinct force magnitudes via muscle contraction and controlling the moment as a function of knee flexion. These characteristics are overlooked in current powered WAE designs, yielding compatibility, comfort, and actuation deficiencies.

In order to preserve the independence of elderly individuals, exoskeletons must be well adopted and accepted into their daily lives. This will require further improvement in device ergonomics, among other factors, such as ease of use. Studies have demonstrated the harmful results of having kinematic mismatch between exoskeletons and their users [11], [12], as well as the actuation deficiencies associated with current designs [12].

One promising solution is the development of a polycentric knee joint. In mechanics, the term "polycentric" refers to having more than one center of rotation. A polycentric joint can have multiple static centers or a single instantaneous center of rotation. These joints reduce the inherent kinematic mismatch between exoskeletons and their users, creating a more comfortable interaction between the two. Researchers have begun to implement polycentric exoskeleton knee joint designs as they consider the complexity of the biological joint and provide the opportunity for force delivery optimization on a kinematic level.

1.3 Objectives and Thesis Contributions

This thesis intends to design a knee joint suitable for powered WAEs that improves ergonomics by optimizing kinematic compatibility between the user and the device. A second objective is to improve performance by optimizing the actuation system force and moment delivery to the knee joint.

Among others, the following three contributions were achieved through this research:

1. A quantitative analysis of existing knee joint kinematic compatibility was conducted.
2. A novel and adaptable knee joint design was developed and tested for kinematic compatibility with the biological knee.
3. A joint was created to be used in line with the leg or at an offset and maintain kinematic compatibility in both cases.

1.4 Thesis Outline

This thesis is coordinated into seven chapters. Chapter 1 introduces the thesis topic, explains the motivation behind the research, and summarizes the thesis objectives and contributions. Chapter 2 provides a comprehensive literature review on the physiology and kinematics of the biological knee and current challenges associated with WAEs. Existing WAEs are presented, and their designs are discussed. Chapter 3 outlines design objectives and the design concept. In Chapter 4, existing designs are modelled and evaluated. This includes a simulation of the design concept and a presentation of the final SolidWorks models. Chapter 5 shows and describes the manufacturing of the prototypes and experimental setup. Chapter 6

analyzes and discusses the experimental results obtained, and Chapter 7 concludes the thesis and provides recommendations for future work.

Chapter 2. Literature Review

Chapter 2 demonstrates the outcome of a thorough literature review. The chapter is divided into five sections: the physiology of the knee, knee modelling, moment arm, current WAE challenges, existing powered WAE knee joints, and existing polycentric orthosis knee joints. Section 2.1 describes the physiology of the human knee, and section 2.2 provides different models for its instantaneous center of rotation. Section 2.3 discusses the moment arm of the biological knee joint. Section 2.4 provides a high-level overview of the main drawbacks of current WAE designs and explains the significance of offsets between biological and exoskeleton joints. Section 2.5 presents a review of current WAEs that incorporate powered polycentric knee joints. Subsequently, a theoretical comparison is provided between conventional single-axis joints, polycentric joints that follow pre-defined rotation paths, and polycentric joints that allow passive translation. Finally, Section 2.6 brings to light three existing knee joints designed for orthoses that have the potential of being integrated into a powered WAE.

2.1 Physiology of the Knee

The knee joint is one of the most complex, robust, and crucial joints in the human body. It transfers significant loads delicately in three-dimensional space. Responsible for allowing relative movement between the shank and the thigh, the knee joint is vital to several daily activities such as walking, running, climbing stairs and sitting.

The biological knee is a spatial joint with six DOFs: three rotational and three translational motions [13], [14]. It experiences flexion/extension in the sagittal plane, varus/valgus rotation in the frontal plane and axial rotation in the transverse plane. Axial rotation is also often referred to as internal/external rotation. The knee undergoes three types of translations throughout movement: anterior/posterior, superior/inferior, and medial/lateral translation. These motions are depicted in Figure 2.1.

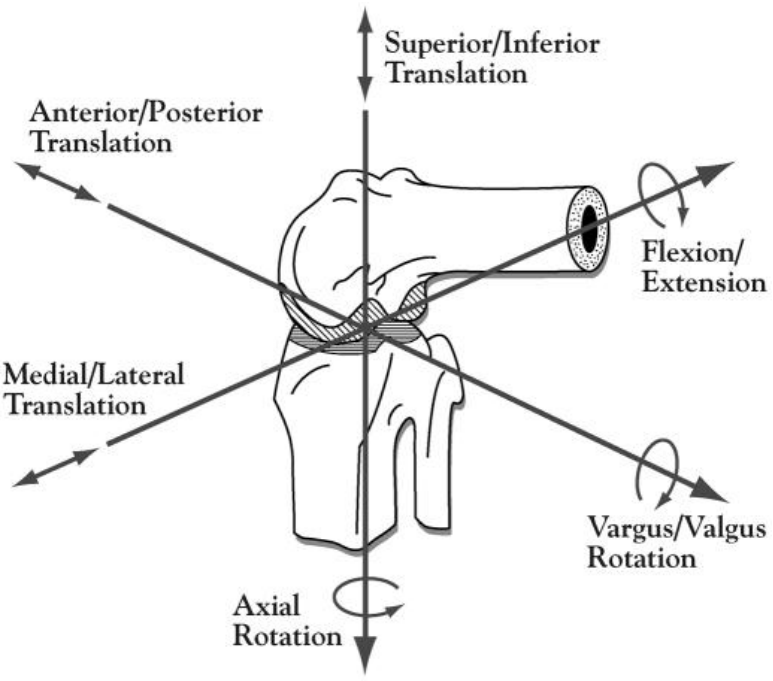

Figure 2.1. Six degrees of freedom of the knee joint. Three rotational motions (flexion/extension, axial rotation, varus/valgus rotation) and three translational motions (superior/inferior translation, anterior/posterior translation, medial/lateral translation) are identified [14]. © 2002, Baylor University Medical Center.

Since most of the DOFs of the knee joint are constrained by bony and ligamentous structures, translations of the joint in the frontal and transverse planes are often neglected [15]. On the other hand, there are significant anterior-posterior translations in the sagittal plane since the human knee experiences a rolling-sliding motion.

Due to this translation in the sagittal plane, the knee joint has an instantaneous center of rotation (ICR) and undergoes polycentric motion [12]. During flexion, the location of the ICR varies up to 20 mm [16]. The anterior-posterior translations are directly influenced by the physical structure of the femur and tibia and the shape of the articulating surfaces. For this reason, the trajectory of the ICR is unique for each individual [17]. Researchers have therefore developed models to represent the average knee's ICR translation [13], [18], [19], [20]. These will be further discussed in section 2.2.

The knee joint has a range of 140° in flexion/extension during active movement, whereas, during passive movement, the knee can reach approximately 160° flexion [5]. Elderly individuals typically require up to 120° flexion to perform daily activities such as walking, stair climbing, and sitting in a chair [21]. During walking, elderly test subjects were found to have a knee extension torque of 1.0 ± 0.4 Nm/kg body mass [22]. Assuming a range of body

mass from 50 to 100kg, the peak knee extension for this range of users is approximately 30 to 140 Nm.

In order to assist an individual's knee motion without any constraints, the assistive device must be capable of accommodating the kinematic and kinetic characteristics of the biological knee joint. Presently, the development of WAEs has insufficiently considered the mechanical characteristics of the biological joint, which can disturb and even damage human joints [13], [23]. For this reason, the mechanical characteristics of the human knee joint must be well identified, analyzed, and subsequently accounted for during the design process.

2.2 Instantaneous Center of Rotation Models

To effectively design a compatible polycentric knee joint, one must first characterize the movement of the biological knee. There exist several methods to model the ICR of the knee throughout flexion. Three methods will be discussed: Surface Contact, Cruciate Ligaments, and Tracking Center of Femoral Condyles.

2.2.1 Surface Contact

Some researchers choose to model the ICR of the biological knee as the point of contact between the two surfaces that articulate during flexion and extension: the femur and tibia. In these cases, it is assumed that any cartilage or lubricating joint fluid is negligible, and simulations are created based on bone structure. The shapes of the resulting ICR curves are dependent on which component is held stationary. In a study conducted by Wang et al., the femur was fixed, and the tibia was allowed to rotate [13]. In Figure 2.2, the ICR of the knee model is indicated by small black circles at three instances of flexion (0°, 60°, and 120°). The ICR travels along the edge of the femoral component following the red arrow.

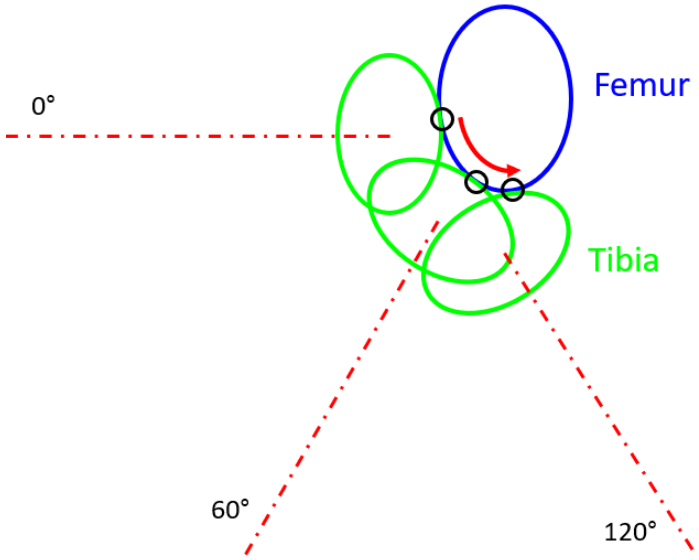

Figure 2.2. Surface contact ICR model developed by Wang et al. with fixed femur. A red arrow identifies the direction of ICR motion from 0° to 120° flexion, and points of contact are identified with black circles. Figure adapted from [13]. © 2011 IEEE.

Using the same approach, Lee and Guo developed a similar model [18]. The tibia in this model is fixed, and the femur is free to rotate. In Figure 2.3, the ICR is represented with small red circles, and the red arrow indicates the direction of its motion.

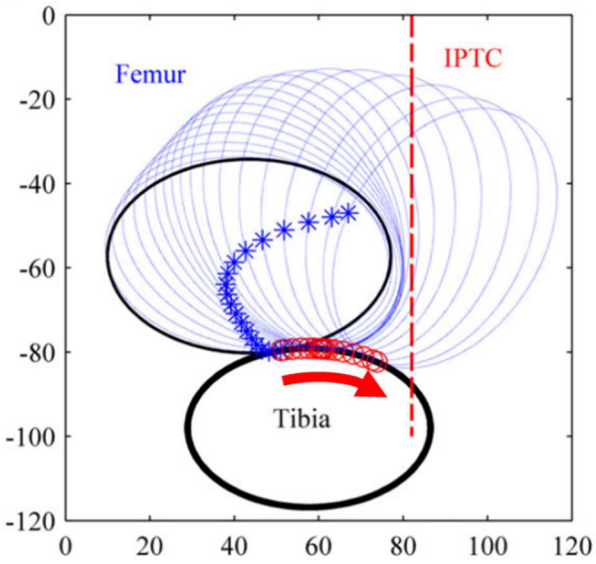

Figure 2.3. Surface contact ICR model developed by Lee and Guo with fixed tibia from -5° to 120° flexion. IPTC (ipsilateral posterior tibial cortices) is used as a point of reference. Blue stars represent the initial contact point between the femur and tibia. Direction of the ICR is identified with a red arrow, and points of contact are identified with red circles [18]. © 2010 Elsevier Ltd.

Though these models both have a similar approach, the definition of a fixed reference frame heavily influences the resulting shape of the ICR curve. It is also important to note that both studies represented the tibia as a convex bearing surface. In the biological knee, only the lateral tibial condyle is convex. The medial tibial condyle is concave, and if one considers the meniscus, the lateral tibial condyle is also concave.

The assumption that the tibia can be represented by a convex shape greatly influences the shape of the curve, and the lack of consideration of any cartilage or lubricating joint fluid adds a degree of error.

2.2.2 Cruciate Ligaments

A second modelling approach involves the physical structure of the cruciate ligaments that connect the femur to the tibia. The knee joint is sometimes considered a four-bar joint since the anterior cruciate ligament (ACL) and posterior cruciate ligament (PCL) cross in the sagittal plane. Figure 2.4 superimposes a four-bar link ABCD on an image of a cadaveric knee to illustrate this fact.

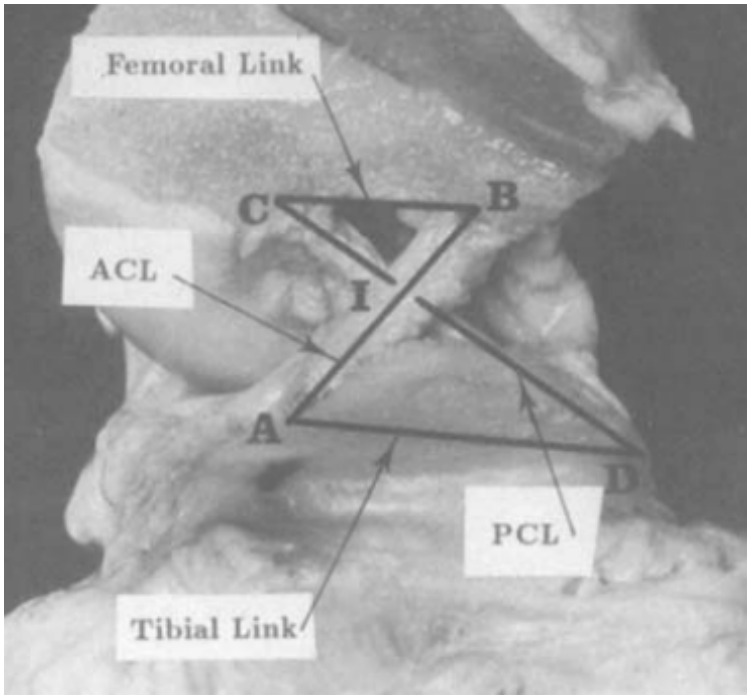

Figure 2.4. A human knee with the lateral femoral condyle removed, exposing the cruciate ligaments. A four-bar linkage ABCD is superimposed [19]. © 1989 SAGE Publications.

Since the biological knee behaves as a four-bar joint, the ICR is often modelled as the intersection of the ACL and PCL. Both Kim et al. and Russell et al. used this method and got

varying results, obtaining a relatively parabolic shape for their ICR curves. Figure 2.5 provides the results obtained by Russell et al.

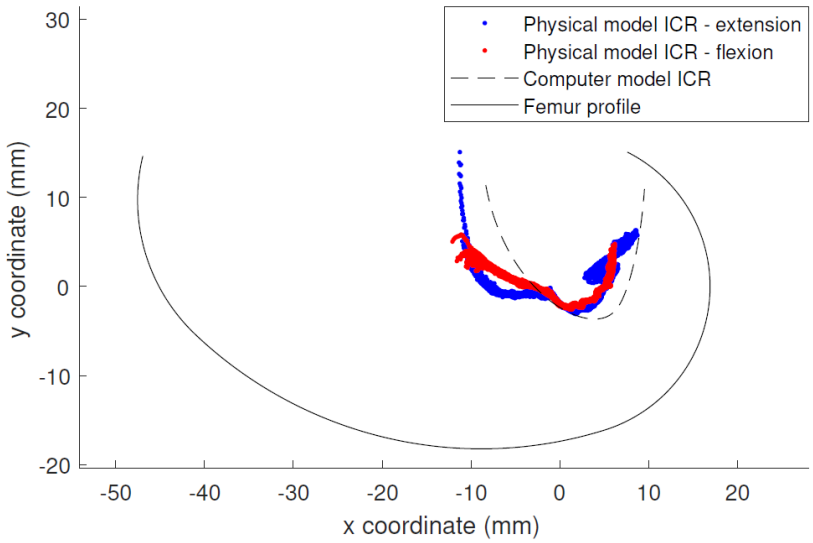

Figure 2.5. ICR measured by Russell et al. [20]. The computer model (dashed line) is based on a four-bar linkage. ICRs from physical models are shown in blue and red for extension and flexion, respectively. © 2018 IEEE.

It is typically assumed that the ACL and PCL behave as rigid links throughout flexion for this type of model, but Heller et al. showed that ligaments lengthen and have strains that vary as a function of flexion/extension angle [24]. As shown in Figure 2.5, the ICR curves obtained using the physical models both vary from the computer model. The shape of the curve also varies depending on whether the knee was being flexed or extended.

2.2.3 Tracking Center of Femoral Condyles

The third method to be discussed involves tracking the center of the femoral condyles throughout flexion. To describe the motion of the knee, a transverse axis intersecting the center of each femoral condyle is tracked throughout flexion from 0° to 120° [25]. In a study by Walker et al., it was assumed that the posterior portion of the femoral condyles could be represented as spherical surfaces, which was later validated. Flexion was measured from the long axis of the femur using video radiography, and 0° of flexion was defined by the long axes of the tibia and femur being collinear. This definition will hold for this thesis as well. The axis system used by Walker et al. can be seen in Figure 2.6.

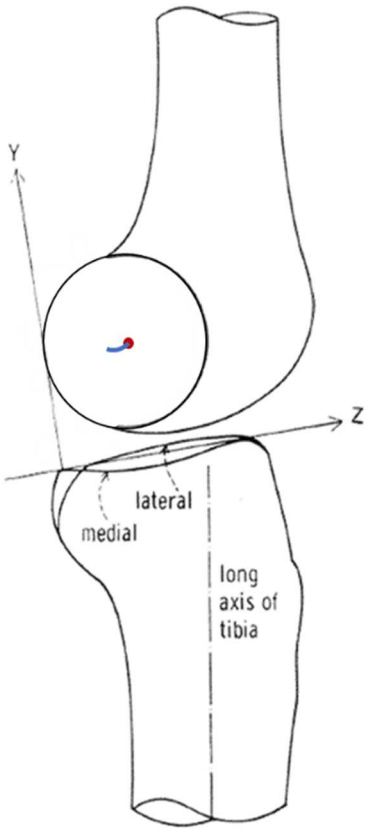

Figure 2.6. ICR model developed by Walker et al. The ICR at 0° flexion is indicated by a red point, and a blue curve depicts the ICR translation from 0° to 120°. Figure adapted from [25]. Public domain.

Based on their collected experimental radiography data, Walker et al. derived best-fit quadratic equations for the anterior-posterior translation Z_{DIS} and distal-proximal translation Y_{DIS} of the transverse axis as a function of flexion angle F, where the translation is measured in mm and flexion in degrees.

$$Z_{DIS} = -0.0602\,F + 0.0000178\,F^2 \tag{2.1}$$

$$Y_{DIS} = -0.05125\,F + 0.000308\,F^2 \tag{2.2}$$

Equations (2.1) and (2.2) describe the motion of the average center of the femoral condyles relative to the tibial axis in the sagittal (Y-Z) plane and are plotted from 0° to 120° flexion in Figure 2.7. The origin (0,0) is defined at the center between both femoral condyles at 0° flexion.

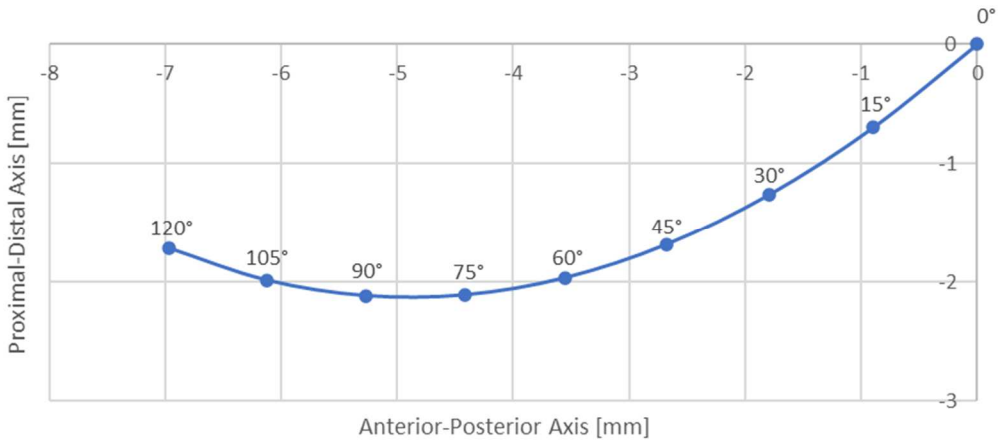

Figure 2.7. Translation of the instantaneous center of rotation from 0° to 120° according to the model developed by Walker et al.

This modelling method has been used in several studies as a dependable basis for tracking the ICR of the knee [26], [27].

2.3 Moment Arm

Due to the complex physical structure of the biological knee joint, its force delivery is not constant throughout flexion. From a sagittal perspective, the muscles primarily responsible for knee extension are the quadriceps: the vastus intermedius, vastus lateralis, vastus medialis and rectus femoris [28]. In order to extend the knee, the quadriceps contract and a tensile force is applied across the patella and patellar ligament through to the tibia. This structure can be seen in Figure 2.8.

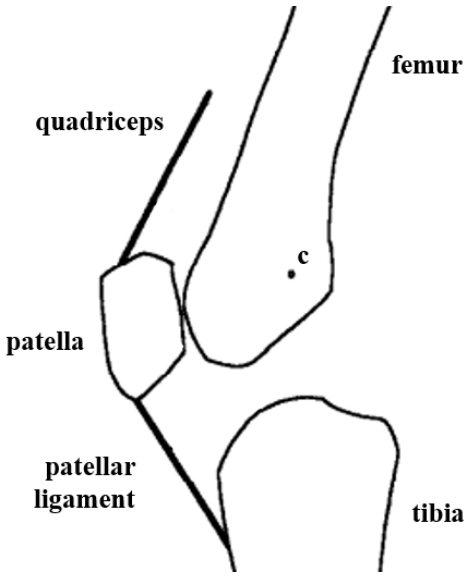

Figure 2.8. Sagittal section through a sketch of the knee where c is the ICR relative to the femur. Adapted from [29]. © 1991 Elsevier Ltd.

Due to the physical structure of the biological knee, the moment arms of the knee change throughout flexion. Through various studies, its variation has been documented [29], [30]. Figure 2.9 provides biological knee moment arm data from a collection of studies on the rectus femoris, one of the quadriceps muscles responsible for knee joint extension.

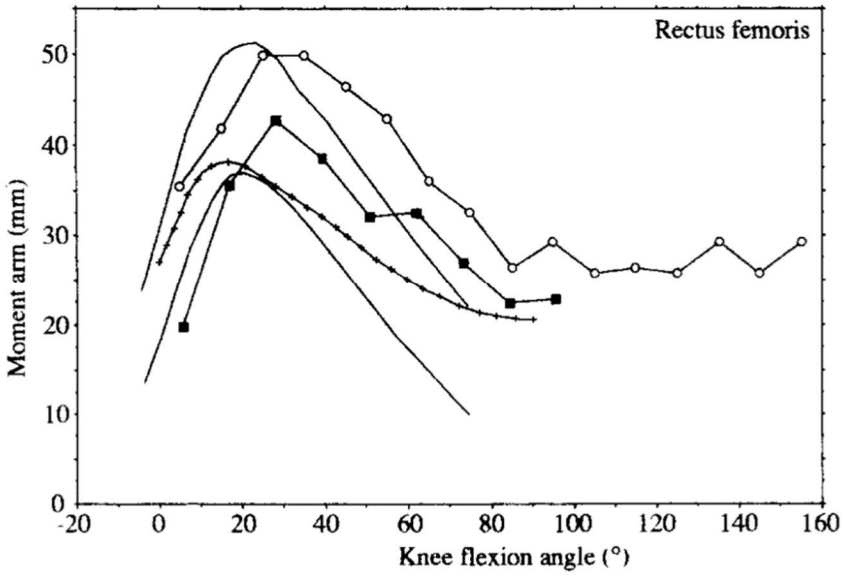

Figure 2.9. Rectus femoris moment arms at the knee joint [29]. (■) from 10 tendon positions, [29]; (○) from 17 tendon positions [30]; (+) quadriceps, averaged over 6 specimens, from moment and force [31]; unmarked lines: quadriceps, upper and lower bounds for 5 specimens, from moment and force [32]. © 1991 Elsevier Ltd.

Though most of the studies demonstrated in Figure 2.9 do not measure the moment arm past 100° flexion, the moment arm plateaus past 90° and becomes relatively constant [30]. When modelling the knee in this research, it will be assumed that the moment arms of the biological knee are constant between 90° and 120° flexion.

Figure 2.10 provides quantitative data for the magnitude of the patellar tendon moment arm from 0° to 90° flexion in mm.

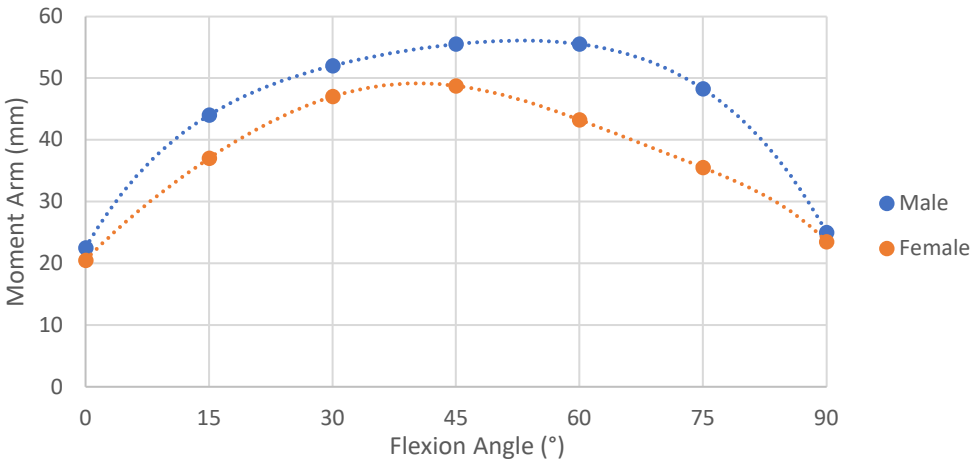

Figure 2.10. Patellar tendon moment arm vs. knee flexion angle from male and female cadavers from 0° to 90°. Data retrieved from [33].

As previously discussed, it can be assumed that the biological knee's moment arm is constant between 90° and 120° flexion [30]. Figure 2.11 was generated based on this assumption, allowing for knee modelling from 0° to 120° flexion.

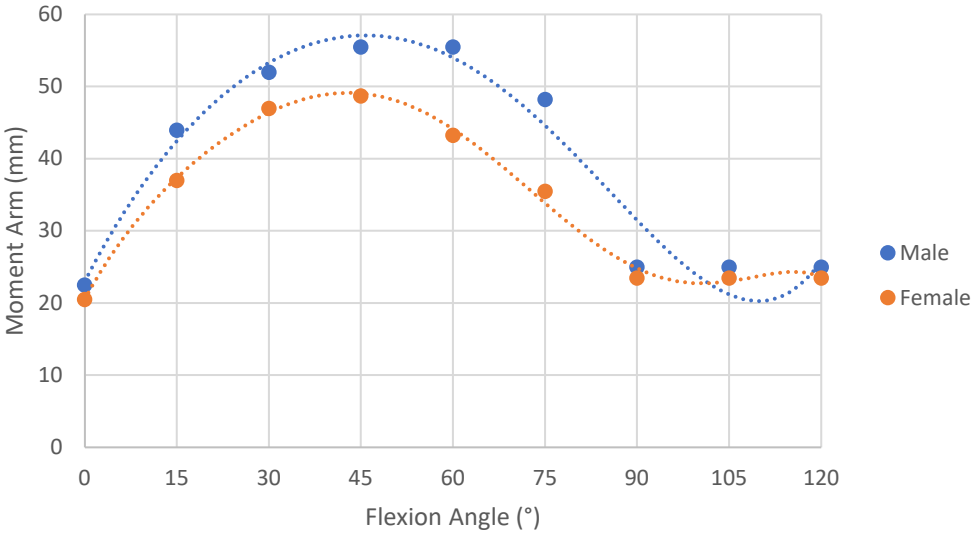

Figure 2.11. Knee moment arm (from patellar tendon) vs. knee flexion angle from male and female cadavers from 0° to 120°. Data for 0° to 90° was retrieved from [33], and constant values from 90° to 120° are based on the assumption from [29], [30].

This moment arm model will be further discussed in sections 4.1.1.2 and 4.1.2.3.

2.4 Current Challenges

Though extensive research has been conducted on the mechanics and robotics of exoskeletons and the human body separately, an area that requires more attention is the interface between the two. Kinematic compatibility is crucial in designing a mobility assistance device, especially if worn for long periods of operation. Forces that cause discomfort are generated when the kinematic compatibility between the exoskeleton and the wearer is insufficient. Kinematic incompatibilities arise from misalignment between the center of rotation of the biological knee and the exoskeleton joint, altered range of motion (ROM), DOF limitations, mechanical restrictions due to the size of the device, initial offsets during donning of the device, interface migration (slip) throughout movement, and the oversimplification of human knee joint kinematics.

Theoretically, if the connection between an exoskeleton and its wearer were perfectly rigid, no motion would be permitted given kinematic incompatibilities. If the rotational axes of the external and biological joints are not perfectly aligned, any movement is strictly possible due to the deformation of soft tissues [34]. Figure 2.12 provides a graphical demonstration of an offset between an exoskeleton joint and a human joint.

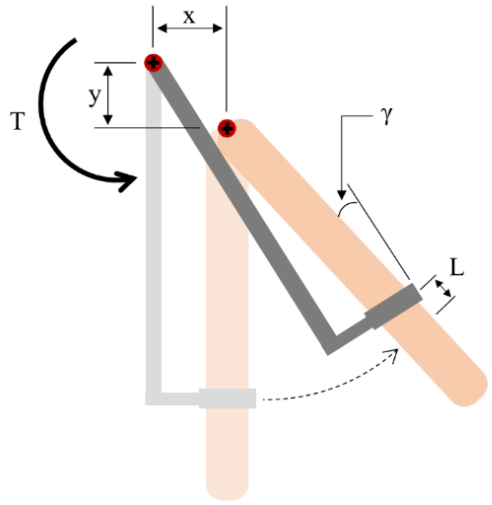

Figure 2.12. Offset between an exoskeleton joint and a human joint. Offset x, y, applied torque T, brace displacement L, brace rotation γ. Recreated from Näf et al. [12].

With reference to Figure 2.12, the exoskeleton joint is horizontally offset by a distance x and vertically offset by a distance y. With an applied torque T, the brace is displaced by a

distance L up the limb and is rotated by γ. Since this movement is typically not permitted or desired with exoskeleton use, misalignment can cause several adverse effects.

As previously discussed, the motion of the knee joint is three-dimensional. Many current knee joints follow kinematic pathways substantially simpler than those of the anatomical knee [23], [35]. Typically, the human knee is simplified as a one DOF hinge joint. However, its ICR migrates during movement due to a rolling motion between the femur and the tibia. Since these small translations are neglected during the simplification of the joint, the exoskeleton cannot account for this migration. Though this simplification is acceptable for small angles, there is a significant discrepancy during larger movements [36]. The mismatch between the DOFs of the two joints causes offsets between the rotation axes, which in turn creates undesirable residual forces [23], [35].

Offsets and misalignments can influence the voluntary ROM, natural patterns of movement, and muscle activation patterns of the user and increase metabolic cost [12], [37]. It also tends to interfere with the transfer of assistive torques onto the body and can cause discomfort or pain and may even lead to long-term injury. Hence, offset is undesirable and must be avoided.

In order to avoid problems associated with kinematic mismatch, polycentric knee joints can be integrated into lower-limb exoskeletons. These joints can minimize the interference between the device and the body by achieving adequate axis alignment [38]. Not only do they more closely follow the natural motion of the knee, but they are known to promote a more natural gait during the stance phase due to their ability to expand the region of knee stability [34].

2.5 Existing Powered Polycentric Knee Joints

To address the current challenges of WAEs, further work must be carried out. Reviewing existing devices and the steps researchers have made to improve upon other works can give insight into the possible future direction of ergonomics concerning WAEs.

Several commercially available WAEs use single-axis joints that are ergonomically insufficient for daily wear and are susceptible to user rejection. The Keeogo+, HAL for Well-Being Lower Limb Type Pro, and Indego Personal are all examples of devices with single-axis joints [8], [10], [9]. As discussed in section 2.4, the use of a single-axis joint in a WAE is not ideal.

As the knee is a 3-dimensional joint, it naturally moves in all three planes: sagittal, frontal and transverse. From an ergonomic point of view, passively allowing motion in the frontal and transverse planes meanwhile actuating in the sagittal plane is ideal. Unfortunately, allowing these motions requires a more complex design, thereby increasing the bulk and cost of the device.

Polycentric devices that restrict knee motion to the sagittal plane tend to be considerably less complex than those that allow other rotations. These devices can be further divided into two sections according to the method by which they allow polycentric motion: using a pre-defined path of ICR or allowing passive translation. Devices that follow a pre-defined path of rotation are typically designed based on average biological joint geometries, whereas those that allow for passive adjustment to the user rely on the decoupling of translations and rotations [11].

Since the natural knee has its most significant translations and rotations in the sagittal plane, devices that restrict motion to this plane can still be relatively ergonomic if designed correctly. In this case, it is up to the designers to determine whether the benefits of having a simpler joint will outweigh any restrictions on the knee. The following section will present several existing knee joints with a pre-defined ICR path and a few that undergo passive ICR translation.

This review was limited to powered knees primarily due to two factors, the first of which is their high level of efficiency in mobility assistance. Secondly, powered knee joints can produce and transfer large torque magnitudes to the body, making them more likely to cause injury.

2.5.1 iT-Knee

The iT-Knee is a powered knee exoskeleton that provides assistive torques up to 140 Nm in the sagittal plane, meanwhile allowing passive varus/valgus and internal/external rotational DOFs. The under-actuated device has 6 DOFs, where the one active DOF (flexion/extension) is powered by an electrical rotary series elastic actuator [5]. The maximum ROM of the device is not specified, but tests were carried out from 0° to 120° flexion, which is less than the natural ROM of the knee, though it is sufficient for daily activities.

In order to compensate for the translation of the knee joint, the iT-Knee incorporates a mechanism that allows passive self-alignment with the ICR of the natural knee. The

mechanism involves two parallelogram structures in series that transmit pure torque generated by the actuator through a universal joint [5]. This is referred to as an S2AP mechanism.

A feature that sets this knee exoskeleton apart from the others is the placement of the actuation and transmission mechanisms on the upper thigh. To allow wheelchair users access to the exoskeleton, the designers have favoured a frontal implementation instead of the classic lateral one [5]. Saccares et al. claim that this device has a low mass, a small form factor and low inertia effects, though Ranaweera et al. have called it "complex and heavy for everyday use" compared to their device, Anthro-X. The iT-Knee can be seen in Figure 2.13.

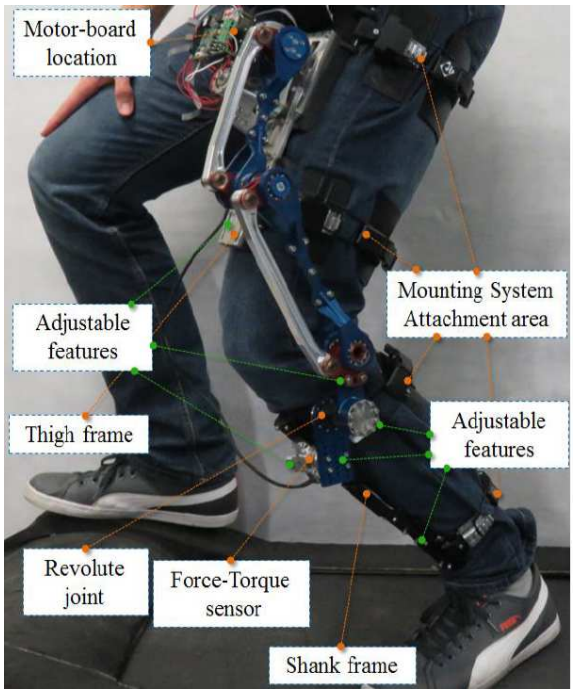

Figure 2.13. iT-Knee with identified components [5]. © 2016 IEEE.

2.5.2 Self-adjusting, Isostatic Exoskeleton

The Self-adjusting, Isostatic Exoskeleton created by Cai et al. is designed to achieve pure torque transmission to the knee joint ergonomically [16]. This mechanism is made up of a seven-link chain with six DOFs. These include one active rotational DOF to provide up to 40 Nm of torque to promote flexion/extension and five passive DOFs (four of which are rotational) to ensure comfort for the user [16]. This magnitude of torque is appropriate for WAE designs, assuming that the ideal assistance level for the user is 40% of the natural torque required for walking [39].

This device actuates flexion and extension, allowing passive motion in frontal and transverse planes and passive ICR translation. Though the ROM of the device is unspecified,

by examining provided test results, it appears that flexion never exceeds 100°, which is sufficient for walking but not for stair climbing or sitting in a chair [21].

Celebi et al. believe that though this design is ideal from an ergonomics perspective, it is unnecessarily complex and heavy [17]. Saccares et al. have also agreed that it is too "complex, bulky and heavy" [5]. The position of the joint with respect to the human knee can be changed by using a vertical slider. Näf et al. have interpreted this to mean that the device would still rely on manual alignment [12].

The Self-adjusting, Isostatic Exoskeleton, as seen in Figure 2.14, was designed as a prototype for both rehabilitative and assistive purposes but was only found to be successful in a rehabilitation scenario. Throughout testing, it was discovered that the device does not provide sufficient assistance to the user during walking [16]. Cai et al. explain that since the rotational velocity is saturated and plateaus, the resulting rotation angles are unnatural, and the support is inadequate. This has been deemed a problem to address in the future.

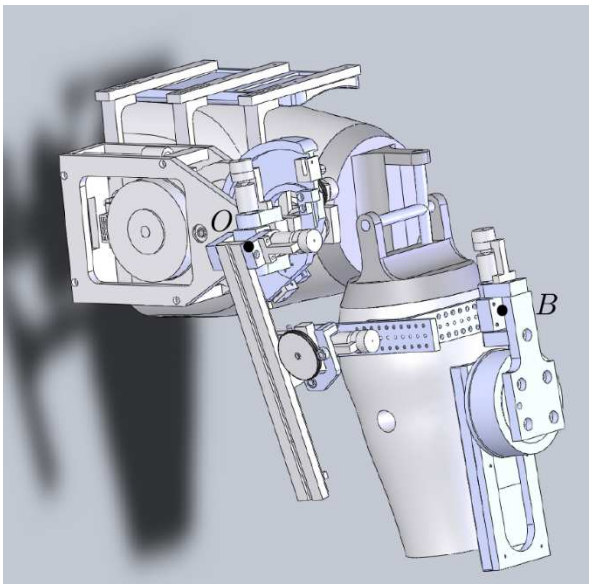

Figure 2.14. Computer-Aided Design model of the Self-adjusting, Isostatic Exoskeleton [16]. ©2011 IEEE.

2.5.3 Human Universal Mobility Assistance Device

The Human Universal Mobility Assistance (HUMA) device employs a polycentric knee joint to allow motion in the sagittal plane, including anterior/posterior translation and flexion/extension. A double four-bar linkage transfers actuating torque from the thigh to the shank segment [34]. One four-bar is used as a powertrain between the actuator and the second four-bar, allowing for the joint's polycentric motion [34]. The knee joint implemented in the HUMA device is displayed in Figure 2.15.

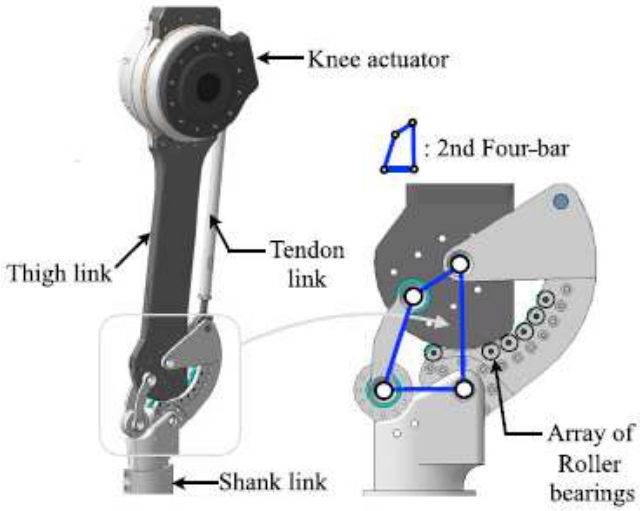

Figure 2.15. Knee joint of the HUMA device [34]. © 2017 Elsevier B.V.

The design of the four-bar mechanism is based on the average ICR of the biological knee, and the lengths of the four-bar links were selected to broaden the range of angles where the user experiences voluntary knee stability. When the knee flexion angle is below 15°, the ICR of the device is above the ICR of the anatomical knee, providing stability [34]. The complete ROM of the device ranges between -2° and 110° flexion [34]. This allows for a natural amount of hyperextension of the joint but limits natural flexion, which can reach 140°.

Since polycentric mechanisms have weaker mechanical durability for weight-bearing than single-axis mechanisms, roller bearings are implemented between the thigh and shank segments to provide support and improve durability. The second four-bar is rendered unnecessary by supporting the trajectory of the pre-defined ICR with a solid curve lined with roller bearings. The track of roller bearings creates a cam-like surface, meaning that the device no longer needs to rely on the four-bar mechanism to create the desired ICR path.

2.5.4 Anthro-X

The Anthro-X is a powered mobility assistance exoskeleton with a polycentric knee joint to enhance kinematic compatibility. The joint only allows for movement in the sagittal plane with powered rotation. The polycentric motion of the knee joint is facilitated by a four-bar mechanism connected to an electrically actuated planetary gear motor that provides torques up to 13.5 Nm. This four-bar mechanism provides a pre-defined path designed to follow the predicted ICR of the biological knee. The knee joint of the Anthro-X has a ROM of -5° to 90° of flexion [38], which is adequate for normal walking but is otherwise quite limiting. In order to minimize inertia and maximize comfort and maneuverability, the structure surrounding the

knee joint was designed to follow body contours closely [38]. Both overground and treadmill walking tests were carried out at 1.3 m/s, and no undue restrictions or abnormal movements were reported. This walking speed is more than sufficient for testing, considering the average walking speed of elderly individuals ranges between 0.78 and 0.86 m/s [40]. The Anthro-X is shown in Figure 2.16.

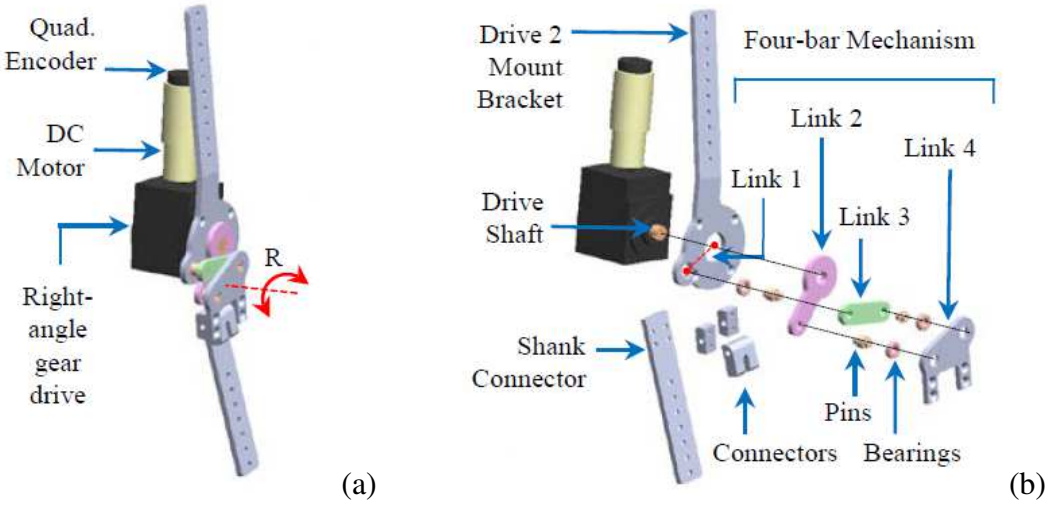

Figure 2.16. (a) Anthro-X assembly, (b) exploded view with identified components [38]. © 2018 IEEE.

2.5.5 AssistOn-Knee

The AssistOn-Knee, as seen in Figure 2.17, is an exoskeleton designed for robot-assisted rehabilitation. It actively assists with flexion/extension of the knee and passively allows for translational movements of the ICR. The decision to restrict motion to the sagittal plane was motivated by a design criterion to keep the weight and the complexity of the mechanism low [17].

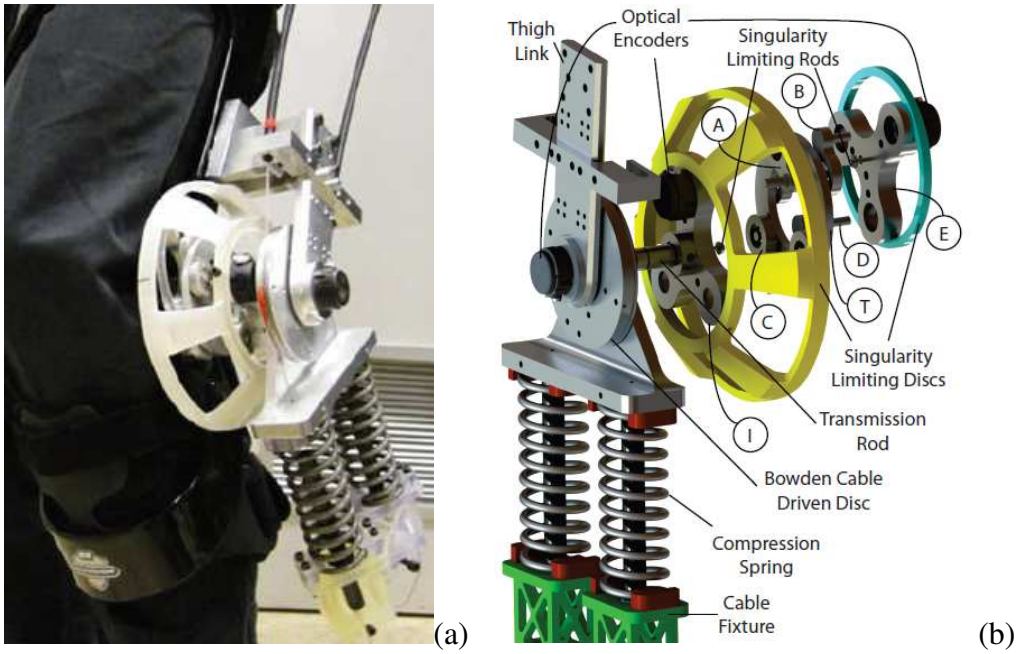

Figure 2.17. (a) AssistOn-Knee joint, (b) exploded view with identified components [17]. © 2013 IEEE.

The exoskeleton uses a Schmidt coupling, a planar parallel kinematic chain with two DOF of in-plane translations and one DOF of rotation about the axis perpendicular to the plane [17]. The Schmidt coupling comprises seven rigid bodies: the input ring I, intermediate ring T and output ring E, two links A and B that connect I to T, and two links C and D that connect T to E [17]. The active rotational DOF is controlled by a Bowden cable-driven series elastic actuator [17]. A Bowden cable was selected to enable the motor and gear reduction unit to be placed away from the knee, reducing the weight of the knee exoskeleton [17].

Since the actuation unit is not placed directly on the body, this device is unsuitable for mobility assistance in day-to-day life. Ranaweera et al. have deemed this device "complex and heavy for everyday use" [38]. Kuan et al. have also discussed that the system is overly heavy and bulky due to the relatively sophisticated coupling structures in AssistOn-Knee [41].

AssistOn-Knee has a greater ROM than typically achievable (-10° to 170°) and can provide torques up to 35.5 Nm [17]. Tests have not yet been carried out to verify that the device does not interfere with the natural walking gait of its users.

2.5.6 Samsung-Assist Device Lower-Limb Type

Choi et al. have developed the "Samsung-Assist device Lower-Limb type" or "S-Assist" [6]. It is a lower-limb assistive exoskeleton with a self-aligning knee joint, meaning that the ICR undergoes passive translation. The actuator is placed in a backpack and actuates the knee

joint remotely by steel cables [42]. A cable tension of 735.5 N is applied to achieve a maximum joint torque of 20 Nm during operation [6]. The self-aligning mechanism has two passive DOFs and one active, rotational DOF. It comprises two links and four pulleys (two of which are fixed together) [6]. Only one pulley is connected to the actuator; the others align themselves passively [6]. The S-Assist can be seen in Figure 2.18.

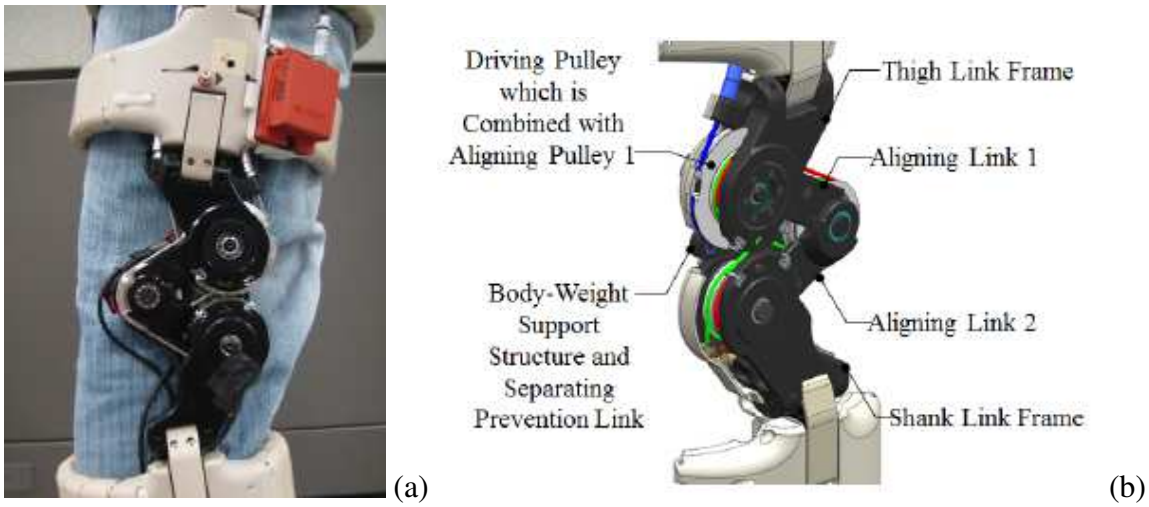

Figure 2.18. (a) S-Assist device on human leg. (b) Isometric view of knee joint with labelled components [6]. © 2016 IEEE.

The device relies on angle sensors attached to the pulleys to ensure appropriate knee motion [6]. This may be more complex than necessary, as a mechanical component (such as a timing belt, cam mechanism, or other) could ensure the correct angles. Sensors may be a source of error, tend to be more challenging to maintain and increase the overall cost of the device.

The S-Assist's knee joint restricts motion to the sagittal plane. It has a ROM of 0° to 160° flexion and allows maximum translations of 30 mm in the anterior-posterior direction and 35 mm in the inferior-superior direction. During testing, it was found that the user is free to perform several movements in different postures without resistance [6]. The strength in the design of this device lies in its size. With a maximum thickness of 34.5 mm, it can be discreetly worn underneath clothing [6]. According to Choi et al., the lack of an actuator on the side of the leg makes it possible to create an exoskeleton that is approximately two times thinner than conventional exoskeletons [6].

2.5.7 Adaptive Coupling Joint

The Adaptive Coupling Joint (ACJ), developed by Kuan et al., is a cable-driven joint mechanism designed to passively match the ICR of the biological knee [41]. The ACJ allows

alignment with the natural rotation axis using a two DOF five-bar linkage system, where the input and output links form a double-rocker mechanism [41]. These components are identified in Figure 2.19.

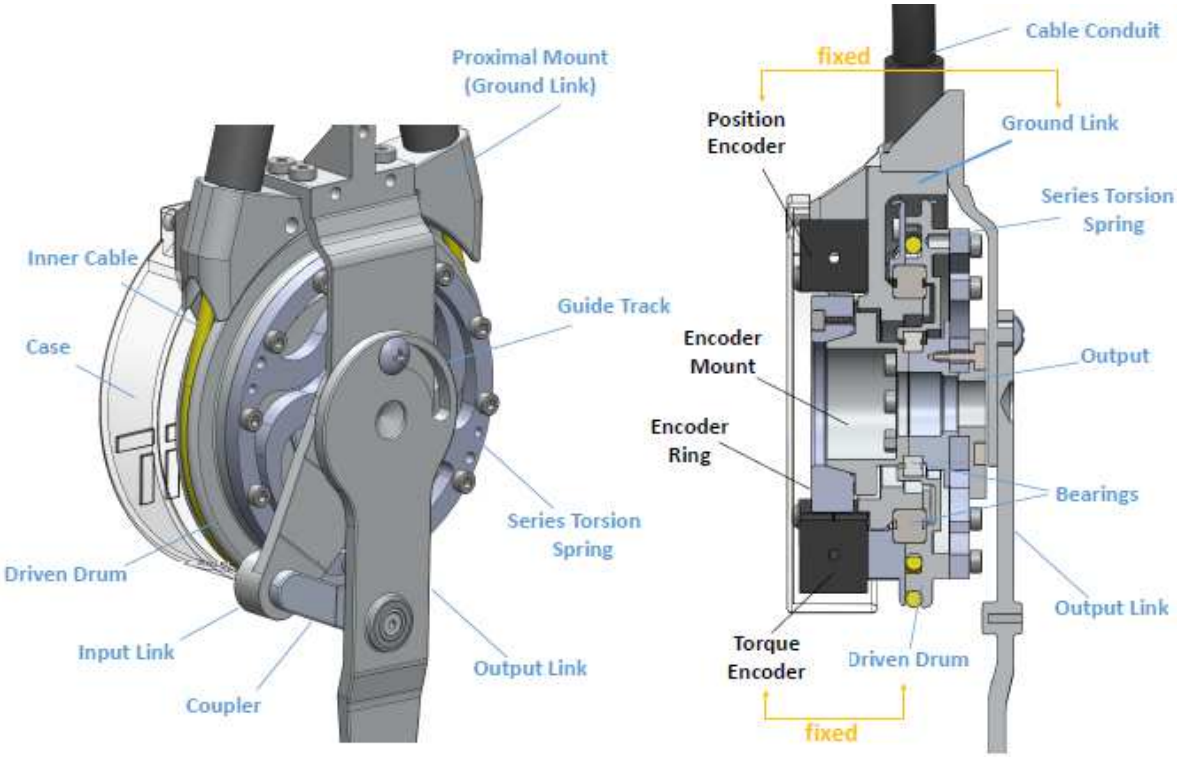

Figure 2.19. Adaptive Coupling Joint with identified components [41]. © 2014 IEEE.

The ACJ is powered by a remotely located actuator connected to the joint by cables that function in a "pull-pull" configuration [41]. It provides a maximum torque of 110 Nm [41], which provides significantly more assistance than typically required in a WAE for elderly patients. At 53 mm thick and with a ROM of 0° to 120° [41], the ACJ is bulkier and more restrictive than the S-Assist but still allows for sufficient freedom to walk normally. Like the S-Assist, the ACJ also restricts motion to the sagittal plane.

To promote safety, the ACJ was designed with limits on the ICR position of the joint. A guide track keeps both proximal-distal and anterior-posterior translations of the output link within the range of 0 - 20 mm [41]. Testing proved the ACJ to successfully transfer torques without hindering natural movement patterns [41]. No significant problems have been reported with this device. Hence, the ACJ is being readied for further bench and human testing.

2.5.8 Overview of Powered Polycentric Knee Joints

In order to evaluate a knee joint design, several factors must be taken into consideration. These include mechanical restrictions imposed on the user, the level of assistance provided, and kinematic compatibility with the body. It is also essential to consider the type of actuation that the design can accommodate the device's size, weight, and complexity. For a particular application, some designs may be more suitable than others. For this reason, the evaluation of knee joint designs must be carried out with a specific application in mind. In WAEs for the elderly population, knee joints must be lightweight since these individuals generally have less muscle strength. As the elderly are prone to injuries, the joint must be designed to remain within a natural ROM and minimize any undesirable forces associated with kinematic incompatibilities.

Table I provides an overview of all previously presented devices. The planes of motion that the devices permit are outlined, noting that all powered devices only provide active assistance in the sagittal plane.

Table I. Overview of existing powered polycentric knee joints.

Device Name	**DOFs**	**ICR**	**Sagittal ROM (°)**	**Actuation**	**Maximum Torque (Nm)**	**Significant Feature**
iT-Knee [5]	All	Passive translation	0 to 120	Electrical rotary series elastic actuator	140	Designed to accommodate wheelchair users
Self-adjusting, Isostatic Exoskeleton [16]	All	Passive translation	Unspecified	Brushless motor and a two-stage, back-drivable, 100:1 transmission	40	Proven successful for rehabilitation but insufficient for walking assistance
Human Universal Mobility Assistance Device [34]	Sagittal	Pre-defined path	-2 to 110	Brushless DC motor, a 50:1 harmonic gear, and a torque transducer	Unspecified	Double four-bar mechanism designed to maximize knee stability
Anthro-X [38]	Sagittal	Pre-defined path	-5 to 90	Electrically actuated planetary gear motor	13.5	Single four-bar mechanism following predicted ICR of the average biological knee
AssistOn-Knee [17]	Sagittal	Passive translation	-10 to 170	Bowden cable-driven series elastic actuator	35.5	Actuation unit is not placed on the body, restricting applications to rehabilitation only
Samsung-Assist Device Lower-Limb Type [6]	Sagittal	Passive translation	0 to 160	Back-drivable ball-screw linear actuator	20	Can be discreetly worn underneath clothing but the user must carry the actuator in a backpack
Adaptive Coupling Joint [41]	Sagittal	Passive translation	0 to 120	Unspecified	110	Double-rocker mechanism with a guide track to keep ICR translations within safe ranges

2.5.8.1 Actuation System

Four of the previously discussed joints have situated the actuator on the thigh: the iT-Knee, Self-adjusting Isostatic Exoskeleton, HUMA and Anthro-X. Due to inertia, the addition of mass distally on the leg increases metabolic cost and promotes unnatural gait patterns [43]. For this reason, it is more desirable to locate the actuator on the thigh than on the shank. Regarding simplicity, it often makes sense to fix the actuator to the thigh. Unfortunately, this added weight will still impact the user's gait, and ideally, the actuator should be placed even closer to the user's center of mass.

Three of the previously discussed devices are powered remotely by cables: the AssistOn-Knee, S-Assist and ACJ. By choosing to use cables, the actuator can be placed closer to the wearer's center of mass. This thereby reduces the inertia caused by the added weight, reducing negative impacts on gait. It also enables direct torque transmission by flexible and complex paths, facilitating thin designs that conform to the wearer's body [42]. A drawback of relying on cables to transfer torques is the loss associated with friction, especially with small components. As cables are bent with smaller radii, there is an increase in resulting friction. Also, cables can introduce restraints across the user's hip joints depending on the placement of the actuator.

2.5.8.2 Frame Design

Regarding respecting the natural ROM of the biological knee joint, some devices are more successful than others. The AssistOn-Knee has a ROM that exceeds the natural ROM, meaning that there is a possibility for user injury. The S-Assist device matches the passive ROM of the natural knee exactly; hence it can allow for all natural motions in the sagittal plane. The iT-Knee, ACJ and HUMA devices have ROMs that are more limited than the biological joint yet allow their users to perform most daily activities. Thus, these are sufficient without needing to over-complicate their designs. The Anthro-X, which only allows up to 90° flexion, may be too restrictive. While this is sufficient to permit normal walking, the flexion restriction may prevent more complicated motions such as sitting and crouching.

2.5.8.3 Knee Joint Mechanical Design

Overall, there are three main approaches to designing knee joints in a WAE. The first traditional method uses a joint with a single axis of rotation that restricts all motion to the sagittal plane. Though it is a simple design that allows for a more compact and lightweight device, it does not account for the complexity of the human knee and is therefore not comfortable for the user.

The second and third approaches use polycentric joints to increase the ergonomics of the human-device interface. The second method uses a pre-determined path along which the joint rotates, typically based on the average human knee ICR. Using a pre-defined path of ICR in a mechanism can be very beneficial to achieve a simple, lightweight and sleek joint. Since this method does not rely on adding joints to achieve kinematic redundancy, the mechanism can be kept uncomplicated with only one DOF. This has the added benefit of increasing the ease of fabrication and decreasing the device cost, making it more accessible to users. The main

drawback of using a pre-defined ICR path is that biological joint anatomy differs slightly between individuals, making it nearly impossible for the path to be perfect for the wearer. Unfortunately, the degree to which a joint must kinematically match the biological knee to ensure user comfort has not yet been determined. This is likely because several factors impact this, such as the structure of the strapping, padding, and shape of the user-device interface.

The third method is to use passive ICR translation. This relies on decoupling the rotation and translation of components, making it a bulkier solution. Due to this decoupling, simulations are much more challenging to achieve. For this reason, designers are unable to predict the wear or efficiency of the device easily. Implementing a mechanism that allows for the passive translation of the ICR is more complex than those that follow a pre-defined path. This method is associated with the added benefit that it will naturally adjust to fit with any individual's biological joint geometry and counteract misalignment caused by initial offset to a certain degree, thereby shortening donning times. Unfortunately, more complex joints such as these are inherently bulkier and can suffer higher user rejection rates.

Figure 2.20 displays all three design types. Due to high variability between configurations, a four-bar joint was chosen to represent the second design type, and a joint with three hinges was selected as an example of a joint with passive ICR translation.

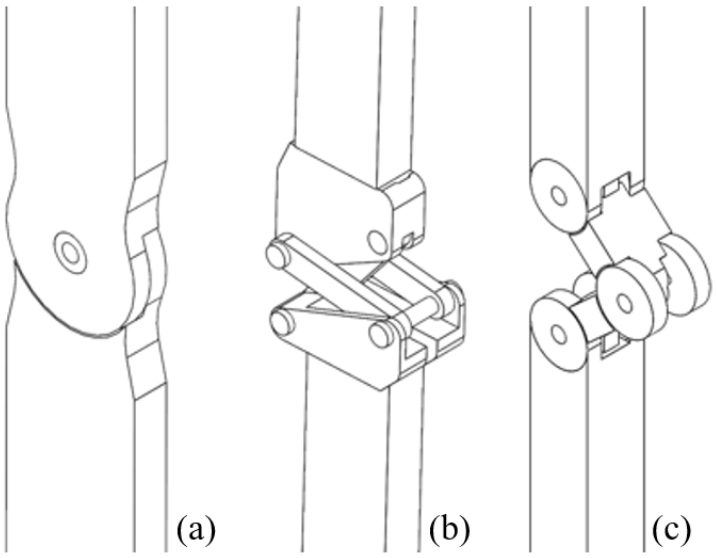

Figure 2.20. (a) Single-axis joint, (b) joint with a pre-defined path of ICR, (c) joint with passive ICR translation.

The true trajectory of the ICR depends entirely on how a joint is designed and cannot be generalized. In order to simulate the behaviour of the device, a design must first be fully conceptualized.

2.6 Existing Orthosis Knee Joints

As the field of research on orthoses is more mature than that of WAEs, there has been more success in improving the kinematic compatibility of these devices with the biological knee. As these joints are not designed to transfer power, solutions to kinematic challenges have been more accessible. In WAE design, the emphasis has primarily been placed on the powered mechanical and robotic elements instead of the ergonomics. This is the opposite in orthosis joint design. Thus, it is a worthy endeavour to examine the relevant literature. Selected orthosis knee joints will be reviewed as they have been fully optimized and could be adapted to powered applications.

2.6.1 Single-Axis Joint

Firstly, the OTC 2554 knee brace is one of many orthoses that use a single-axis joint. Figure 2.21 shows the device attached to a user's leg.

Figure 2.21. Single-axis Joint (OTC 2554 Knee Brace) [44]. © 2020 Surgical Appliance Industries, Inc. & Airway Surgical Appliances Ltd.

Several devices use this type of joint with a singular hinge to allow flexion; the OTC 2554 will be used as an example. Single-axis joints are typically constructed from two bars with a

connecting pin in the center. The bars are fixed to the thigh and shank of the user using strapping, and the connecting pin allows the bars to rotate. This permits flexion and extension of the joint. The OTC 2254 does not have any stopping mechanisms to prevent hyperextension of the biological joint, leaving the potential for injury. Since this type of joint rotates about a single point, any offset between the ICR of the device and the biological knee is compensated by compression of soft tissues or strapping slip. As the single-axis joint is not always ergonomically appropriate, polycentric knee orthoses were developed.

2.6.2 Double-Hinge Gear Joint

Figure 2.22 provides an example of a knee orthosis that has been designed to mimic the biological knee better than a single-axis joint [45].

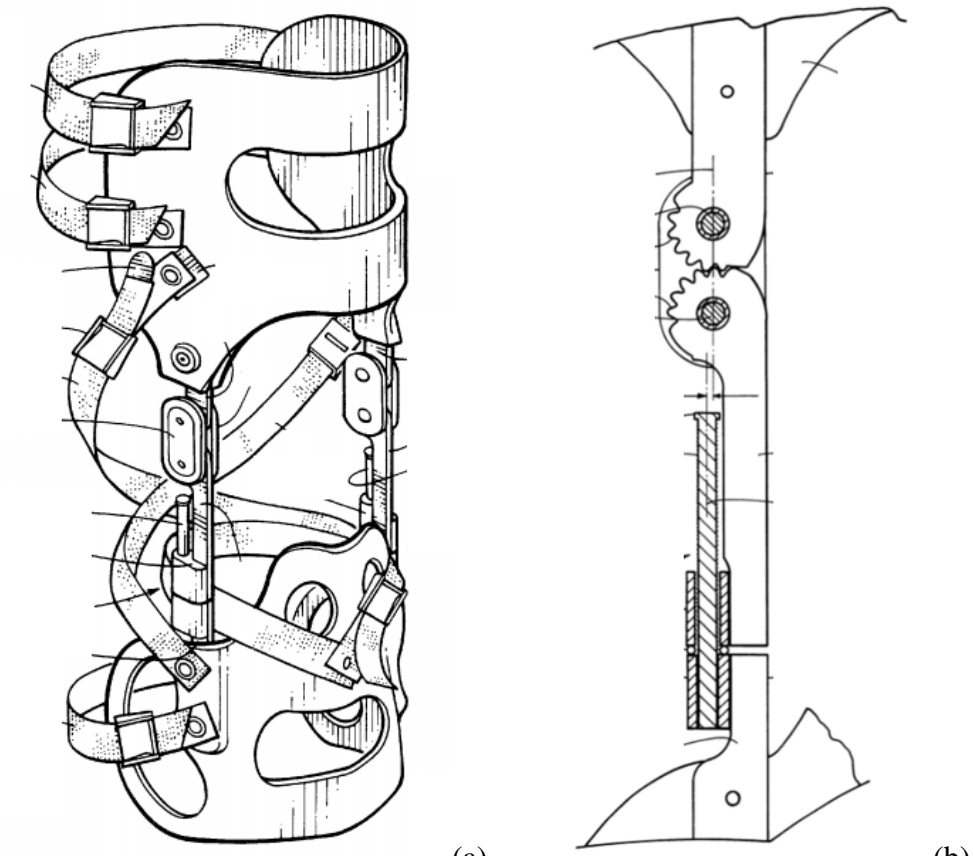

Figure 2.22. Double-hinge gear joint orthosis [45]. (a) Complete orthosis, (b) cap removed to show gears. Labels removed for clarity.

This orthosis comprises thigh and shank components that are connected by an intermediary piece. This intermediary piece has two single-axis hinge joints, resulting in a polycentric double-hinge joint. The thigh and shank bars have meshing gear teeth to ensure that they rotate

at the same rate. Unfortunately, due to the nature of flexion and extension cycling in the knee, the gear teeth are likely to experience wear more rapidly than joints that do not require gear teeth. Though gears can be reliable in an appropriately designed housing, this is not the case in this orthosis.

2.6.3 External Knee Joint Design Based on Normal Motion

Walker et al. designed a polycentric knee joint for a knee brace based on their modelling of the ICR of the biological knee [25]. The joint and prototype developed during this study can be seen in Figure 2.23.

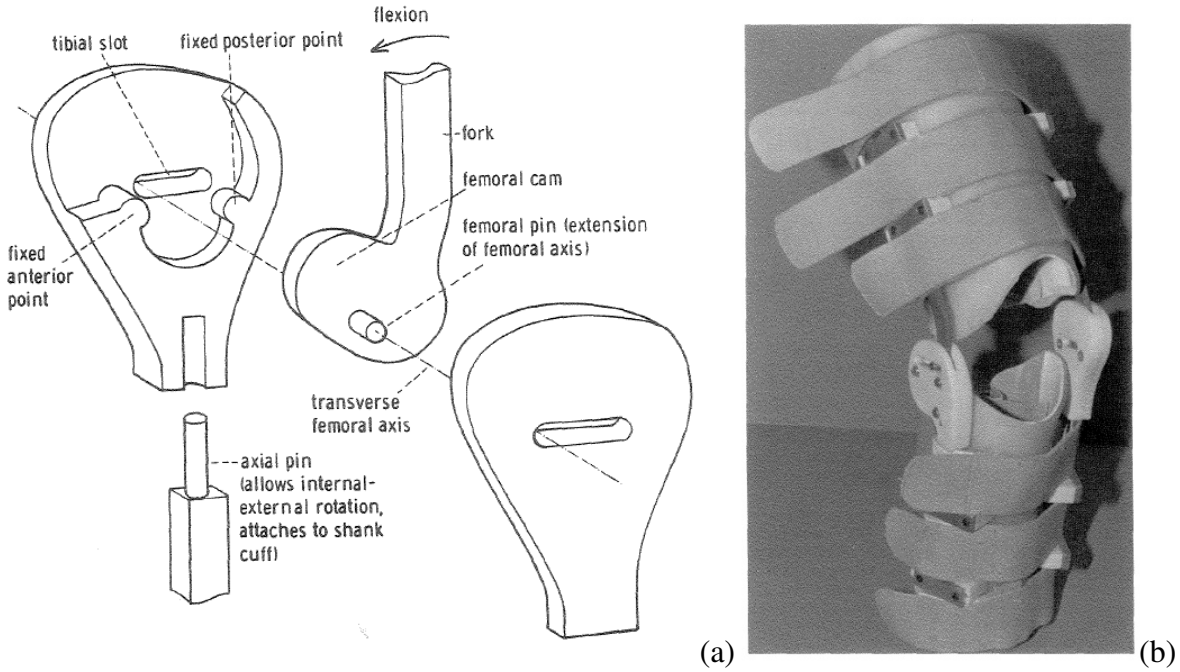

Figure 2.23. External Knee Joint Based on Normal Motion. (a) Exploded view of the joint with identified components, (b) completed knee brace prototype [25]. Public domain.

Using a pin on the femoral component that fits into a slot on the tibial component combined with a cam, this joint effectively follows a pre-defined path of ICR [25]. The shape of the cam was optimized by a computer program and provides the correct amount of translation at a given angle of knee flexion. An axial pin allows for internal-external rotation of the tibial component, allowing this device to align itself in the transverse plane passively [25]. This knee joint design provides a reliable translation path but cannot be implemented in a WAE without alteration, as it is not designed to transfer power. When power is required, other considerations must be made. These considerations will be covered in Chapter 3.

Chapter 3. Design Process

3.1 Kinematic Analysis of Existing Designs

The literature review discussed four distinct knee joint designs: a single-axis joint, the Double-Hinge Gear Joint, the External Knee Joint Design Based on Normal Motion, and a joint with passive ICR translation. A side-by-side comparison is provided in Figure 3.1.

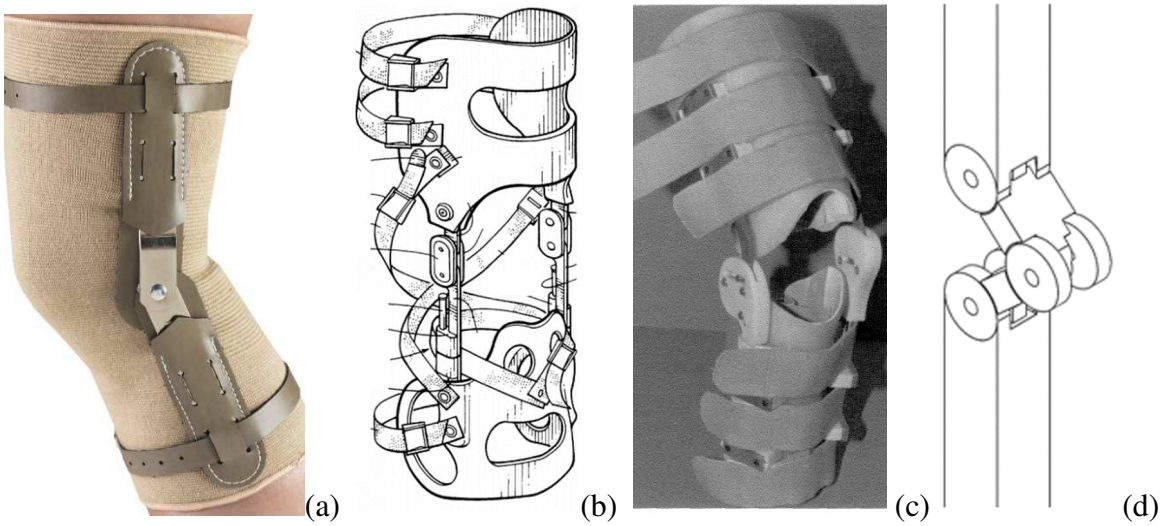

Figure 3.2. Four distinct knee joint designs. (a) Single-axis joint [44]. © 2020 Surgical Appliance Industries, Inc. & Airway Surgical Appliances Ltd., (b) Double-hinge gear joint orthosis [45], (c) External Knee Joint Based on Normal Motion [25]. Public domain. (d) joint with passive ICR translation.

It was deemed critical to analyze these designs analytically and understand their shortfalls to optimize the knee design development process. Using MATLAB, each design is simulated through a complete range of flexion, and their kinematic paths are compared to that of the biological knee. Consequently, the offset in the sagittal plane between the knee designs and the biological joint is determined. Simulations of single-axis joints and joints with a pre-defined path of ICR can be generated reliably. As the interest of this research is focused on joints with pre-determined ICR paths, the first three listed joint types are modelled in MATLAB, and the latter is briefly discussed.

3.1.1 ICR Model

Since Walker et al. considered motions outside the sagittal plane (e.g. internal/external rotation), some assumptions were necessary to convert their model to a 2-dimensional system. Though the center of each femoral condyle has slightly differing pathways throughout flexion/extension, equations (2.1) and (2.2) provide a reasonable basis for modelling the average ICR of the knee. The model developed by Walker et al. represents the intersection of

the transverse axis with the sagittal plane, meaning that the translation defined by these equations represents the midpoint between the medial and lateral femoral condyles. For this research, equations (2.1) and (2.2) will be converted to a new axis system where the x-axis is horizontal in the anterior-posterior direction, and the y-axis is vertical in the proximal-distal direction. The origin (0,0) is identified as the point of the ICR at 0° flexion.

The following equations (3.1) and (3.2) will be used to represent the average translation of the ICR, where x_1 is the translation in the anterior-posterior direction in mm, y_1 is the translation in the proximal-distal direction in mm, and θ is the knee flexion in degrees.

$$x_1 = -0.0602\,\theta + 0.0000178\,\theta^2 \tag{3.1}$$

$$y_1 = -0.05125\,\theta + 0.000308\,\theta^2 \tag{3.2}$$

3.1.2 Single-Axis Joint

Figure 3.3 shows the kinematic incompatibility between the anatomical knee and single-axis joints. Based on the data from [25], the average ICR of the human knee joint is simulated and shown in blue from 0° to 120° flexion. The center of rotation for a single-axis joint is fixed and thus is represented by a single red point.

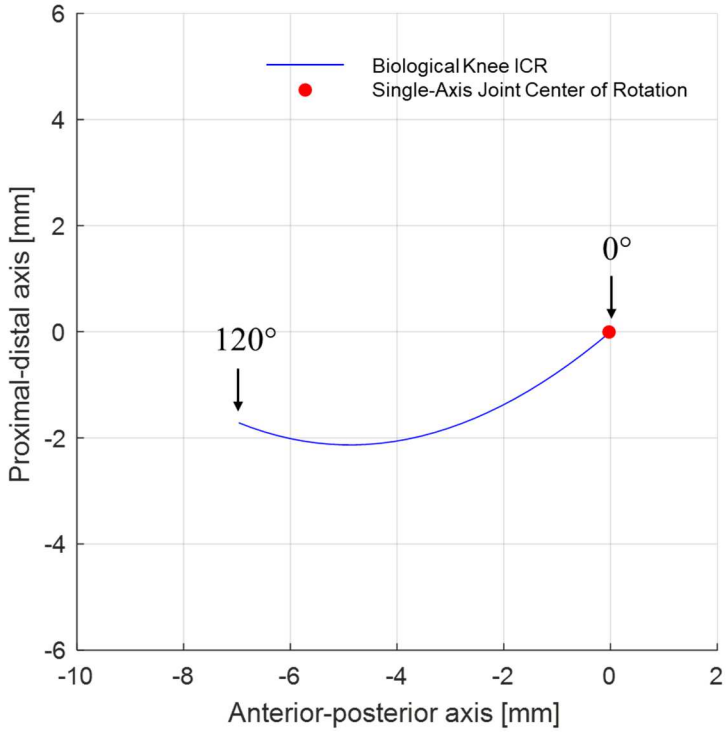

Figure 3.3. Translation of the ICR of an average anatomical knee joint vs. a single-axis joint.

Due to the lack of ICR translation in single-axis joints, offsets occur between the mechanical joint and the biological knee joint. The simulation in Figure 3.4 illustrates this fact. A point at the location of typical shank cuffs was selected at x = 10 mm and y = -70 mm. This point was subjected to a rotation of 120° about the biological ICR, and a curve was drawn. The same point was then rotated about the single-axis hinge joint at (0,0), and a second curve was generated.

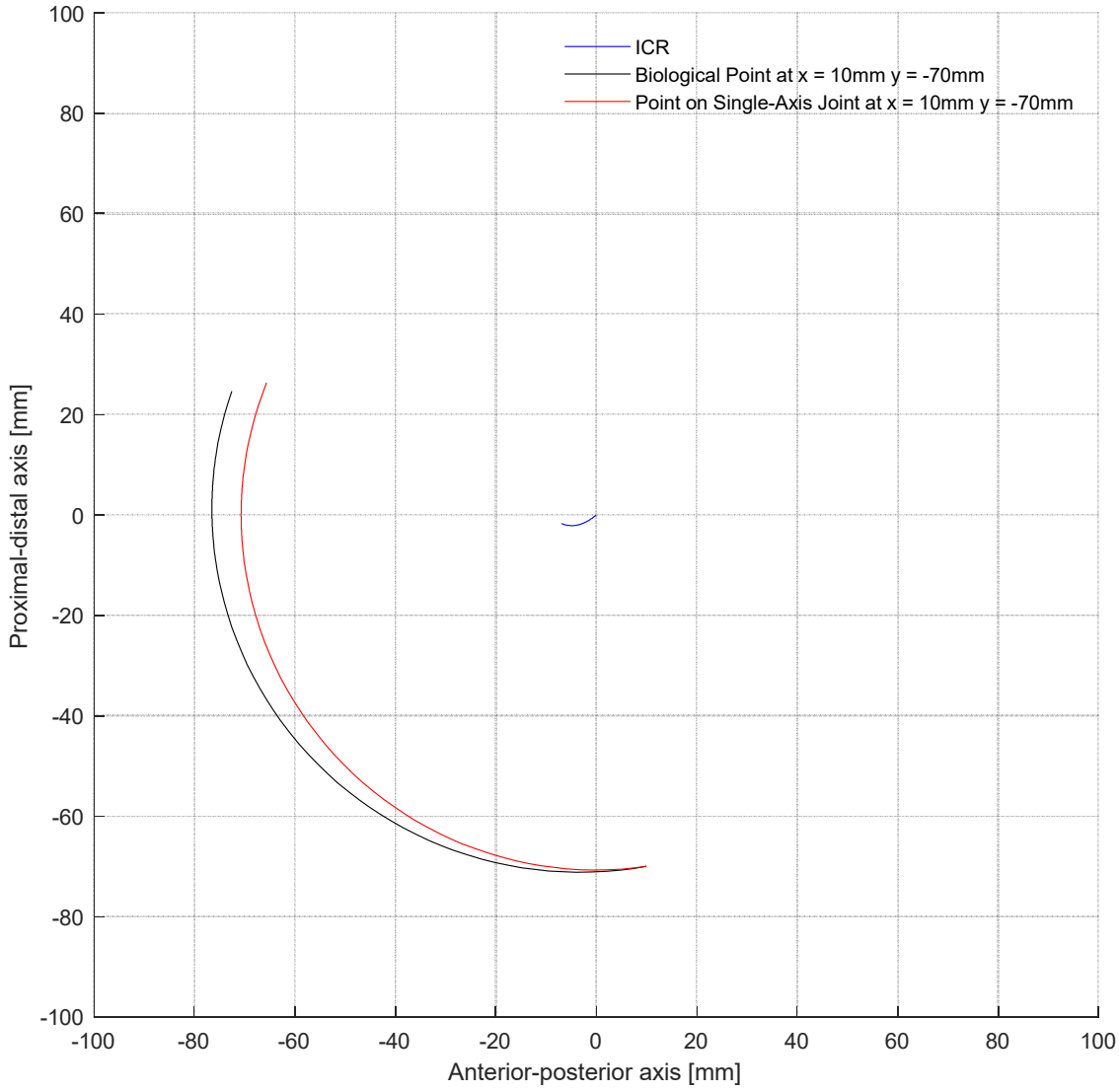

Figure 3.4. Simulation of single-axis joint offset. Point at x = 10 mm and y = -70 mm tracked throughout flexion for biological joint and single-axis joint.

The single-axis joint provides a purely circular path, whereas the biological knee translates throughout flexion. The offset increases as a function of flexion angle which would lead to harmful discomfort to the user. Typical cuff positioning in WAEs can create an offset of

approximately 7 mm at 120° flexion. Therefore, it can be stated that single-axis joints provide poor alignment with the biological knee center and should not be used in powered WAEs, especially when the device transmits considerable force.

3.1.3 Double-Hinge Gear Joint

The Double-Hinge Gear Joint design has a pre-defined path of ICR, as it comprises two circular gears meshing. The femoral component is fixed throughout the simulation to facilitate comparison between the ICR of this device and the model described by Walker et al. Knowing that the ICR of meshing gears is at their point of contact, the ICR path depends on the radius of the gears. Given that the dimensions of the device are not provided by Bhuiyan et al., the models are analyzed at a range of radii. A simulation of this joint between 0° and 120° flexion was carried out in MATLAB and is shown in Figure 3.5.

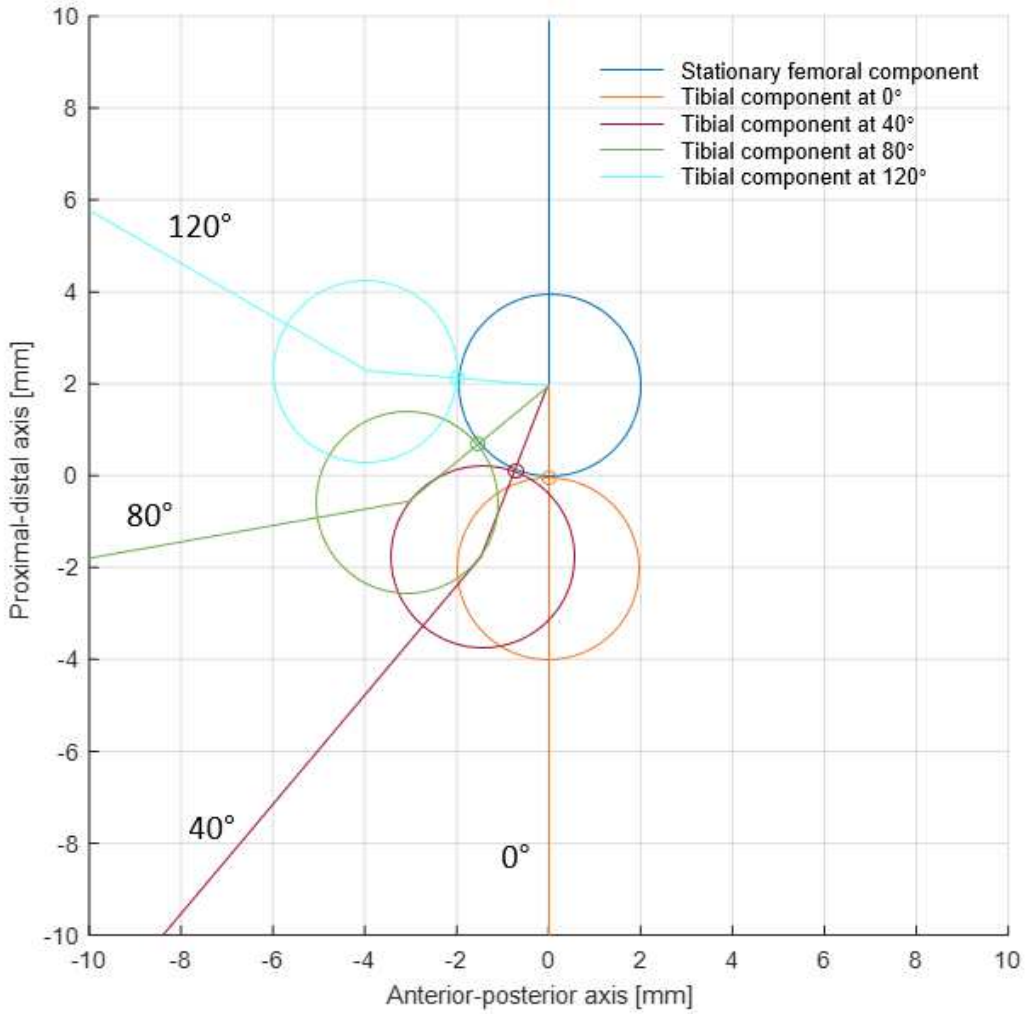

Figure 3.5. Simulation of Double-Hinge Gear Joint. The radius of the gears is 2 mm.

In Figure 3.5, models are drawn at 0°, 40°, 80°, and 120°. The radius of the gears is set to 2 mm, but the figure would look identical with larger radii, simply having a larger scale. Since the femoral component is fixed throughout this simulation, the top gear does not move during flexion. The ICR of the joint is indicated with small circles, neglecting the influence of gear teeth. As seen in Figure 3.5, the ICR is restricted by the location of the top gear and traces a circular shape. The following equations give the x and y coordinates of the ICR of the Double-Hinge Gear Joint.

$$x_{hinge\ ICR} = -r * \sin\left[-\left(\sin^{-1}\left(\frac{\sin(180-\theta)}{2}\right)\right) + \theta\right] \quad (3.3)$$

$$y_{hinge\ ICR} = -r * \cos\left[-\left(\sin^{-1}\left(\frac{\sin(180-\theta)}{2}\right)\right) + \theta\right] + r \quad (3.4)$$

For comparison, the ICRs of the Double-Hinge Gear Joint, the average biological knee from Walker et al. and a single-axis joint have been plotted in Figure 3.6.

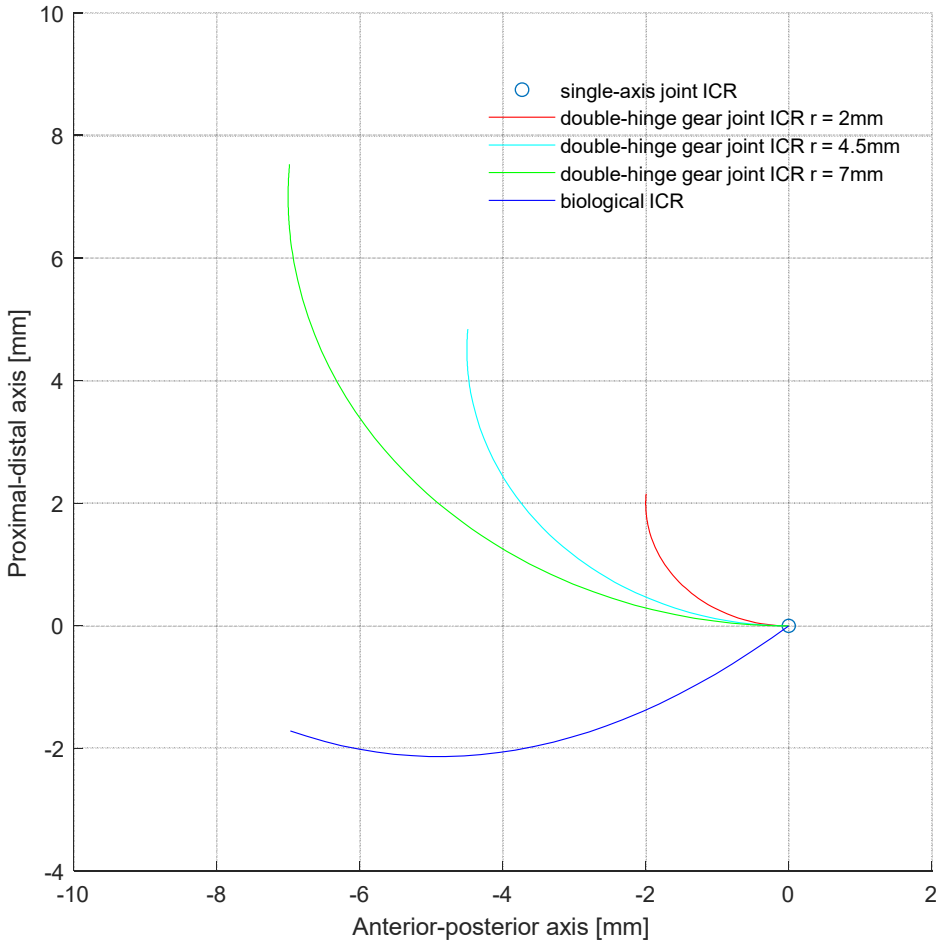

Figure 3.6. ICR comparison of Double-Hinge Gear Joints with varying radii, single-axis Joints, and biological knee.

When simulating different gear radii, it becomes evident that one can prioritize matching the displacement of the biological ICR in the x-axis by setting the radius = 7 mm or prioritize the y-axis displacement by setting the radius = 2 mm. Gears with a radius of 2 mm may be complicated to manufacture and do not achieve enough x-axis translation. Similarly, the 7 mm gears significantly overshoot the y-axis displacement (by approximately 5 mm). If one sets the radius to a value in the middle of the two, 4.5 mm, a compromise is achieved between x- and y-axis displacements. This is an improvement over the 2 mm and 7 mm gears, but there is still a significant difference between the ICR of this joint and the biological knee. A perfectly designed joint with a pre-defined path of ICR would have a trajectory identical to the blue line. Thus, this design is not ideal.

To visually compare the offset between the Double-Hinge Gear Joint, a single-axis Joint and the average biological knee, a simulation similar to Figure 3.4 was generated.

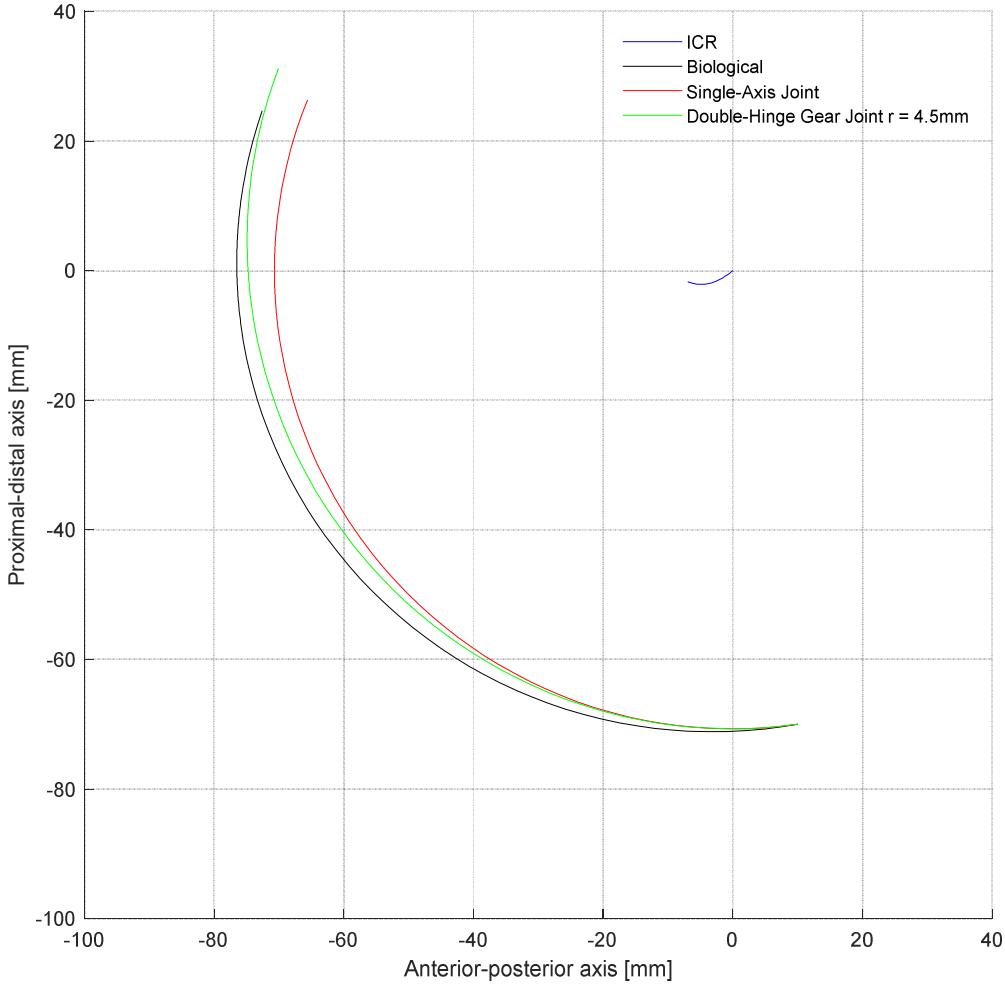

Figure 3.7. Simulation of Double-Hinge Gear Joint offset. Point at x = 10 mm and y = -70 mm tracked throughout flexion for biological joint, single-axis joint, and Double-Hinge Gear Joint.

Visibly, the Double-Hinge Gear Joint (at 4.5 mm gear radius) has smaller offset magnitudes than the single-axis Joint. Though it is an improvement, this design remains insufficient as it does not suit the kinematics of the biological knee.

3.1.4 External Knee Joint Design Based on Normal Motion

Since the External Knee Joint Design Based on Normal Motion is designed on the principle that it has the same ICR as the biological knee joint, evaluating its kinematics theoretically is fruitless. For simulation and later comparison purposes, a point will be chosen on the tibial component and tracked through space throughout the ROM of the joint. The point selected is at the same coordinates as in section 3.1.1, x = 10 mm and y = -70 mm, since this is a common placement of shank cuffs.

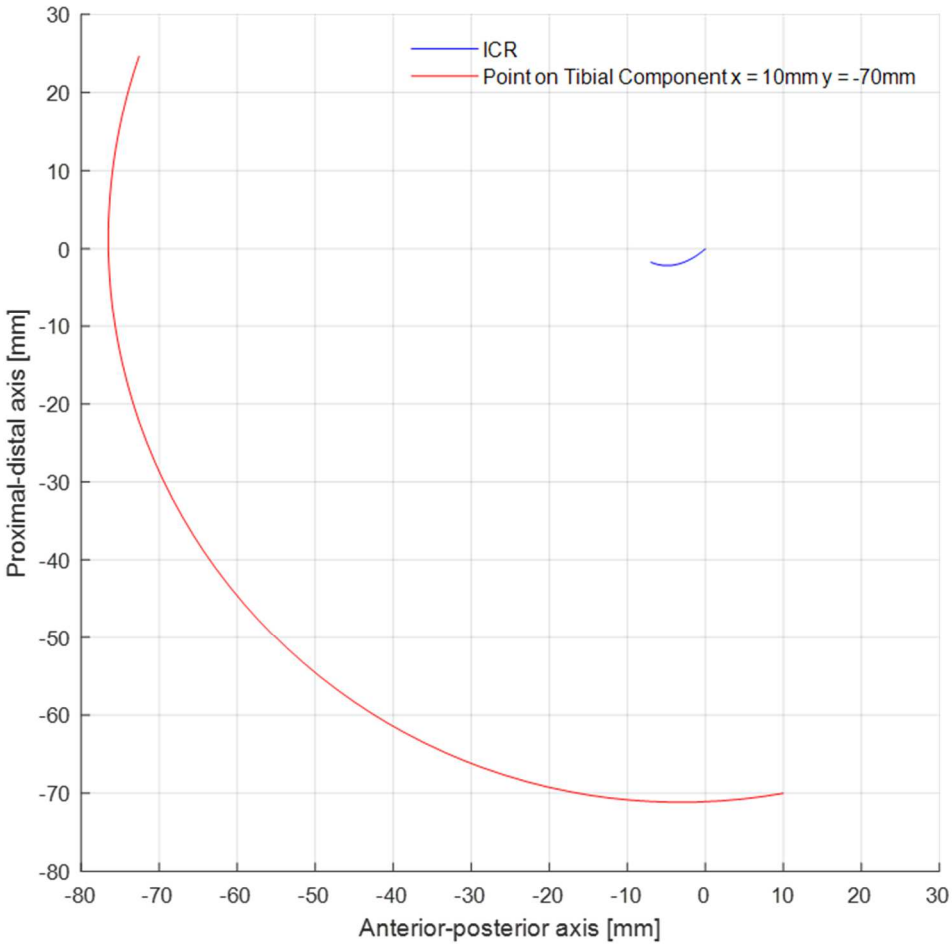

Figure 3.8. Simulation of External Knee Joint Based on Normal Motion.

Since the ICRs of the device and the biological knee model are identical in this simulation, they are both represented by the blue curve. Theoretically, this design is an ideal kinematic match for the biological knee.

3.1.5 Joint with Passive Translation of the Instantaneous Center of Rotation

Compared to joints with pre-defined ICR paths, passive ICR translation may allow for improved alignment between the biological and exoskeleton joint axes. This being said, a well-designed joint that uses a pre-determined ICR path may be just as effective as passive translation. Due to the variability and unpredictability of joints that allow passive ICR translation, they cannot be reliably simulated and will not be considered in this analysis.

3.2 Force Transfer Analysis of Existing Designs

In powered WAE knee joints, effective force transfer is crucial. For this reason, a brief qualitative kinetic analysis of the four joint types discussed in section 3.1 follows. Although they have been shown to be kinematically incompatible with the biological knee, single-axis

joints are very efficient for force transfer. They are reliable and can endure a significant number of repeated cycles. Single-axis joints can redirect applied forces easily and via several methods. A pulley can be located at the hinge, and a cable can transfer the load, simply changing its direction. A rotational actuator can also be placed in line with the joint and apply torque directly, but this configuration tends to be bulkier and more inconvenient.

Double-hinge gear joints are also reliable joints but are more complex in their method of transferring force. A cable and pulley system can be implemented, but the pulley(s) must be standalone from the gears themselves as they move relative to each other. In this type of joint, rotational actuators cannot be placed directly in line with the biological joint due to the relative gear center displacement. Double-hinge gear joints have a shorter lifespan than single-axis joints but are nonetheless relatively reliable. They wear more quickly due to the meshing gear teeth.

The External Knee Joint Design Based on Normal Motion by Walker et al. is a polycentric joint with a pre-defined path of rotation. Because it falls within this type of joint design, wear is predictable via simulations. For this study, the analysis will remain qualitative. Though not designed to transfer force, this joint is similar to the Double-Hinge Gear Joint from a kinetic force transfer perspective. It could also be integrated with a cable and pulley system, and pulleys would have to be additional to the existing design. Additionally, it is incompatible with the placement of a rotational actuator in line with the joint.

As previously stated, joints with passive ICR translation cannot be reliably simulated. Thus, it is difficult to predict their efficiency in force transmission and wear resistance. Powered joints with passive ICR translation such as the iT-Knee [5], Self-Adjusting Isostatic Exoskeleton [16], AssistOn-Knee [17], S-Assist [6], and the Adaptive Coupling Joint [41] are highly complex and tend to be bulkier. This is because rotations and translations are decoupled to transfer force in a passive joint, and the force must be able to cross the joint in more than one way to avoid offset.

3.3 Design Objective

Though significant progress has been made in WAE development, the literature review and the previously presented design analyses have demonstrated the inadequacy of current WAE knee joint designs. Studies have suggested that incompatibilities between the mechanical and the biological joints can be mitigated by using a polycentric knee joint that would eliminate

kinematic offset [25]-[27],[34],[46]. Orthoses, which have been researched for a more extended period, have made more advancements in this regard. Due to the inherent intricacies of kinematically biocompatible joints and the increased complexity of injecting an external force into a system, polycentric joints have been minimally included in powered exoskeletons.

In order to achieve the required performance in powered WAEs, a novel knee joint must be developed. This thesis proposes a novel knee joint design inspired by knee orthoses that can be adapted to the needs of powered exoskeletons.

From a kinematic perspective, the joint must be polycentric to emulate the motion of the natural knee; however, it must also transfer force reliably and assist the actuation system with optimal force delivery. The aim is to have a resulting knee joint design compatible with various actuators, with varying moment arm throughout flexion. The variation of moment arm not only changes the magnitude of the moment but also changes the rate of flexion. Biologically, this change in moment arm causes the amount of linear contraction by the muscle to decrease at high flexion angles.

Finally, the design should be modular and adaptable so that it can be positioned at different locations that include offset configurations. Based on these requirements, design criteria are proposed in section 3.4.

3.4 Design Criteria

The design of a novel polycentric powered knee joint for WAEs must satisfy the following criteria:

1. Develop a polycentric knee joint with the ability to transfer force from an actuator.
2. The joint must be able to vary the moment arm throughout flexion.
3. The joint must accommodate offsets of the knee joint in the sagittal plane.
4. The ROM of the joint must be 0° to 120° flexion.
5. Physical restrictions must be implemented to avoid hyperextension knee injuries.
6. The design must allow the actuator to be placed proximally to the knee to reduce inertia and felt weight.
7. The design must be compact and light.

3.5 Design Concept

Based on the design criteria set in section 3.4, several design concepts were considered and analyzed. Given the characteristics of the required device, a joint design with a pre-defined path of ICR was deemed the most favourable. This is the type of joint identified as type (b) in

Figure 2.20. The device possesses a pre-defined path of rotation to match the average ICR translation of the biological knee. The ICR model shown in section 2.2.3 is used as a reference for biological knee kinematics.

Based on the design analysis in section 3.1.4, the External Knee Joint Design Based on Normal Motion designed by Walker et al. is deemed adequate to serve as inspiration. The pin-in-slot design restricts the ROM and prevents hyperextension without the need for an additional stopping mechanism. While this design achieves ideal kinematics, it does not meet the moment arm and modular design requirements for powered WAE integration. Consequently, a preliminary design concept is developed to achieve the design objectives outlined in section 3.4. SolidWorks was used to draft the model, which is shown in Figure 3.9.

Figure 3.9. SolidWorks assemblies of the joint design concept. A tibial component with pins is shown between two femoral components that have slots. (a) Intact assembly, (b) exploded view.

Depending on the actuator, a cable or belt is favoured to transfer energy from various types of actuators through the joint. In order to facilitate this, a cable must be guided along a surface. Thus, a pulley is integrated into the joint. Since the moment arm is a key parameter for a joint that mimics the behaviour of the biological knee, the outer shape of the pulley that controls force transmission is noncircular. This allows change in the moment arm throughout flexion, similar to the biological knee's functionality.

In order to prevent injury, the ROM of the joint will be restricted using a pin-in-slot design where pins move along slots to dictate the kinematics of the joint and prevent hyperflexion

and hyperextension. Initially, the design was generated with only two pins, but due to the physical construction of the design, a third was added for increased stability and reliability. The third path was identified by choosing a point relative to the first two pins at full extension and tracking its movement throughout flexion. Figure 3.1 shows the initial and revised path designs.

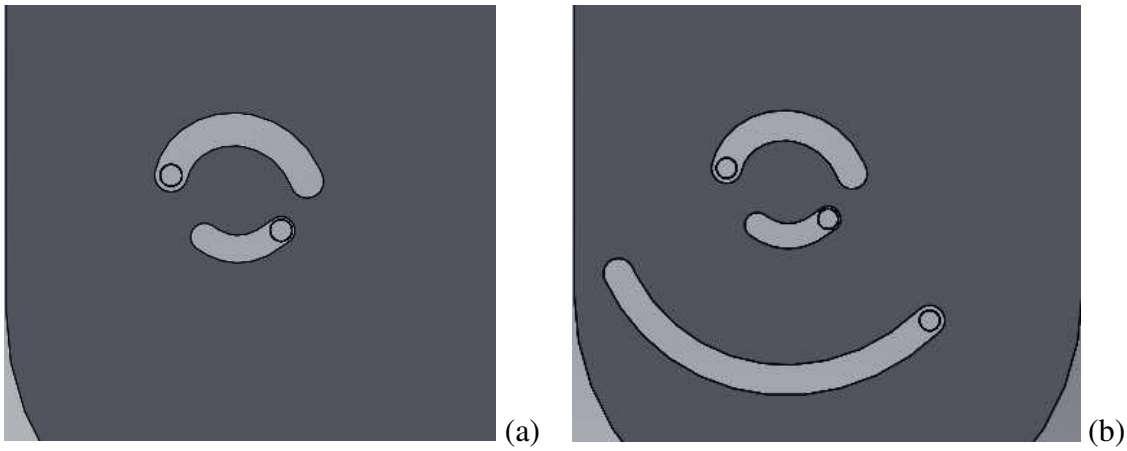

Figure 3.10. Detailed view of the pin-and-slot mechanism of the joint. (a) Initial two-pin design. (b) Revised three-pin design for increased stability and reliability.

The placement of bushings on the pins would minimize friction between the pins and their paths, though, for simplicity, bushings will not be depicted in renderings.

As shown in Figure 3.9, slots are located on the femoral component, and pins are fixed to the tibial component. Three pins are implemented in the design, as previously described. One of the pins is aligned with and represents the ICR, allowing for kinematic compatibility with the biological knee. A second pin has the purpose of ensuring that the first pin moves along its path at the appropriate rate, and the third pin provides extra stability and ensures that there is only one DOF. Ensuring a single DOF means that only one kinematic solution is available throughout movement and improves the reliability of simulations. If multiple DOFs were present, simulations would be difficult to generate, and device behaviour would be challenging to predict.

This design effectively ensures kinematic reliability as it restricts the device's flexion ROM. Due to the inherent ROM restrictions that come with pin-in-slot designs, additional stoppers are not required. At the end of the ROM, pin motion is restricted by the end of the slots. Thus, the joint prevents hyperflexion and hyperextension. The process of determining the shapes of the slots is discussed in detail in sections 4.1.1.1 and 4.1.2.2.

The device is actuated using a cable and pulley system to allow for flexibility in the future placement of the actuator. This would allow the actuator to be placed close to the user's center of mass, thereby reducing felt weight and energy expenditure. The cable, which is not depicted in SolidWorks renderings, is routed from the posterior side of the femoral component around a pulley on the tibial component and back up the anterior side of the femoral component. Two small pulleys were designed to be fixed anteriorly and posteriorly on the proximal end of the femoral component. These pulleys would act as pretensioners for the cable and help guide the cable along the component. This cable is fixed to the pulley of the tibial component with a pin. The pretensioner pulleys and pin locations are indicated in Figure 3.11 by black 'x' markers and a yellow point, respectively.

Figure 3.11. SolidWorks assembly of joint without offset. Cable and bushings not depicted. Location of pretensioner pulleys indicated by black ‘x’ markers and location of pin indicated by a yellow point.

The fixation of the cable to the pulley is to allow for force transmission. To flex and extend the joint, tension is applied to the posterior and anterior ends of the cable, respectively. When tension is applied to the cable, force is transferred from the actuator to the tibial component via a pin. The moment arm, which is measured from the outer edge of the pulley to the ICR of the device, varies throughout flexion. The applied force causes the joint to flex or extend, and the pins in slots dictate the kinematics throughout motion. This means that the shape of the slots controls the rate of rotation and translation of the joint and is designed to mimic the kinematics of the biological knee.

Unlike the single-axis joint, the Double-Hinge Gear Joint, and the External Knee Joint Design Based on Normal Motion, this new design concept was created to accommodate an offset in the sagittal offset. If the device cannot be aligned with the biological knee due to mechanical restrictions, an alternative shape can still allow the rolling and sliding motion of the knee.

In this case, the first pin (aligned with the ICR of the knee in the original design) becomes a virtual point in space, and three pins are displaced away from the ICR. A joint model that takes prescribed offset into account was created (this is shown in more detail in section 4.1.2). Figure 3.1 provides the SolidWorks model for the joint with offset. The actuating cable and cable-routing components have been excluded from the SolidWorks model for simplicity.

Figure 3.12. SolidWorks assemblies of joint with offset. (a) Intact assembly, (b) exploded view. Location of pretensioner pulleys indicated by black ‘x’ markers in (a), and location of pin indicated by a yellow point in (b).

Chapter 4. Modelling and Simulation

4.1 Modelling of Design Concept

The selected design concept shown in Chapter 3 should theoretically match the ICR model of the biological knee developed by Walker et al. To prove this, the modelling process of the joint design will be presented. This section is divided into two parts: the first describes the design with no offset, and the second provides an example of the modular design with offset.

4.1.1 Joint with no Offset

This model assumes no initial offset between the device and the biological joint, meaning that it is aligned with the biological ICR, located at (0,0) at 0° flexion.

4.1.1.1 Kinematics/Paths

The locations of pins 1, 2, and 3 are modelled from 0° to 120° flexion to validate the kinematic requirement that the design should match the translation of the ICR of the biological knee model outlined by Walker et al.

The path associated with pin 1 precisely follows the ICR model. Thus, the ICR is represented by x_1 and y_1 from equations (3.1) and (3.2), respectively. Pin 1 is therefore located at the center of the femoral condyle (0,0) at 0° flexion. Having placed pin 2 at prescribed x and y values away from pin 1, a corresponding path 2 was calculated and is represented by the parametric equations for x_2 and y_2. The location of pin 2 with respect to pin 1 can be described by the variables $x_{2\,Diff}$ = 10 mm and $y_{2\,Diff}$ = -10 mm, meaning that pin 2 is located at (10,-10). The locations of the pins were determined by trial-and-error and their paths were validated via modelling.

The distance from pin 1 to pin 2 can be found using the Pythagorean theorem as follows:

$$d_{1\to2} = \sqrt{\left(x_{2\,Diff}\right)^2 + \left(y_{2\,Diff}\right)^2} \tag{4.1}$$

To find the coordinates for path 2 that correspond with knee flexion angles of 0° to 120°, first, the angle between the $d_{1\to2}$ vector and the y-axis must be found and is denoted by θ_2.

$$\theta_2 = \left|\tan^{-1}\left(\frac{x_{2\,Diff}}{y_{2\,Diff}}\right)\right| \tag{4.2}$$

Finally, parametric equations for path 2 were developed as follows:

$$x_2 = x_1 + d_{1\to2}(\sin(\theta_2 - \theta)) \tag{4.3}$$

$$y_2 = y_1 - d_{1\to2}(\cos(\theta_2 - \theta)) \tag{4.4}$$

Using the same process for pin 3 with values of $x_{3\,Diff} = -10$ and $y_{3\,Diff} = 5$, path 3 is described by equations (4.5) and (4.6).

$$x_3 = x_1 + d_{1\to3}(\sin(\theta_3 - \theta)) \tag{4.5}$$

$$y_3 = y_1 - d_{1\to3}(\cos(\theta_3 - \theta)) \tag{4.6}$$

Figure 4.1 is a simulation from MATLAB that shows the paths of the three pins from 0° to 120° flexion. Path 1 is blue and coincides with the ICR, path 2 is red, and path 3 is black. The locations of the pins at 0° flexion are indicated with points in their corresponding colours.

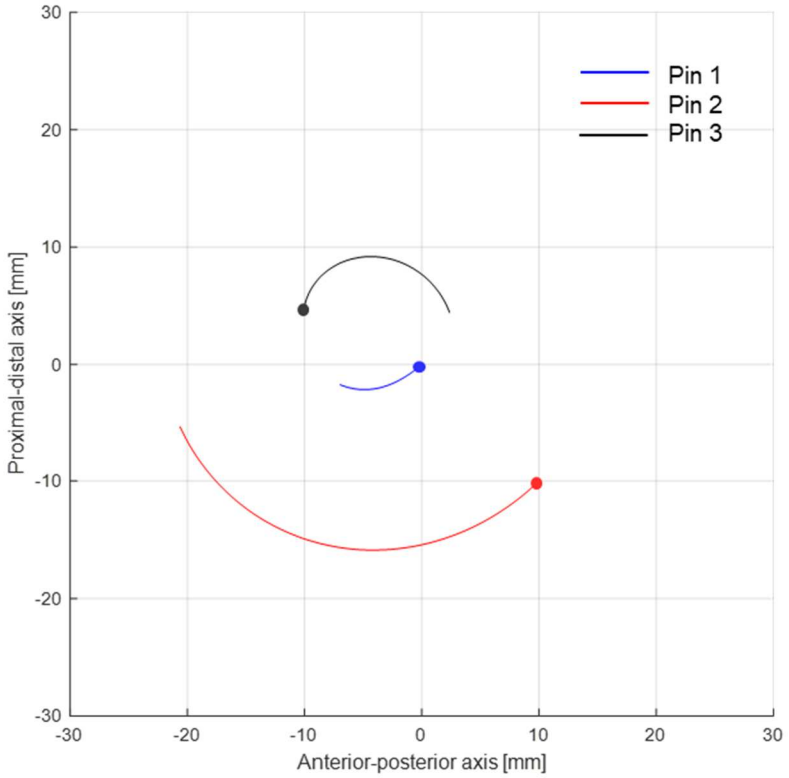

Figure 4.1. Design concept with no offset.

Subsequently, to model the movement of the pins, lines connecting the pins were drawn at 15° intervals throughout the ROM. An infinite number of lines could be drawn, but eight were selected for clarity and consistency between experimental tests. Figure 4.2 demonstrates the location of the pins at different degrees of flexion, which is later validated experimentally.

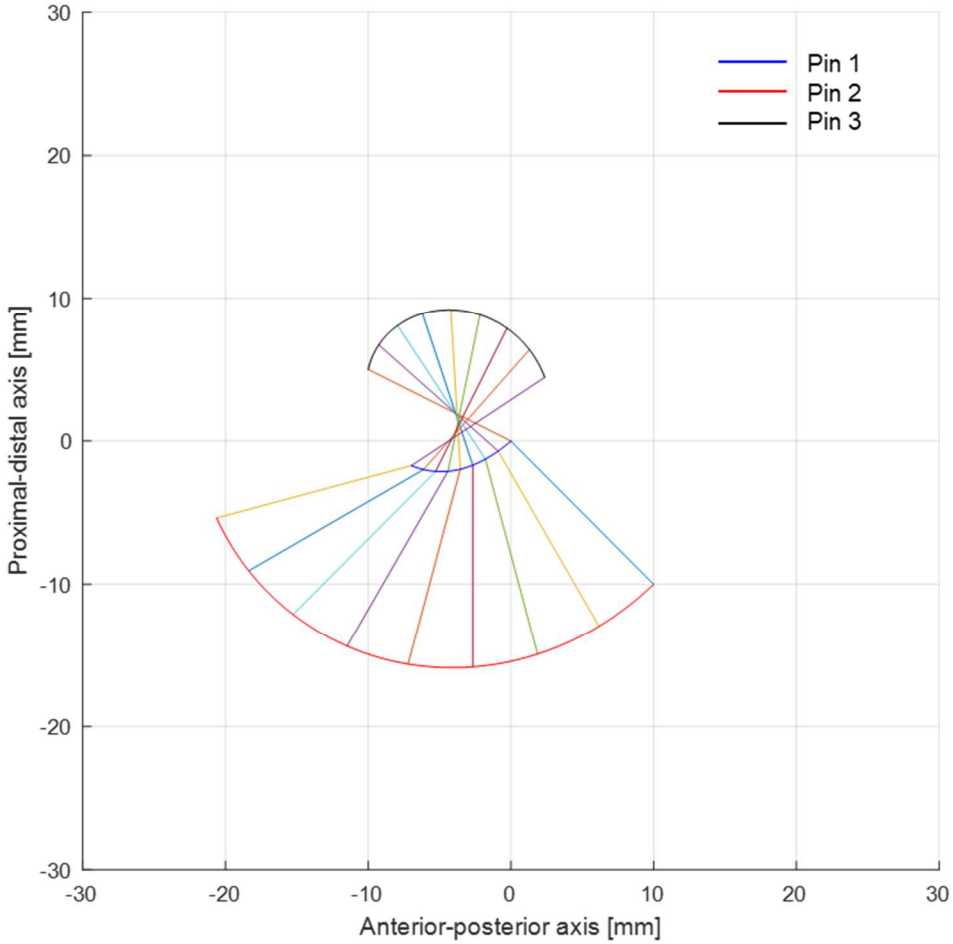

Figure 4.2. Design concept with no offset. Multicolored lines connecting pin 1 to pin 2 and pin 3 are drawn at 15° intervals between 0° and 120°.

In order to compare this joint to the External Knee Joint Design Based on Normal Motion, the same point at the location of a shank cuff is modelled. This point is located at x = 10 mm and y = -70 mm when the joint is at 0°, and is tracked from 0° to 120° flexion.

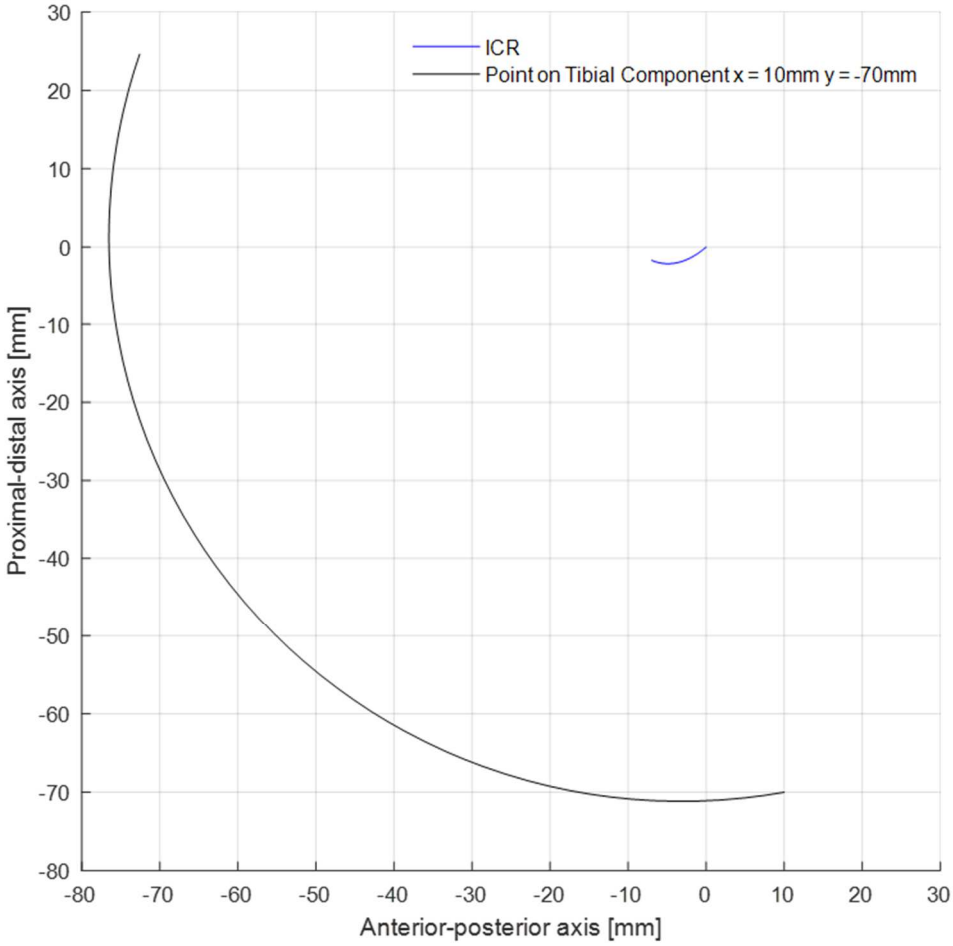

Figure 4.3. Simulation of joint with no offset.

The curve tracking the location of the specified point is identical to that of the External Knee Joint Design Based on Normal Motion in simulations, shown in Figure 3.8. This is because both simulations and joint designs revolve around the same ICR path. Theoretically, both joints should produce identical behaviour, but this cannot be verified without experimental validation as variations will be caused by manufacturing methods and the design of the rest of the device structure.

In order to confirm that this joint design permits exactly 120° flexion, the SolidWorks assembly was evaluated. Figure 4.4 provides a lateral side view of the joint at the ends of its ROM. Pins are identified in the same colours as shown in Figure 4.1.

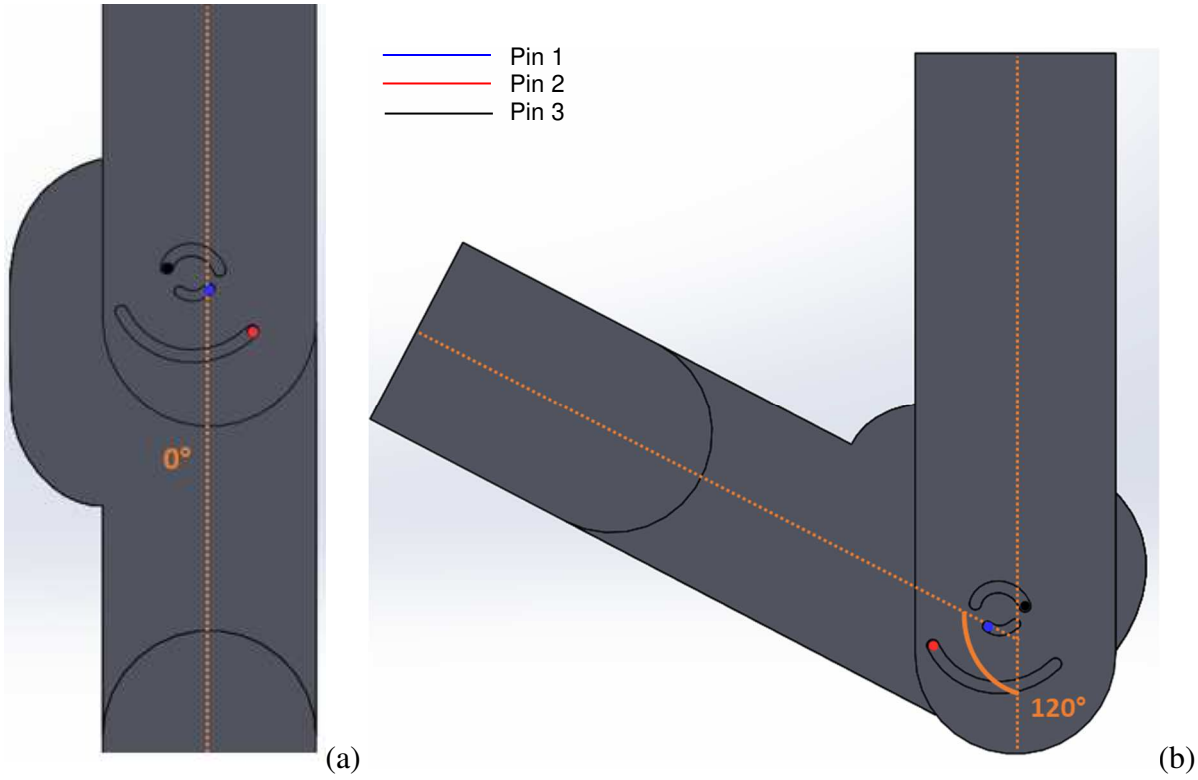

Figure 4.4. SolidWorks model of the joint with no offset at ends of the ROM. (a) 0° flexion, (b) 120° flexion.

As desired, at maximum and extension and flexion, the component centerlines form angles of 0° and 120°, respectively. This model supports the hypothesis that the joint will maintain the same ICR as the biological knee and shows that the pins will act as stoppers to prevent excessive extension or flexion of the joint.

4.1.1.2 Moment Arm

Since this design is intended to be integrated into a powered WAE, it is essential to consider the changing moment arm in the knee throughout flexion during the design process. Considering the design uses a cable for force transmission, using a noncircular pulley minimizes the contraction distance required. The contraction distance is reduced at high degrees of flexion, thereby reducing the total amount required.

The rate of change in moment arm is the most crucial aspect to consider when designing the shape of the noncircular pulley, as it permits efficient joint flexion. Before the required profile of the noncircular pulley can be determined, the moment arm of the biological knee had to be investigated. Figure 4.5 expresses the data found in Figure 2.11 as percentages of the maximum moment arm value.

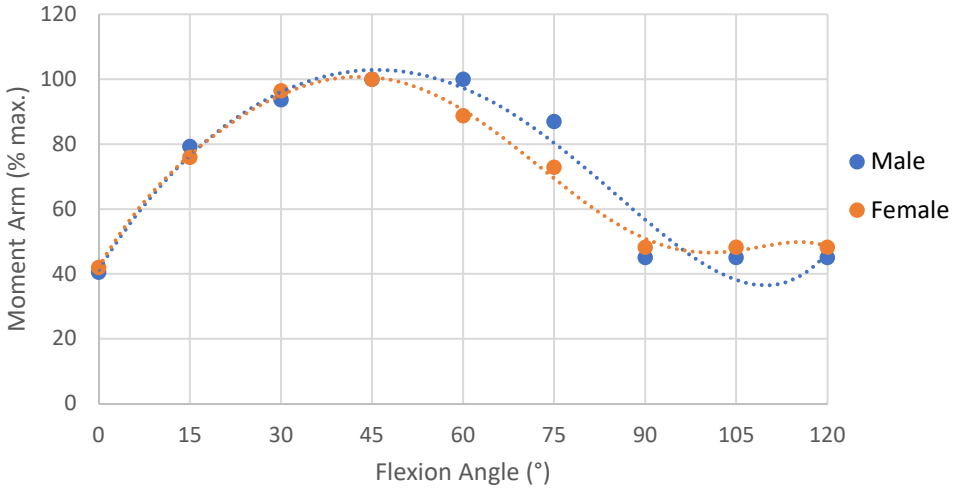

Figure 4.5. Percent maximum knee moment arm vs. knee flexion angle from male and female adults from 0° to 120°.

Both male and female curves did not change shape between Figure 2.11 and Figure 4.5. The maximum values are set to 100%, and all other values are proportionally converted to percentages. Note that the curve-fit goes past 100% but does not represent the actual value.

The literature review in section 2.3 demonstrates that the moment arm increases from 0° to approximately 45° and returns to its original value at 90° flexion. For the purposes of this research, data for male patients will be used, but calculations and design variables could certainly be recomputed using female moment arm values.

To determine the required profile of the noncircular pulley, a reference frame must be identified. θ is measured at the location of the ICR and represents the degree of flexion. Here, the femoral component is kept vertical. θ measures the angle between the centerline of the tibial component and the vertical, and Figure 4.6 provides a visual representation of this reference frame. The yellow dotted lines are vertical and represent the femoral centerline, and the red lines represent the tibial centerline at 15° intervals.

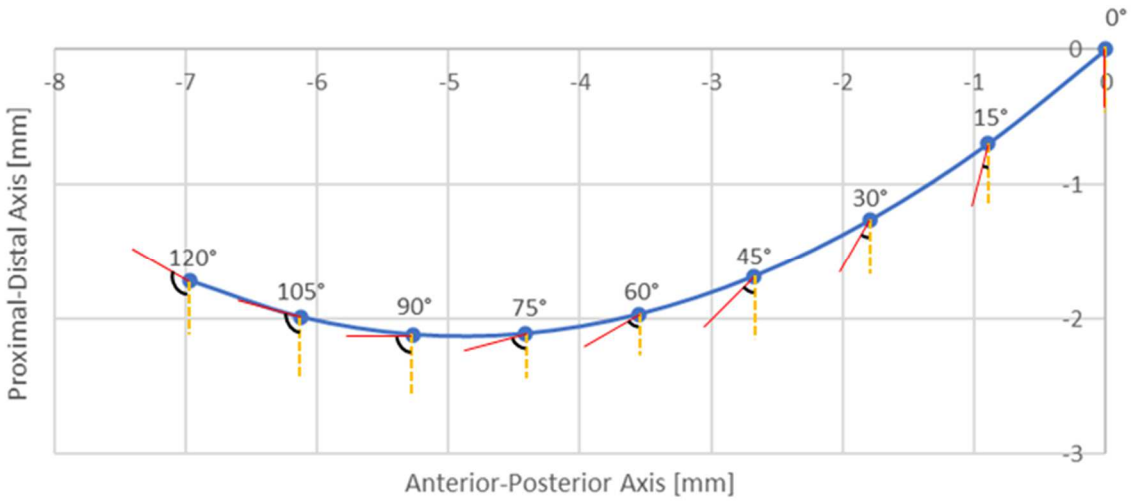

Figure 4.6. Biological instantaneous center of rotation reference. The yellow dotted lines represent the femoral centerline, and the red lines represent the tibial centerline at 15° intervals.

The pulley coordinates were determined under the assumption that the location of applied force is the last point of contact between the cable and pulley. Though several pulley shapes of different moment arm magnitudes were generated, sample calculations will be shown for the design at 100% of the magnitudes shown in Figure 4.5.

In order to develop the first iteration of the pulley shape, coordinates were located as follows.

$$x_{p1} = x_1 - Mcos(\theta) \tag{4.7}$$

$$y_{p1} = y_1 - Msin(\theta) \tag{4.8}$$

where M is the magnitude of the moment arm in mm, (x_1, y_1) are the coordinates of pin 1 in mm, and θ is the flexion in degrees. The coordinates of the first pulley shape iteration can be seen in Figure 4.7.

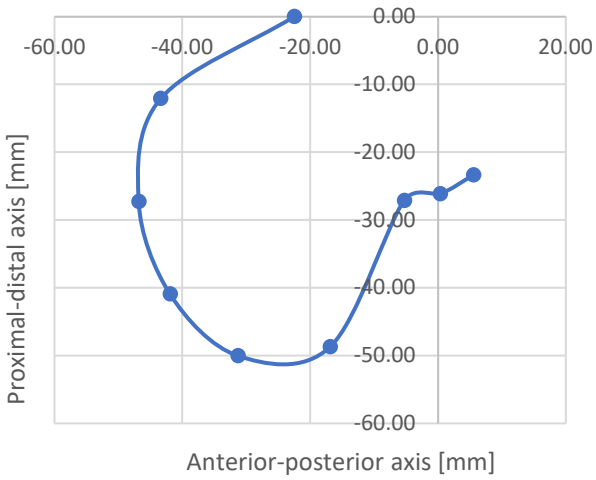

Figure 4.7. Coordinates of first pulley shape iteration.

The physical design must be considered to validate this pulley shape. As the cable is routed down the femoral component and is wrapped around the pulley on the tibial component, it is vital that the cable contacts the entire surface of the pulley. Otherwise, the moment arm calculated using the coordinates of the pulley will not coincide with the moment arm generated by the cable's position. A sketch of the first pulley shape iteration is shown in Figure 4.8.

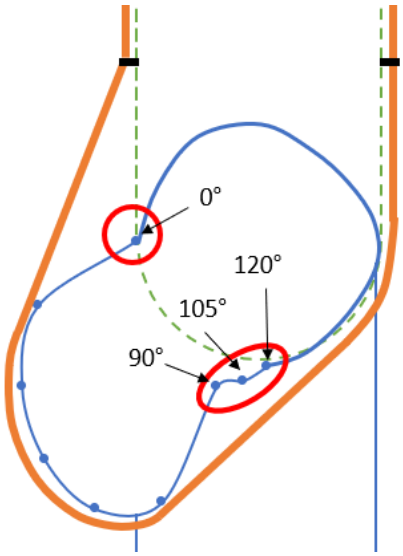

Figure 4.8. Sketch of the first iteration of the pulley shape. Areas of concern are circled in red.

The pulley and tibial component to which it is fixed is drawn in blue. An orange line represents the cable, the femoral component is indicated by a dotted green line, and the black rectangles symbolize pretensioner pulleys fixed to the femoral component to guide the cable. It is visible and indicated in red that the cable does not contact the pulley at 0°, 90°, 105° and

120°. Unfortunately, the cable cannot be guided along this pulley shape with a track or several smaller pulleys. This is because as the joint flexes and the tibial component rotates, the cable cannot contact degrees of flexion below its current degree. This is demonstrated in Figure 4.9.

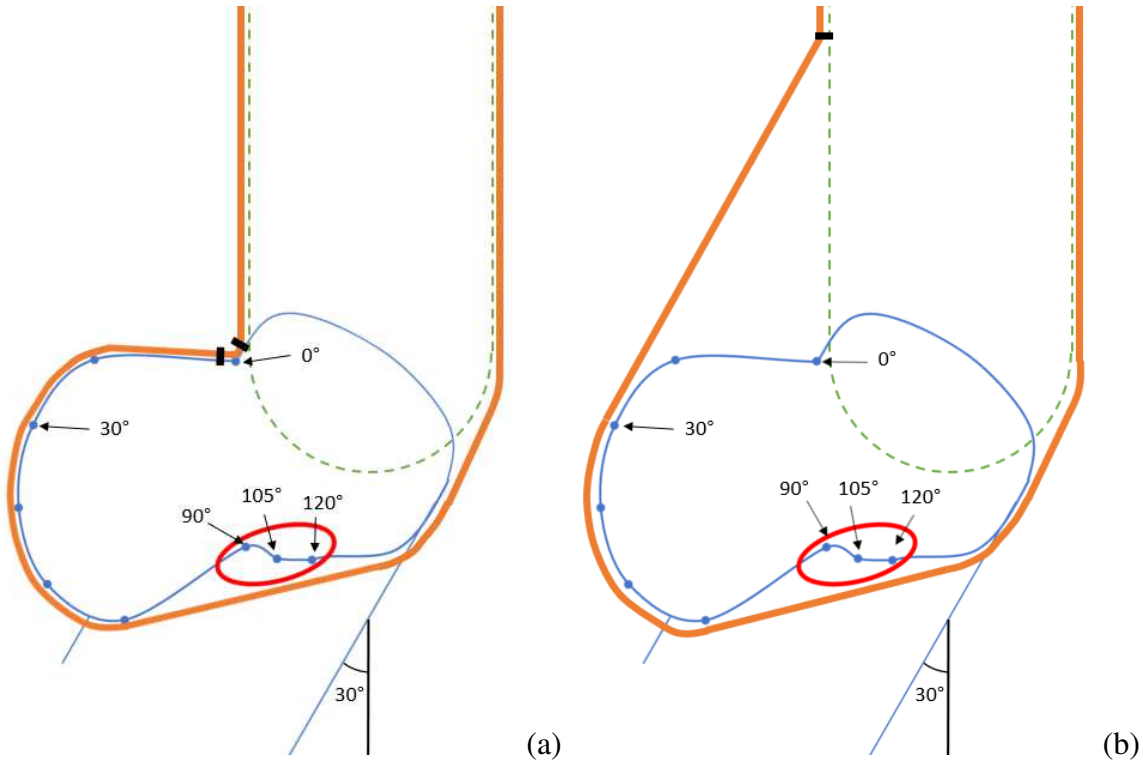

Figure 4.9. Sketches of the first pulley shape iteration at 30° flexion. (a) Cable is guided along the shape of the pulley with added smaller pulleys. (b) Cable is free to move away from the pulley.

Figure 4.90 presents two cases of the joint at 30° flexion. In (a), smaller pulleys have been added on either side of the 0° point to ensure cable contact at that point. When the joint is flexed, the last point of contact is still approximately at 0°, meaning that the moment arm is not being measured from the desired 30° point. In (b), the design is demonstrated with a single pretensioner pulley fixed to the femoral component. Here, as designed, the last point of contact between the cable and the pulley is at the 30° point.

Since the cable cannot be guided along the entire length of the pulley, the pulley's shape must be altered. The first two coordinates of the pulley shape (0° and 15°) had to be moved further out to be in line vertically with the point that protrudes the furthest posteriorly (30°), thereby increasing the moment arm at 0° and 15°. This change is reflected in (4.9).

The moment arm of the biological knee decreases after 90° flexion, which is unfortunately unachievable with this type of design. With an applied tensile force, the cable will always take the shortest path and not contact these pulley portions. For this reason, coordinates between 75° and 120° were interpolated to create a straight line. This can be seen in (4.10).

The coordinates for the final pulley shape were located as follows.

$$x_{p2} = \begin{cases} if\ \theta < 30° & x_{p1\ @\ \theta=30°} \\ if\ \theta \geq 30° & x_{p1} \end{cases} \tag{4.9}$$

$$y_{p2} = \begin{cases} if\ \theta \leq 75° & y_{p1} \\ if\ 75° < \theta < 120° & \dfrac{(x_{p2} - x_{p2\ @\ \theta=75°})(y_{p2\ @\ \theta=120°} - y_{p2\ @\ \theta=75°})}{x_{p2\ @\ \theta=120°} - x_{p2\ @\ \theta=75°}} + y_{p2\ @\ \theta=75°} \\ if\ \theta = 120° & y_{p1} \end{cases} \tag{4.10}$$

Using these coordinates, a final pulley shape was created. Figure 4.10 provides a graphical view of the coordinates and a sketch of the final pulley shape.

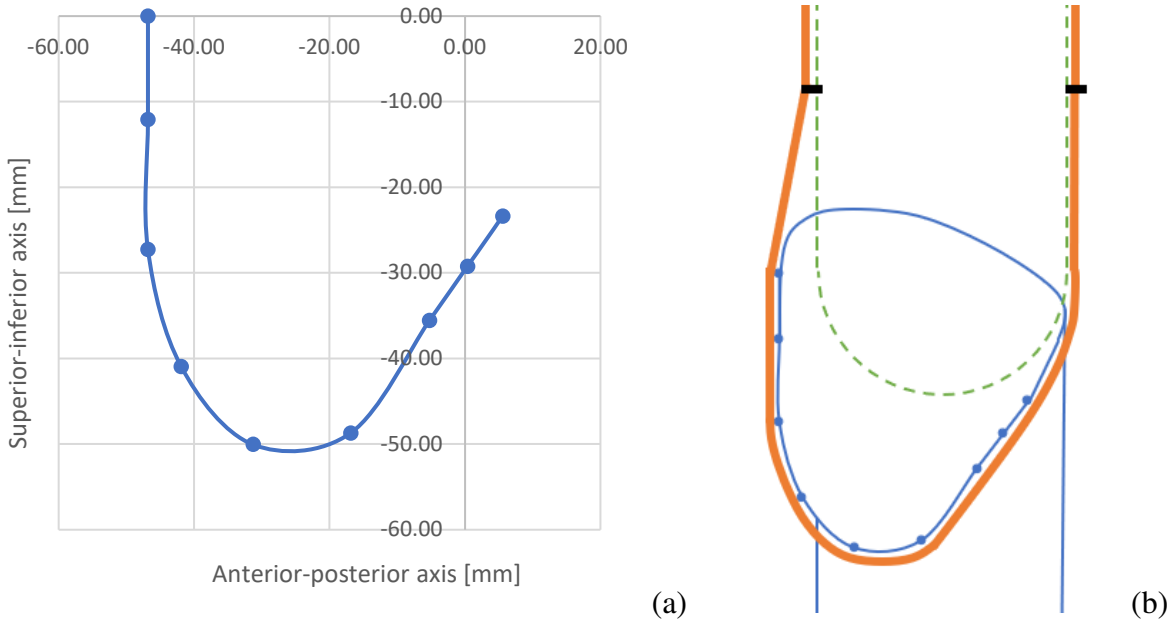

Figure 4.10. (a) Coordinates of the final pulley shape. (b) Sketch of the joint with the final pulley shape.

Since this final pulley shape is generated using moment arm data at 100% of the maximum magnitude, alternate pulleys were simulated at 75%, 50% and 25%.

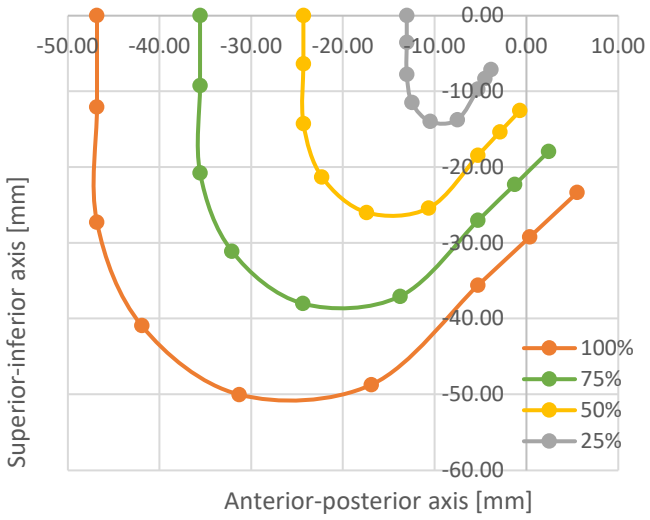

Figure 4.11. Alternate pulley shapes for the joint with no offset. Moment arm magnitudes shown are 100% (orange), 75% (green), 50% (yellow), and 25% (grey).

To select a pulley shape to be implemented, the theoretical moment arms were simulated and are shown in Figure 4.12.

Due to the physical design of the joint, specific alterations were made to ensure contact between the cable and pulley at all degrees of flexion. Because of these changes, the theoretical moment arms are not identical to the biological values. A comparison is shown in Figure 4.12.

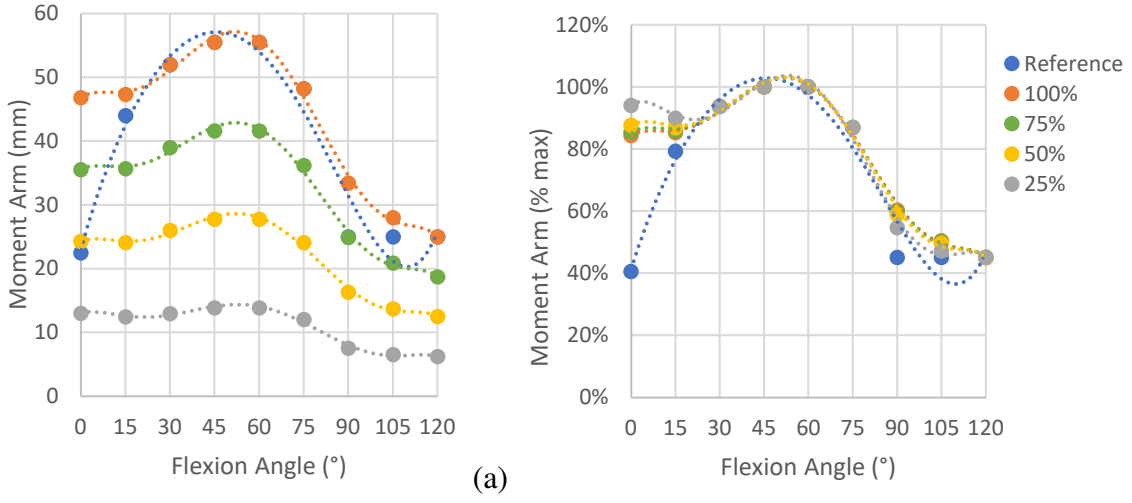

Figure 4.12. Moment arm comparison between male reference data for the biological knee and final pulley shapes with varying magnitudes. (a) Moment arm in mm. (b) Moment arm as a percentage of maximum moment arm.

Observing Figure 4.12 (a), it is clear that the alternate pulley shapes successfully change the magnitude of the moment arm by a constant factor throughout the entire ROM without

changing the shape of the curve. When evaluating Figure 4.12 (b), it is easier to compare the joint moment arms to the male biological reference data. The theoretical moment arm provided by the pulley shape is increased significantly at 0°, and minor increases in the moment arm occur at 15°, 90°, and 105°. The rest of the points are identical to the reference data, as they were not altered to ensure contact between the cable and the pulley.

In order to validate the theoretical results, the moment arms must be tested experimentally. Based on the simulations, the pulley shape at 100% moment arm was selected for experimental evaluation. This design was chosen because the moment arm at 0° had the most negligible discrepancy with the biological joint out of all the other designs. This can be seen in Figure 4.12 (b). Though this joint was the least accurate from 90° to 120°, the behaviour at 0° was deemed more important since the data points after 90° on the biological curve are based on an assumption. Testing is later conducted, and results are presented in section 6.2.

4.1.2 Joint with Offset

There are instances where one may not be able to align the mechanical knee joint with the biological joint (e.g. size restrictions, actuator placement, mechanical constraints). For this reason, a modular design was developed. Given a prescribed offset distance, a joint that remains compatible with the ICR of the biological knee can be created.

4.1.2.1 Limit Simulations

Knowing that the goal of this joint is to re-create the same kinematics as the joint with offset regardless of the joint placement, it is important to consider the offset limitations. For example, a joint cannot feasibly be located 1 meter away from the biological knee due to physical constraints and inconveniences that would lead to user rejection. For this design, limits have been put in place that restrict the placement of paths and pins to a 150 mm radius from the origin. This limit was determined experientially. It is also important to clarify that the joints cannot overlap the path of the biological ICR. If the device crosses the ICR of the biological knee, the device is no longer considered “offset,” and the initial design for a joint with no offset should be implemented. Therefore, to avoid overlap with the ICR, the paths have been restricted and cannot have x coordinates $-7 < x < 0$ at any degree of flexion. By trial-and-error process, four limiting pin coordinates were located and are shown in Table II.

Table II. Limiting pin coordinates for the offset joint.

Restriction	**x-coordinate**	**y-coordinate**
Maximum x-coordinate	124	80
Maximum y-coordinate	30	150
Minimum x-coordinate	-127	-75
Minimum y-coordinate	-8	-144

These pins represent the starting point for each curve drawn in Figure 4.13.

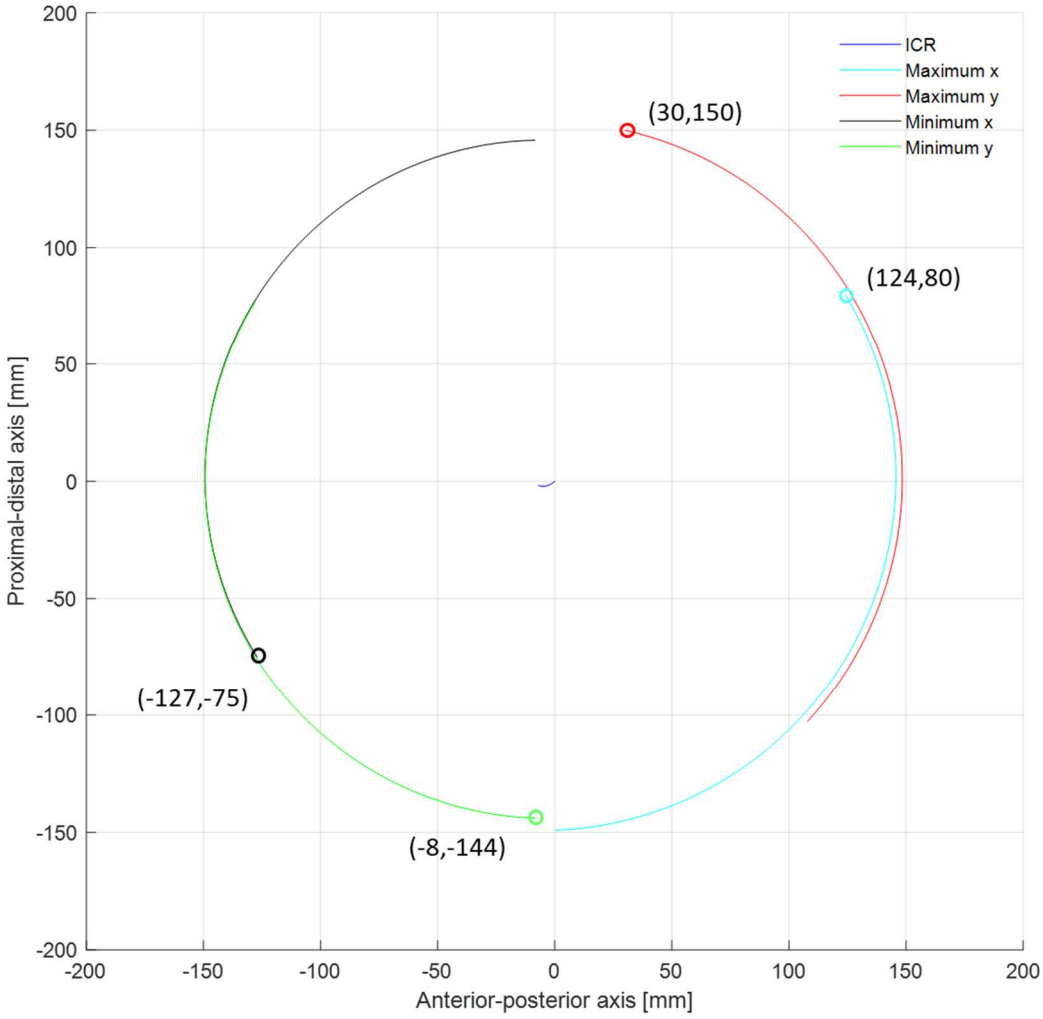

Figure 4.13. Evaluation of offset joint limits. Location of pins at 0° flexion indicated by small circles.

As highlighted by the simulation, if the joint must be located anteriorly or posteriorly to the biological knee, the maximum or minimum coordinates must be considered, respectively. One cannot use a design where pins are both on the anterior and posterior sides of the origin because

this would mean that the width of the device would span the ICR and reduce the design to a joint without offset.

When modularizing the joint to suit the needs of an application, it is crucial to keep the starting pin locations within the identified limits, ensure the paths do not cross the ICR and select three paths that do not intersect. If the paths intersect, the pin-in-slot mechanism will not function as desired.

4.1.2.2 Kinematics/Paths

Modelling will be carried out for a test case where the device is offset such that the centerline of the device is located at an arbitrary location of 40 mm anterior to the ICR at 0° flexion.

As with the model with no offset, three pins and their corresponding paths must be identified to allow appropriate motion from 0° to 120° flexion. By trial-and-error process, three paths that do not intersect or cross the ICR were found and are modelled using the following equations.

$$x_{iM} = x_1 + \left(\sqrt{x_{i\,Diff\,M}^2 + y_{i\,Diff\,M}^2}\right) * cos\left(\left|tan^{-1}\left(\frac{y_{i\,Diff\,M}}{x_{i\,Diff\,M}}\right)\right| - \theta\right) \quad (4.11)$$

$$y_{iM} = y_1 + \left(\sqrt{x_{i\,Diff\,M}^2 + y_{i\,Diff\,M}^2}\right) * sin\left(\left|tan^{-1}\left(\frac{y_{i\,Diff\,M}}{x_{i\,Diff\,M}}\right)\right| - \theta\right) \quad (4.12)$$

Where (x_{iM}, y_{iM}) are parametric equations describing paths for pins $i = 1, 2, 3$ and $(x_{i\,Diff\,M}, y_{i\,Diff\,M})$ are the locations of pins $i = 1, 2, 3$ at 0° flexion.

The following equations provide the locations for pins 1, 2, and 3 in Figure 4.14.

$$(x_{Diff\,1\,M}, y_{Diff\,1\,M}) = (50,60) \quad (4.13)$$

$$(x_{Diff\,2\,M}, y_{Diff\,2\,M}) = (55,65) \quad (4.14)$$

$$(x_{Diff\,3\,M}, y_{Diff\,3\,M}) = (60,70) \quad (4.15)$$

Points indicate these pins in the figure. The ICR is shown but does not represent a path.

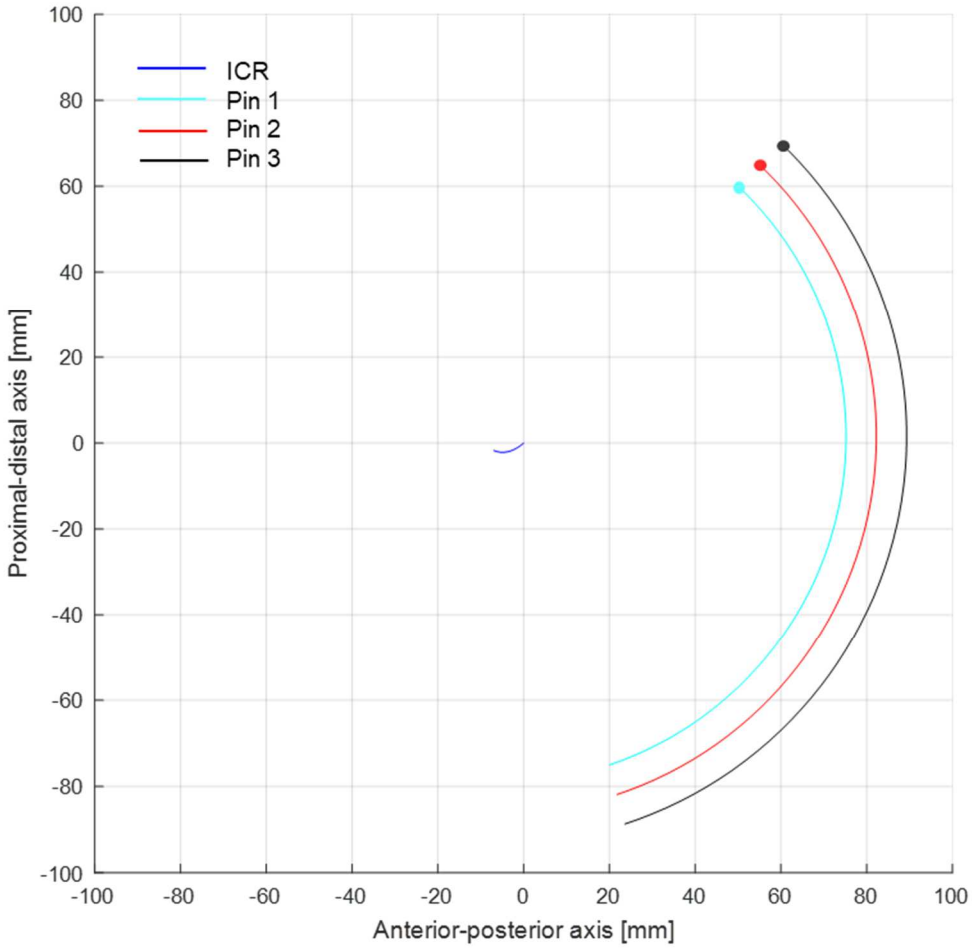

Figure 4.14. First iteration of the design concept with offset.

This design iteration showed that pins 1 and 3 have the freedom to rotate about pin 2, adding approximately 40° of rotational freedom. As this was undesired, a second iteration of paths was generated. Refer to Appendix A.1 for additional information on this design.

The following two equations replace (4.14) and (4.15). The location of pin 1 was left the same.

$$(x_{Diff\,2\,M}, y_{Diff\,2\,M}) = (20,65) \tag{4.16}$$

$$(x_{Diff\,3\,M}, y_{Diff\,3\,M}) = (30,85) \tag{4.17}$$

The following path simulation was created in MATLAB using the revised pin locations.

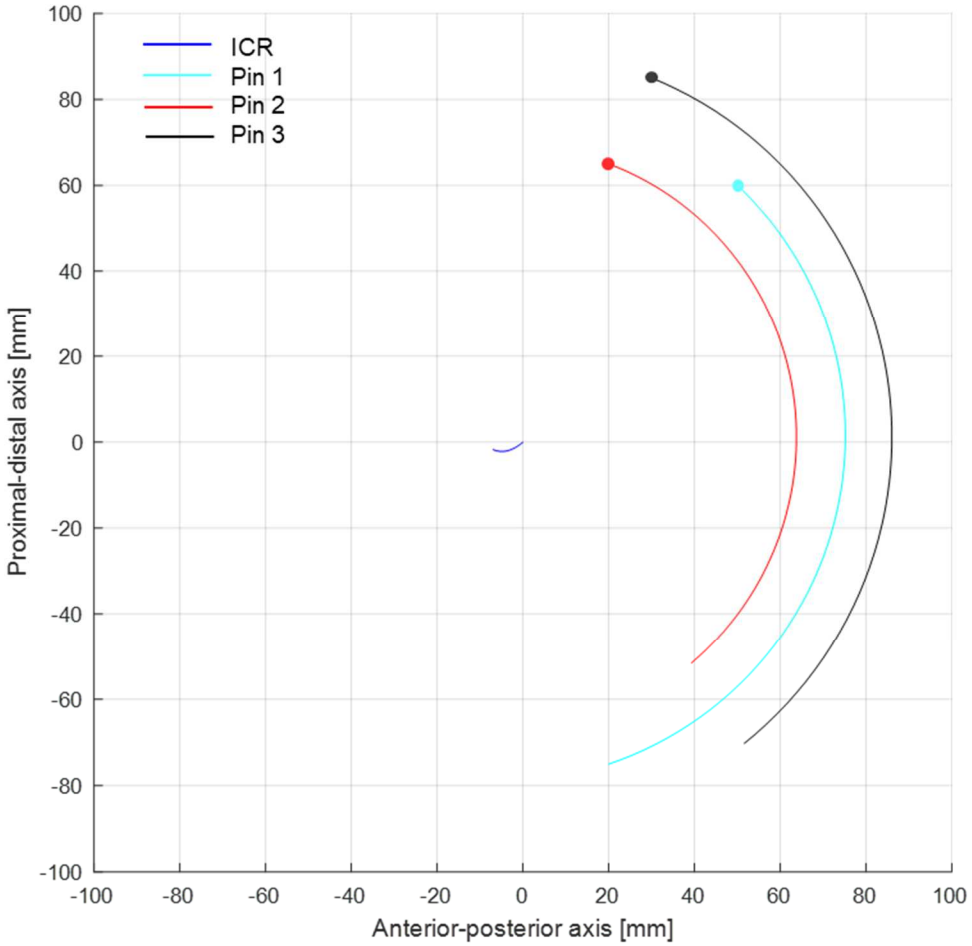

Figure 4.15. Final design concept with offset.

The new path locations do not allow for the undesired DOF identified in the first design iteration; thus, these are implemented in the final design. Once again, to model the locations of the pins throughout flexion, eight lines connecting the pins were drawn at 15° intervals. Figure 4.16 shows the location of the pins at different degrees of flexion, which are to be validated experimentally.

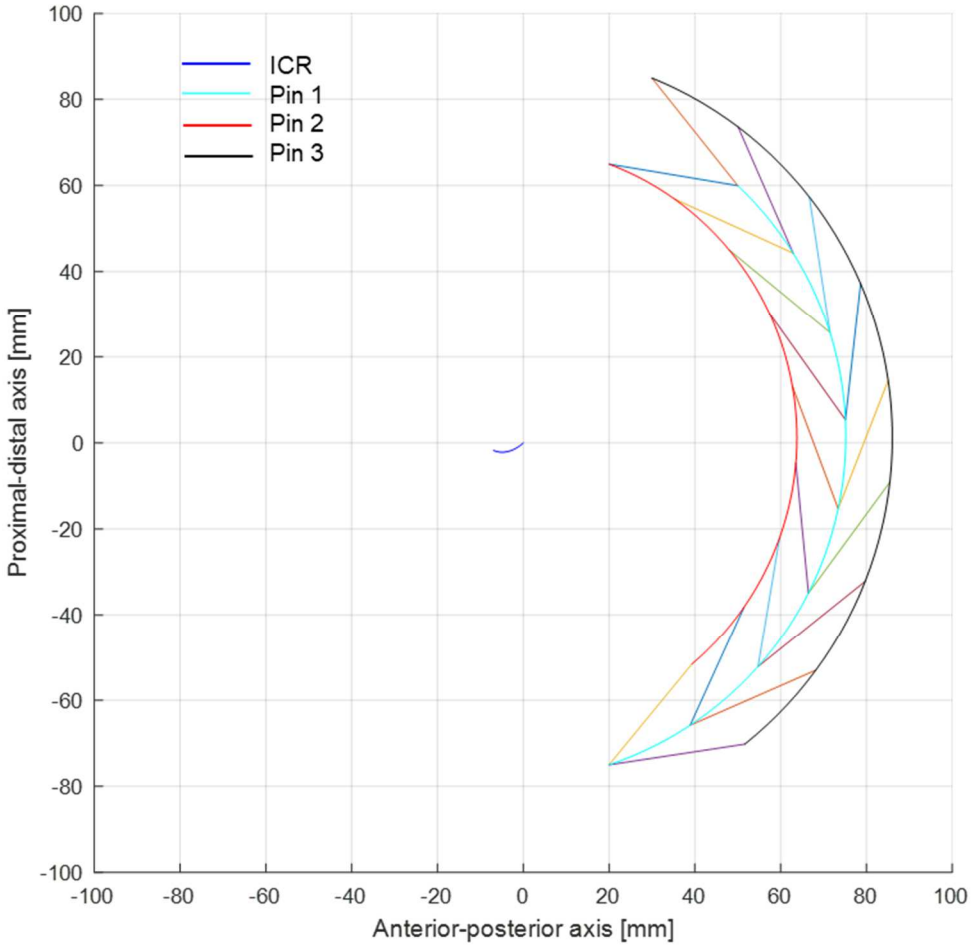

Figure 4.16. Final design concept with offset. Multicolored lines connecting pin 1 to pin 2 and pin 3 are drawn at 15° intervals between 0° and 120°.

As done previously, a 3-dimensional model of the joint with offset was created in SolidWorks. Figure 4.17 provides a lateral side view of the joint at the ends of its ROM, 0° and 120° flexion. Pins are identified in the same colours as shown in Figure 4.15. The ICR of the device is a theoretical point in space modelled based on the reference frame of the device components. The ICR curve is drawn in correspondence to the femoral component as it is fixed in space, and the point in blue is drawn with respect to the tibial component.

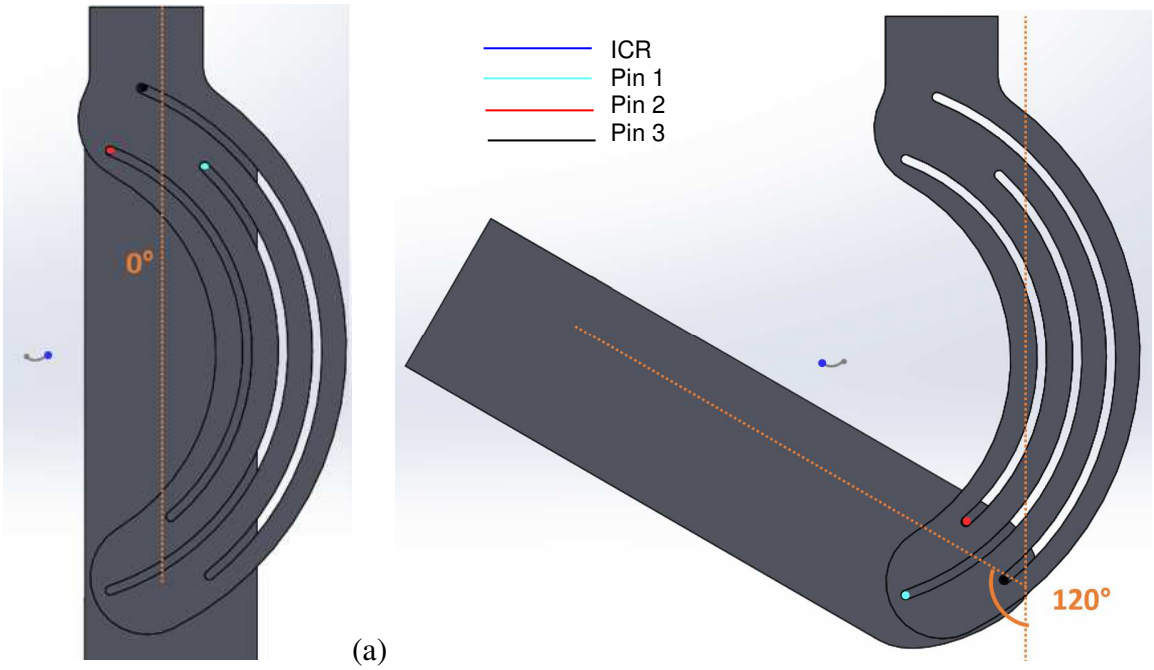

Figure 4.17. SolidWorks model of the joint with offset at ends of the ROM. (a) 0° flexion, (b) 120° flexion.

This modelling confirms that the offset joint maintains an ICR that coincides with the biological knee and that the joint cannot surpass its designed ROM due to the pin locations.

4.1.2.3 Moment Arm

As it was done for the joint with no offset, the moment arm was modelled for the offset modular design test case. Due to the nature of the shape of the design, the pulley had to be located further distally from the joint center to allow proper force transmission and flexion of the joint. Essentially, this means that the surface of the pulley on the tibial component had to be located distally to the ends of the paths of the femoral component.

The pulley shape designed for the joint without offset in section 4.1.1.2 is also used in this case; the coordinates simply had to be translated. The coordinates for the final offset pulley shape were translated from their original position anteriorly so that the x coordinate at 0° was flush with the posterior side of the tibial component. Since the tibial component has a centerline at 40 mm and a width of 54 mm, the posterior edge is located at x = 13 mm. The pulley was also translated distally by 50 mm to ensure its lowest point was distal to the end of pin path 1 (cyan in Figure 4.15). The following equations provide the coordinates for the offset pulley shape.

$$x_{pM} = x_{p2} - x_{p2\,@\,0^\circ} + 13 \tag{4.18}$$

$$y_{pM} = y_{p2} - 50 \tag{4.19}$$

Figure 4.18 shows the resulting shape of the pulley for the joint with offset.

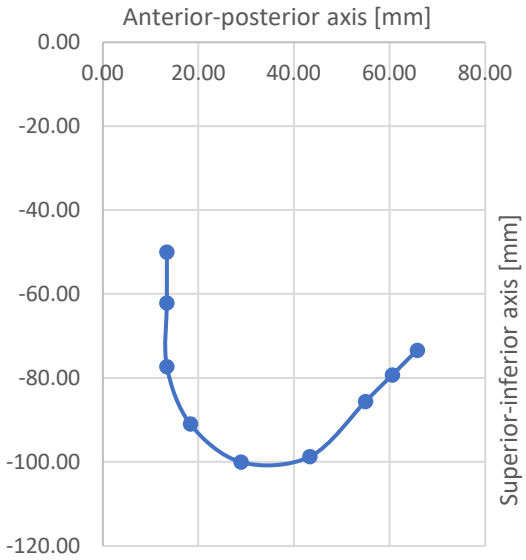

Figure 4.18. Coordinates of the offset joint pulley shape.

The moment arm of this joint, M_M, is measured from the ICR to the last point of contact between the pulley and cable. M_M is represented by (4.20). The moment arm of the offset joint is compared to reference data in Figure 4.19.

$$M_M = \sqrt{(x_{pM} - x_1)^2 + (y_{pM} - y_1)^2} \tag{4.20}$$

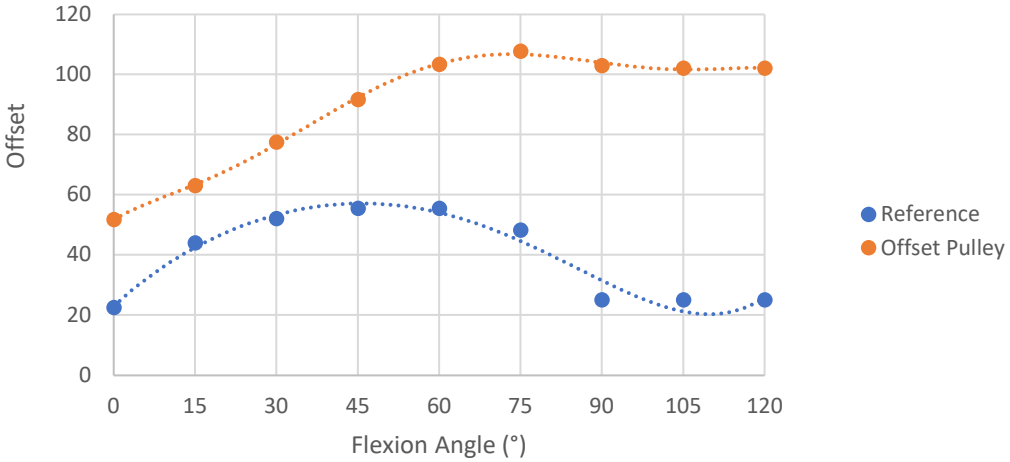

Figure 4.19. Moment arm comparison between male reference data for the biological knee and the offset pulley shape.

Due to the offset and translation of the pulley, the moment arm is consistently larger than the reference data. The magnitude is not of concern as this can be adjusted through the actuator. Moment arm data were normalized as a percentage of their maximum value to compare the shape of the curves without consideration for the magnitude. The following figure presents these results.

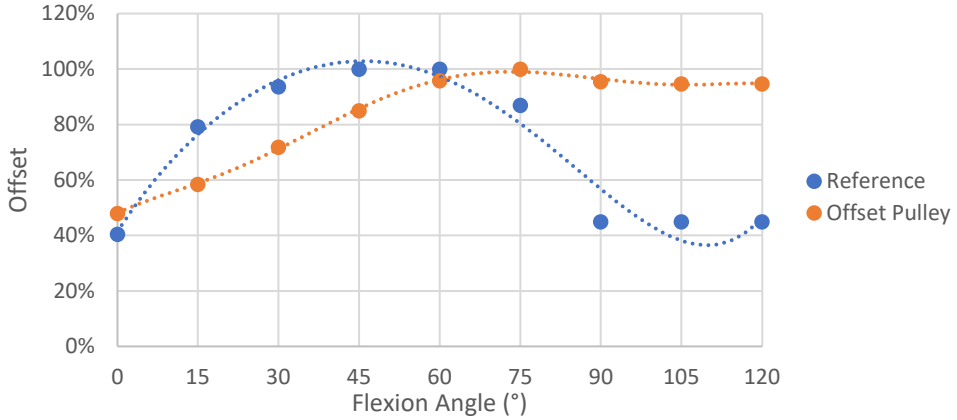

Figure 4.20. Moment arm comparison between male reference data for the biological knee and the offset pulley shape. Normalized as a percentage of the maximum moment arm.

Unlike the reference curve, the offset pulley creates a maximum moment arm at 75°. Due to physical constraints discussed in section 4.1.1.2, the moment arm cannot decrease in the same fashion as the biological knee and return to approximately its original value at 90°.

Chapter 5. Prototype Fabrication and Experimental Testing

Once a joint design was conceptualized and modelled, it was essential to verify that it satisfies the design criteria established in section 3.4. The purpose of experimental testing was to validate that the joint can transfer force, has a moment arm that varies throughout movement, accommodates an offset while maintaining kinematic compatibility, has the appropriate ROM of 0° to 120° flexion, and prevents hyperextension.

5.1 Prototypes and Fabrication Process

Experimental prototypes were created using the Ultimaker 3 Extended 3D Printer. SolidWorks models were printed in black PLA at a 0.2 mm profile and with 10% infill. The femoral components were printed in two parts for assembly, and the tibial components were printed in a single piece. To allow an analysis of the last point of contact between the cable and the pulley on the tibial component, the lateral side was omitted during 3D printing. Figure 5.1 shows how this provides a clear view of the pulley from the lateral view.

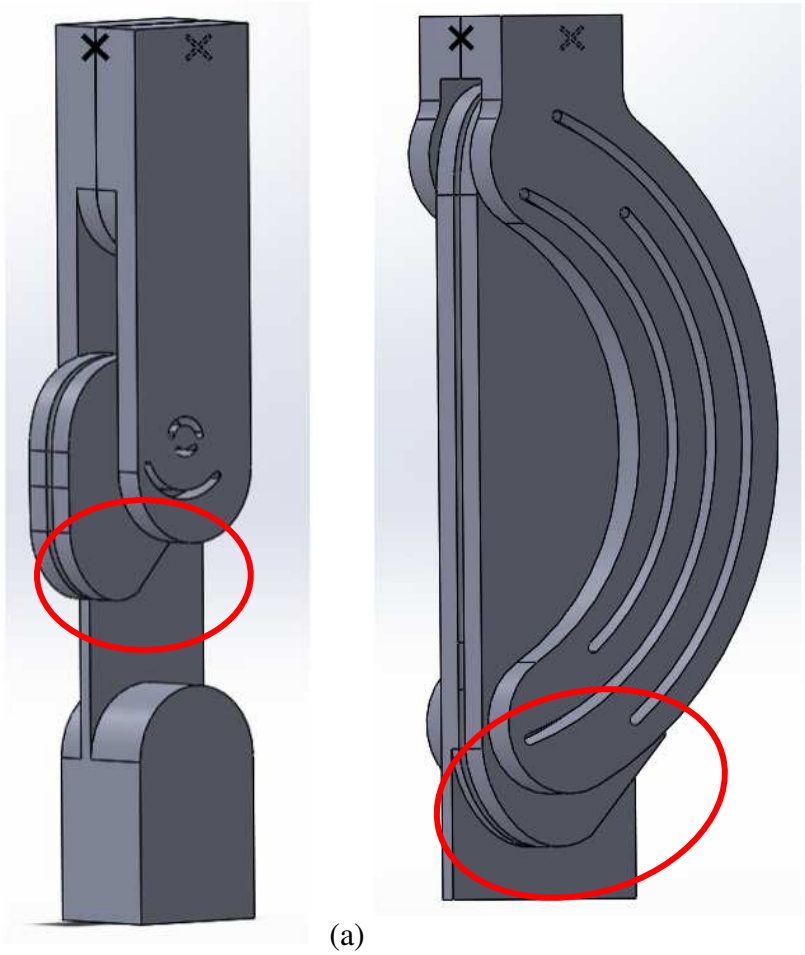

Figure 5.1. SolidWorks assemblies with lateral sides omitted for clarity. (a) Joint without offset. (b) Joint with offset. Portions of the pulleys exposed by removing the lateral sides are circled in red.

Steel pins were inserted into both prototypes' tibial components and affixed with cyanoacrylate (CA). Bushings were not deemed necessary for the preliminary mechanical prototypes and were therefore excluded from the fabrication process.

Twisted polypropylene mason twine with a diameter of 2 mm was selected as the cable material due to its minimal strain and low cost. A bright orange coloured cable was a clear choice for high visibility against the black PLA material. The cable is fixed to the tibial component with aluminum wire and CA adhesive.

In order to simplify the fabrication process, the pretensioner pulleys were replaced with screw-in eyelets so that the cable can nevertheless be guided along the appropriate path. Eyelets were fixed to the femoral component with CA to guide the cable. The following figures show the experimental prototypes.

Figure 5.2. Experimental prototype of the joint with no offset. The femoral and tibial components are constructed out of PLA with steel pins. The cable (bright orange) is made of polypropylene mason twine and is fed through eyelets on the anterior and posterior ends of the femoral component.

Figure 5.3. Experimental prototype of the joint with offset. An extension with a slot is added to the tibial component to allow for use with the testing rig.

As visible in Figure 5.3, an extension with a slot is added to the tibial component of the offset joint. This addition was fixed with CA and is designed to accommodate the significant proximal-distal translation of the joint during testing.

5.2 Experimental Setup and Methodology

To validate that the designed joints satisfy the design criteria, two testing rigs were developed. The first experimental setup can be seen in Figure 5.4.

Figure 5.4. Testing rig 1. Prototypes are fixed to a board with two curved tracks by adjustable U-shaped supports. A tripod is fixed to the board to take photos of the prototypes at prescribed intervals of 15°.

The first testing rig is designed to take photos of each joint prototype at 15° intervals from 0° to 120° flexion. This permits the evaluation of their kinematics and moment arm performance.

A 1.9 cm-thick plywood platform is supported by three beams that span the length of the platform and with square cross-sections of 5.1 x 5.1 cm. This platform has two curved tracks that are designed to allow joint flexion from 0° to 120°. Four L-brackets were bolted together in pairs to create two U-shaped supports at the proximal and distal ends of the joints. These supports are fixed to the platform by tightening nuts and bolts through the curved tracks. The proximal and distal ends of the joint prototype are bolted to the U-shaped supports.

To ensure that photos are taken from the same reference point, a tripod is fixed to the platform. A small support piece was 3D-printed using PLA filament to fix the center of the tripod to the platform with screws. This prevents significant discrepancies between photograph reference frames. To further ensure minimal movement between trials, a wireless remote is used to initiate photo capture at a distance. Photos are taken with iPhone XR.

The following figure shows both joints fixed to the testing rig at 45° flexion.

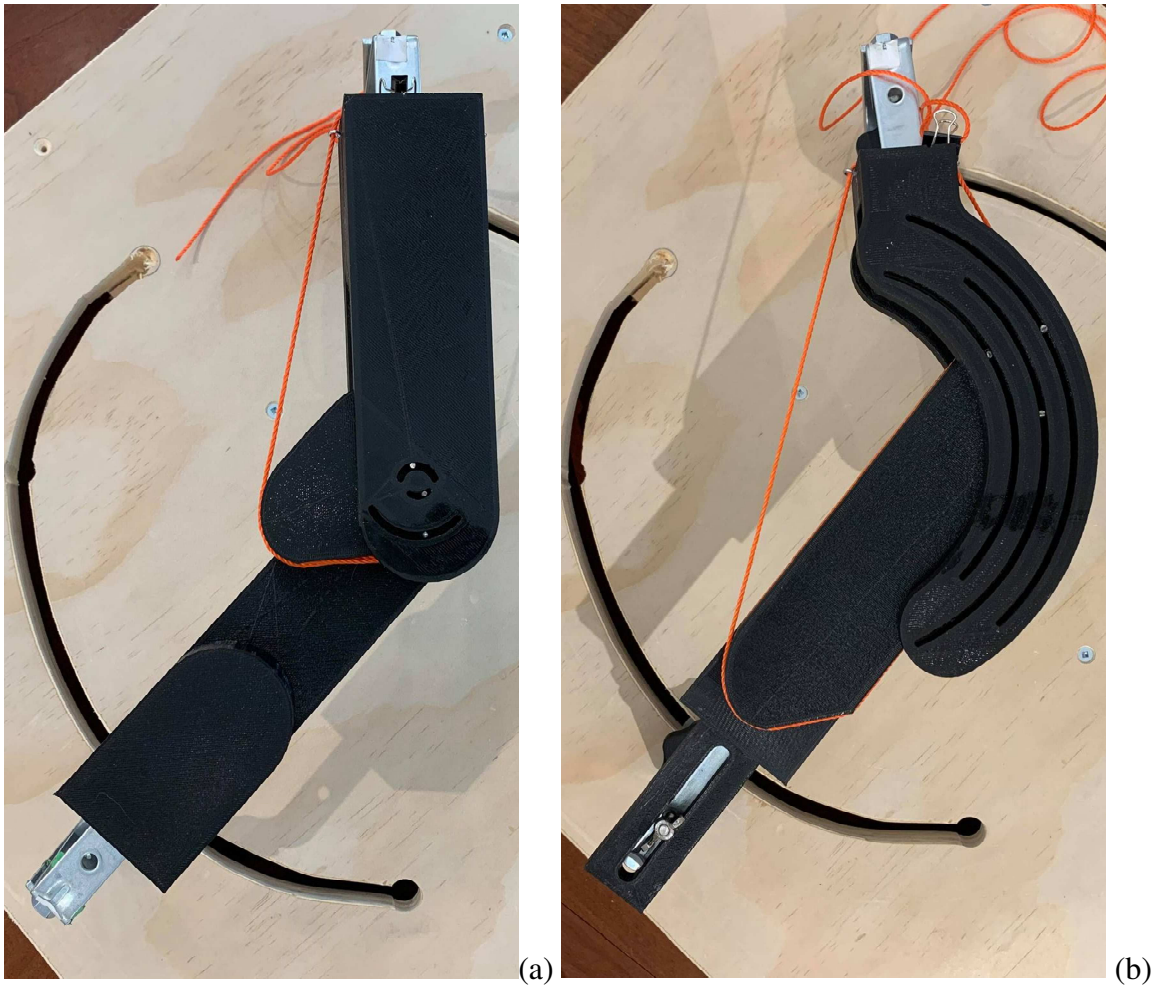

(a) (b)

Figure 5.5. Photos of joints at 45° flexion - taken using testing rig 1. (a) Joint with no offset. (b) Offset joint.

To ensure comparable images, the femoral component of the joint is fixed at the end of its track and does not move throughout testing. A plastic 12-inch goniometer is applied to measure the flexion angle before each trial and is removed before photos are taken. The support beams beneath the platform allow for manual adjustment of the tightening nuts, permitting joint movement between trials. The cable is manually pulled taut and fastened with a binder clip at every 15° interval. The resulting images are consequently analyzed in MATLAB. This is discussed in further detail in Chapter 6.

A second experimental setup was developed to further validate that the joints each possess a single kinematic solution. It can be seen in Figure 5.6.

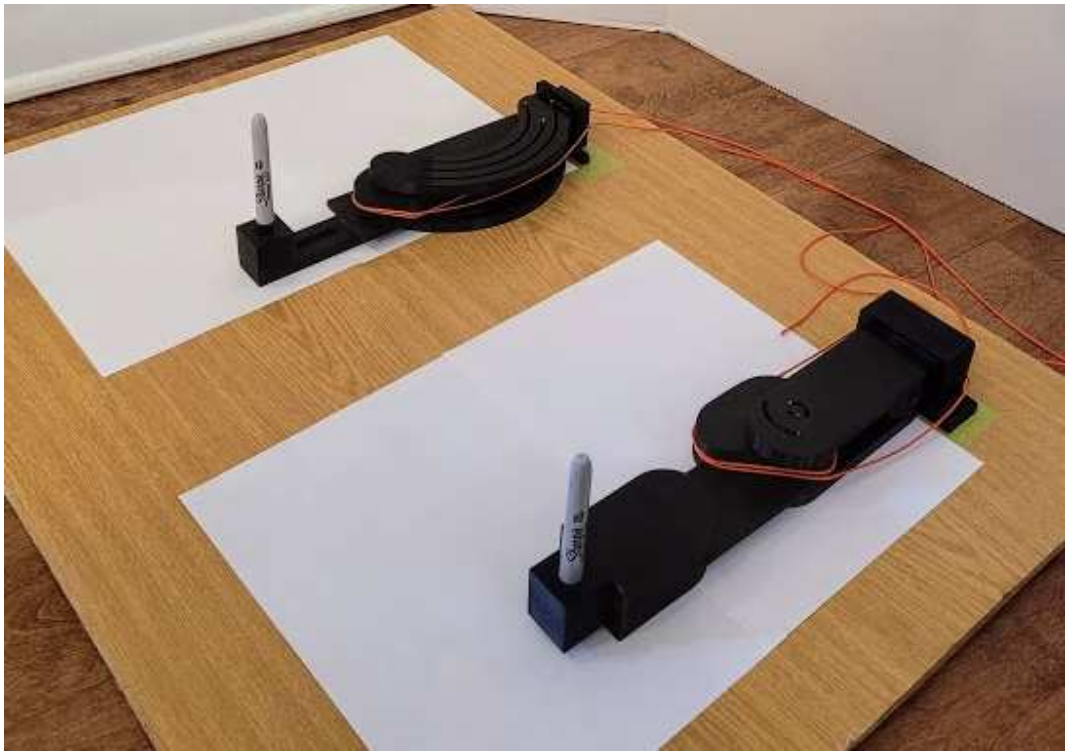

Figure 5.6. Testing rig 2. The femoral components of each prototype are fixed to a board. Markers are affixed to the distal ends of the tibial components. When tension is applied to the cables, curves are drawn.

The femoral components of both joints are fixed to a plywood board. U-shaped brackets were custom 3D-printed to fit the components and allow for easier adhesion to the board. Small blocks designed to hold a permanent marker were also 3D-printed and fixed to the tibial components of the joints with CA. White sheets of paper are taped to the board to provide a clean surface for drawing rotation paths. A marker is placed inside the holder and provides a fixed point on the tibial component for tracking. Tension is applied to the posterior and anterior cables to flex and extend the joint, respectively. As the joint moves, the marker draws a curve on the white sheets of paper placed beneath it. Ten cycles of flexion and extension from 0° to 120° are conducted for each joint. The resulting curves are analyzed in Chapter 6.

Chapter 6. Analysis, Results and Discussion

Chapter 6 analyzes and discusses the experimental results from testing described in Chapter 5. This section is divided into three components: kinematic analysis, moment arm analysis, and DOF analysis.

6.1 Kinematic Analysis

In order to begin the kinematic analysis, .jpg images were imported into MATLAB using the "imread" function. Nine images were taken of each joint at 15° intervals from 0° to 120° flexion. Though movement was minimized between photos by the design of the testing rig, the reference frames of all images were not identical. Therefore, reference frames were normalized to that of the joints at 0° flexion. Images were displayed in MATLAB using the "imshow" function. Using the data cursor in the MATLAB interface, the coordinates of the top left and top right corners of the femoral component were manually identified and recorded in an Excel spreadsheet. It is important to note that MATLAB identifies the top left corner of its images as the origin. Y-values are positive downwards, and x-values are positive to the right.

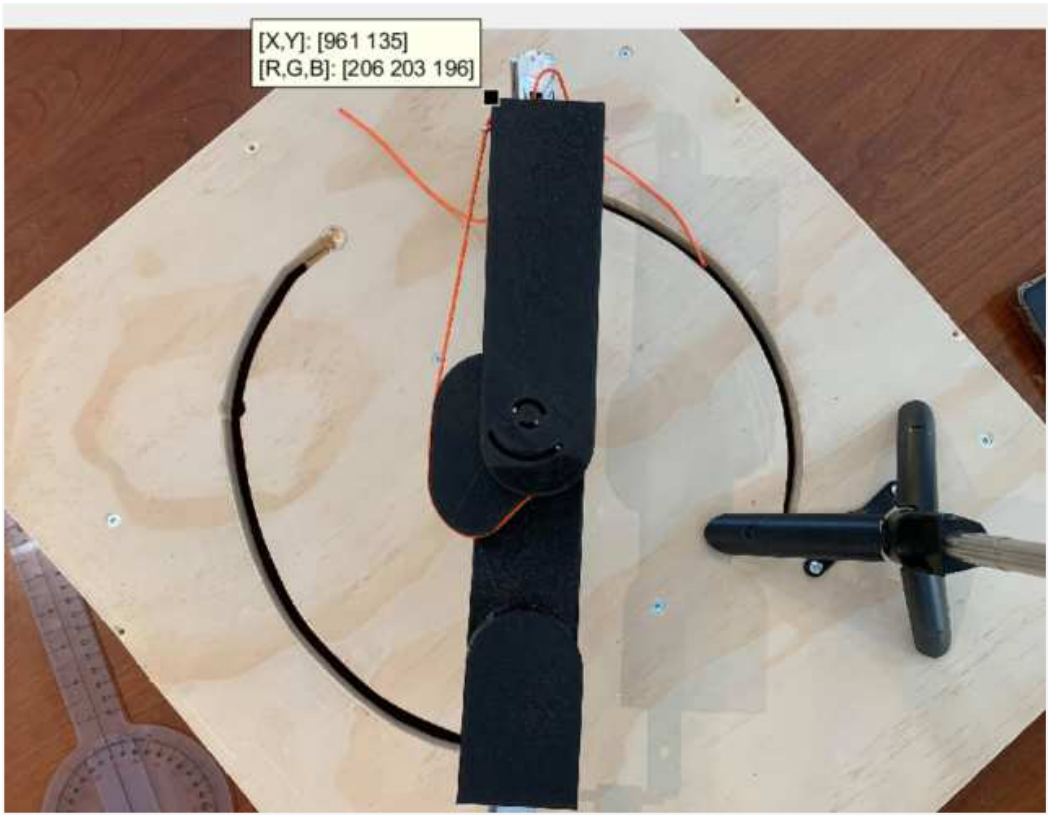

Figure 6.1. Data cursor function in MATLAB interface identifying coordinates of the top left corner of the joint with no offset at 0° flexion.

Figure 6.1 shows the MATLAB interface with the top left corner selected by the data cursor. The coordinates of the points are provided in pixels, which are consequently converted to mm.

To ensure that the same reference frame is used between photos, three critical factors must be identical: rotation, origin, and scale. To align the rotation of reference frames between images, the MATLAB function “imrotate” is used to rotate images so that the top of the femoral component is horizontal. The required rotation is calculated as follows.

$$\theta_{rotate} = \tan\left(\frac{y_{TL} - y_{TR}}{x_{TL} - x_{TR}}\right) \tag{6.1}$$

Where (x_{TL}, y_{TL}) and (x_{TR}, y_{TR}) are the coordinates of the top left and top right corners, respectively. The image is then rotated by the appropriate degree and displayed in MATLAB again. The data cursor is used to ensure that the new top left and right corners have the same y-value.

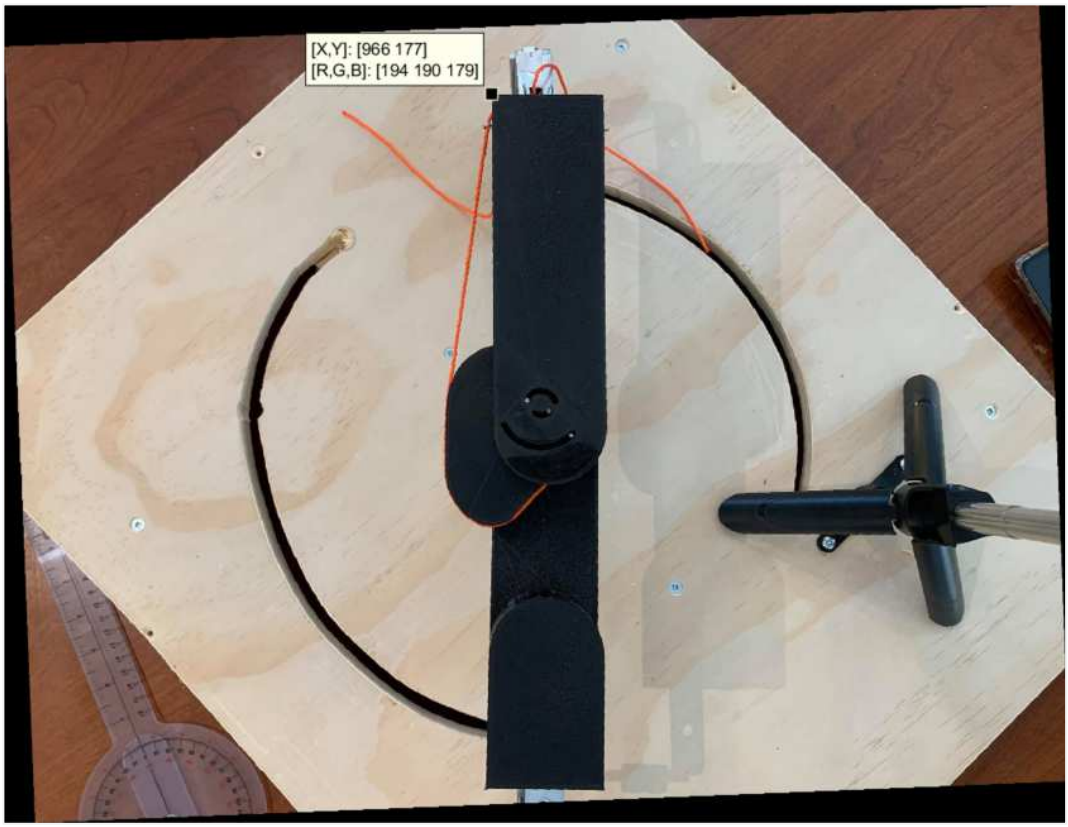

Figure 6.2. Rotated image of joint with no offset at 0° flexion. New top left corner is identified using data cursor.

Next, an origin is determined. Based on the simulations, the location of the origin is the point at the beginning (right-hand side) of path 1. Figure 6.3 provides an example of the manual identification of this point.

Figure 6.3. Manual identification of the origin using data cursor in MATLAB.

In order to finalize reference frame alignment, the scale must be verified. Since the width of the femoral component and the coordinates of the new top left and top right corners are known, a ratio of pixels to millimeters, *S*, can be created.

$$S\left[\frac{pixels}{mm}\right] = \frac{\sqrt{(x_{TLnew} - x_{TRnew})^2 + (y_{TLnew} - y_{TRnew})^2}\,[pixels]}{w_f\,[mm]} \qquad (6.2)$$

Where (x_{TLnew}, y_{TLnew}) and (x_{TRnew}, y_{TRnew}) are the coordinates of the top left and top right corners after rotation, respectively, and w_f is the width of the femoral component in mm. The scale of the images is adjusted after further data points are extracted from the images. Though it would have been possible to determine the scale based on the length of the femoral component, the width was deemed to be more reliable. The distal end of the femoral component is rounded; therefore, manually identifying the center of this curve could have introduced additional error.

The purpose of the kinematic analysis is to track the locations of pins 1, 2, and 3 throughout flexion and verify how closely they follow the simulation. Thus, the data cursor was used to manually select what appeared to be the most central pixel for each of the three pins.

Figure 6.4. Manual identification of the center of a pin using data cursor in MATLAB.

The locations of the pins are denoted by $(x_{i\ pin}, y_{i\ pin})$, where i = 1, 2, 3 (the pin number). These coordinates can finally be translated to the correct reference frame using the following equations.

$$x_{i\ pin\ new} = \left(x_{i\ pin} - x_0 + x_{0\ @\ 0^\circ} - x_{i\ pin\ @\ 0^\circ}\right)S \tag{6.3}$$

$$y_{i\ pin\ new} = [(-1)(y_{i\ pin} - y_0 + y_{0\ @\ 0^\circ}) - y_{i\ pin\ @\ 0^\circ}]S \tag{6.4}$$

Equations (6.3) and (6.4) translate all frames of reference so that (x_0, y_0) is located at (0,0), and the scale factor S both normalizes the size of the images and converts units from pixels to mm. Multiplying the y-coordinates by a factor of -1 allows the y-axis to be positive upwards (proximally), thus aligning with the simulations.

Pin locations were plotted against the paths, and the following results were obtained.

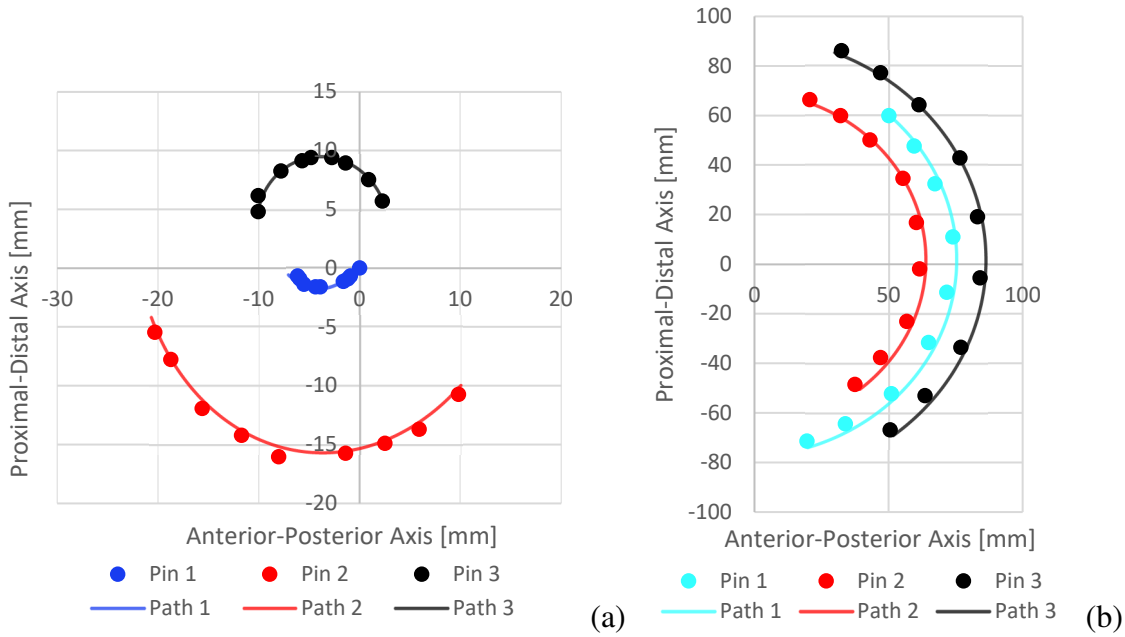

Figure 6.5. Kinematic experimental results. Locations of pins are represented by points overlaid on simulation paths. (a) Joint with no offset. (b) Joint with offset.

In Figure 6.5, theoretical paths are shown by a solid line, and the location of the pin centers are shown in corresponding colours. Evidently, the pins on both joints appear to follow their simulated paths with a degree of error. To quantify the agreement between kinematic simulations and experimental results, percent error and absolute error were evaluated. Percent error and absolute error were calculated as follows:

$$\% \text{ error} = \frac{\left|d_{theoretical} - d_{experimental}\right|}{d_{theoretical}} * 100 \tag{6.5}$$

$$\text{absolute error} = \left|d_{theoretical} - d_{experimental}\right| \tag{6.6}$$

where $d_{theoretical}$ and $d_{experimental}$ are the distances between the theoretical and experimental pin centers and the origin in mm, respectively.

Error values were evaluated for each data point, meaning that both percent error and absolute error values were determined at every 15° for each pin. Figures 6.6,Figure *6.8*, Figure *6.7*, and Figure *6.9* present these results.

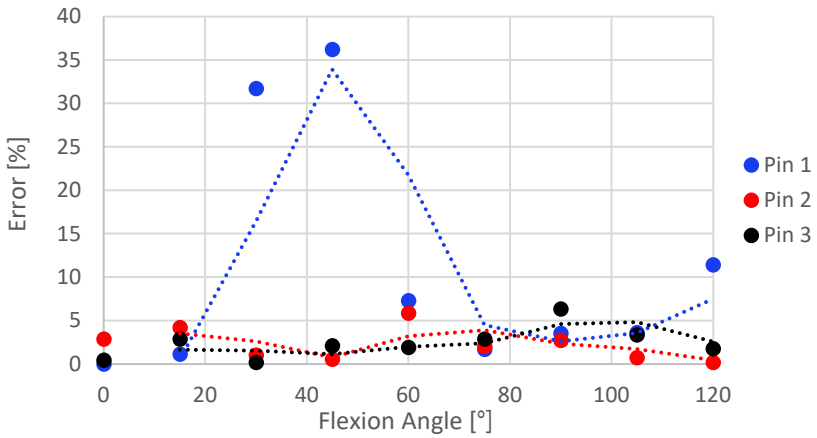

Figure 6.6. Kinematic experimental percent error for the joint with no offset. Average errors throughout flexion: pin 1=10.72%, pin 2=2.22%, pin 3=2.42%.

An average percent error value was obtained for each pin. In the joint with no offset, Pin 1 had the most significant error with 10.72%. Pin 2 had 2.22% error, and pin 3 had 2.42% error. The overall kinematic percent error for the joint with no offset was 5.12%.

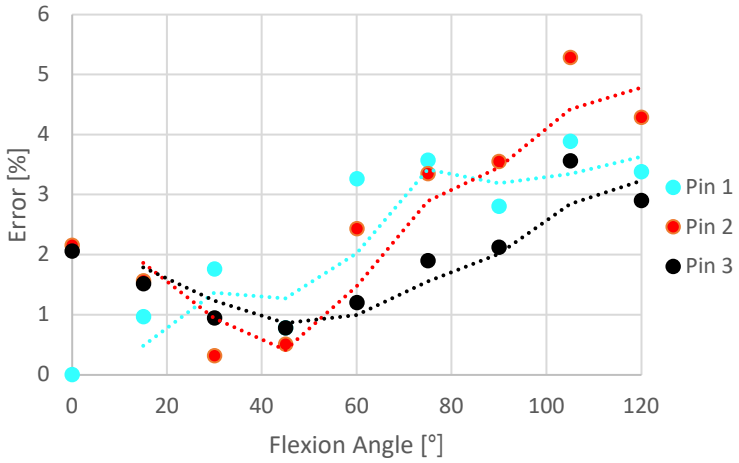

Figure 6.7. Kinematic experimental percent error for the joint with offset. Average errors throughout flexion: pin 1=2.27%, pin 2=2.61%, pin 3=1.89%.

Average error values for pin location throughout flexion in the joint with offset are as follows: pin 1 = 2.27%, pin 2 = 2.61%, and pin 3 = 1.89%. The overall kinematic error for the joint with offset was 2.26%. Unfortunately, it was not possible to physically obtain error values for the ICR of this joint as it is a theoretical point in space.

Pin 1 in the joint with no offset demonstrated significant error at 30° and 45° flexion, which can likely be attributed to the construction of the prototypes. Since the pins could not be 3D-printed in one piece with the tibial component, metal pins had to be inserted and fixed by hand.

This introduced error because when the pins are not perfectly perpendicular to the component's surface, the pins experience friction against the inner walls of the paths. Pin 1 likely was the most affected by this, as evidenced by the error shown in Figure 6.6. The pins were also not centered on their simulated paths. Any level of clearance between the pins and their paths causes error because the pins press up against one side of the paths during movement, meaning that the pins are no longer on the centerline. Due to the fabrication of the prototypes using 3D-printed components without bushings, a slight clearance between the pins and paths was necessary. Without this clearance, the friction would be too high to allow for smooth movement during testing.

Though the difference in percent error demonstrated by both prototypes is significant, their manufacturing errors are of the same order. The decreased percent error in the joint with offset can likely be attributed to the larger distance travelled by the joint pins.

Percent error analysis showed that the joint with an offset agreed with simulations more than the joint with no offset, which motivated an error analysis in terms of absolute measurements. Since a WAE user would experience more discomfort with a considerable misalignment between their natural joint ICR and the ICR of the device, it was deemed important to investigate the total misalignment as opposed to simply evaluating the percent error. The percent error evaluation can provide meaningful information but does not adequately represent the significance of misalignment with respect to comfort and user retention. Figures Figure *6.8* and Figure *6.9* provide the absolute error results for both joint prototypes.

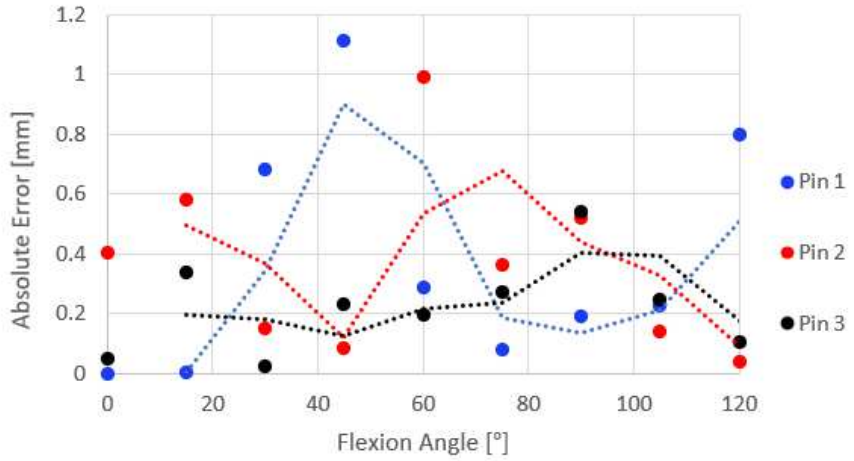

Figure 6.8. Kinematic experimental absolute error for the joint with no offset. Average errors throughout flexion: pin 1 = 0.38 mm, pin 2 = 0.36 mm, pin 3 = 0.22 mm.

On average, throughout flexion, pin 1 had 0.37 mm error, pin 2 had 0.36 mm error, and pin 3 had 0.22 mm error. The overall kinematic absolute error for the joint with no offset was 0.32 mm.

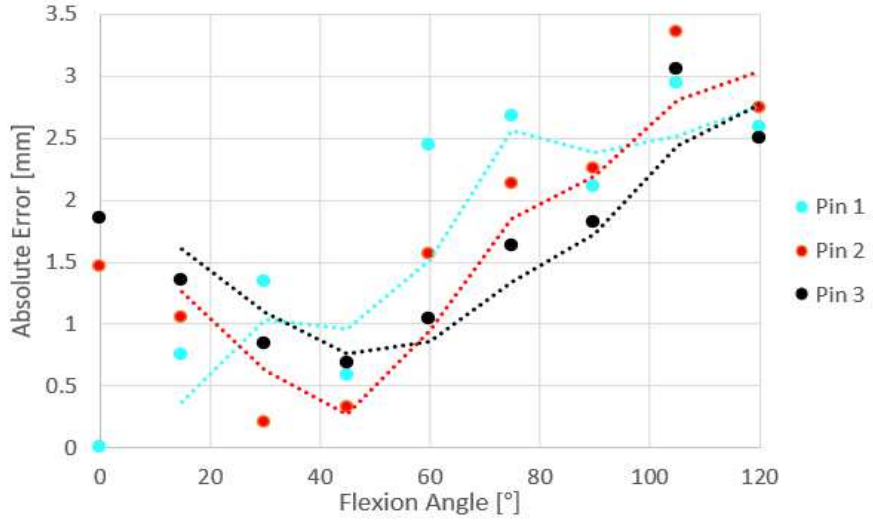

Figure 6.9. Kinematic experimental absolute error for the joint with offset. Average errors throughout flexion: pin 1 = 1.71 mm, pin 2 = 1.68 mm, pin 3 = 1.64 mm.

Since the joint with offset is larger, it experienced higher absolute errors when compared to the aligned joint. Average absolute error values for pin location throughout flexion in the joint with offset are pin 1 = 1.71 mm, pin 2 = 1.68 mm, and pin 3 = 1.64 mm. Overall, this joint had an average absolute error value of 1.68 mm.

When one compares the average absolute error between both joints, it is clear that the joint with offset would be less comfortable than the aligned joint. This being said, 1.68 mm of deviation could be considered acceptable, but the threshold for comfort has not yet been defined.

6.2 Moment Arm Analysis

An analysis was performed to examine the moment arms obtained experimentally. As with the kinematic analysis, reference frames were normalized between images. Differently, the reference frame for the moment arm analysis is based on a static tibial component compared to the static femoral component used in the kinematic analysis. A similar method is used to achieve this. The bottom corners of the tibial component are manually identified in MATLAB, and the image is rotated so that the bottom is horizontal. Since the tibial component is fixed in this reference frame, the pins are fixed as well. In the joint with no offset, the origin is selected to be the coordinates of pin 1. There is no pin aligned with the ICR for the offset joint,

so an additional translation is required. Pin 1 is located a distance of $(x_{Diff\,1\,M}, y_{Diff\,1\,M})$ away from the origin, thus pin 1 can still be used as a point of reference to locate the origin.

Image scaling is carried out in the same way as for the kinematic analysis. To obtain data for cable contact, the last visible point of contact between the pulley and the cable $(x_{contact}, y_{contact})$, is manually identified in MATLAB, as shown in Figure 6.10.

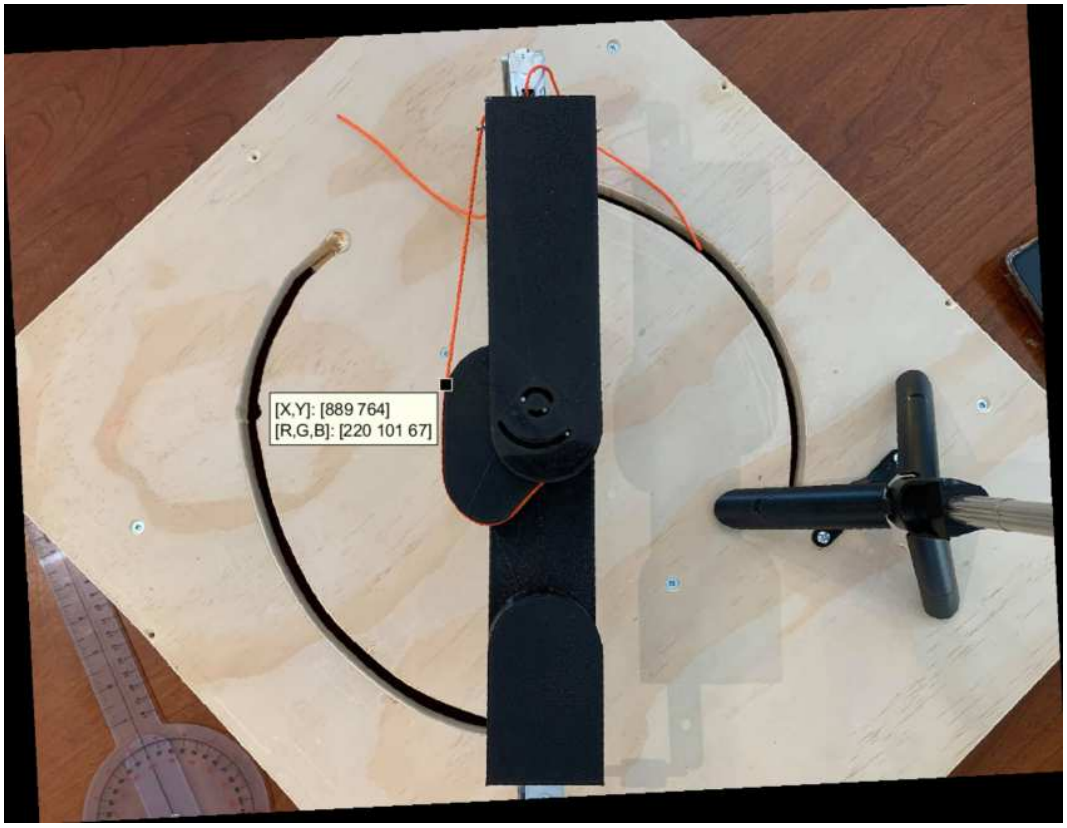

Figure 6.10. Manual identification of the last point of contact between the cable and pulley using data cursor in MATLAB.

These values are normalized and plotted against the shape of the pulley, as can be seen in Figure 6.11. These normalized coordinates in mm are denoted by $(x_{contact\ new}, y_{contact\ new})$.

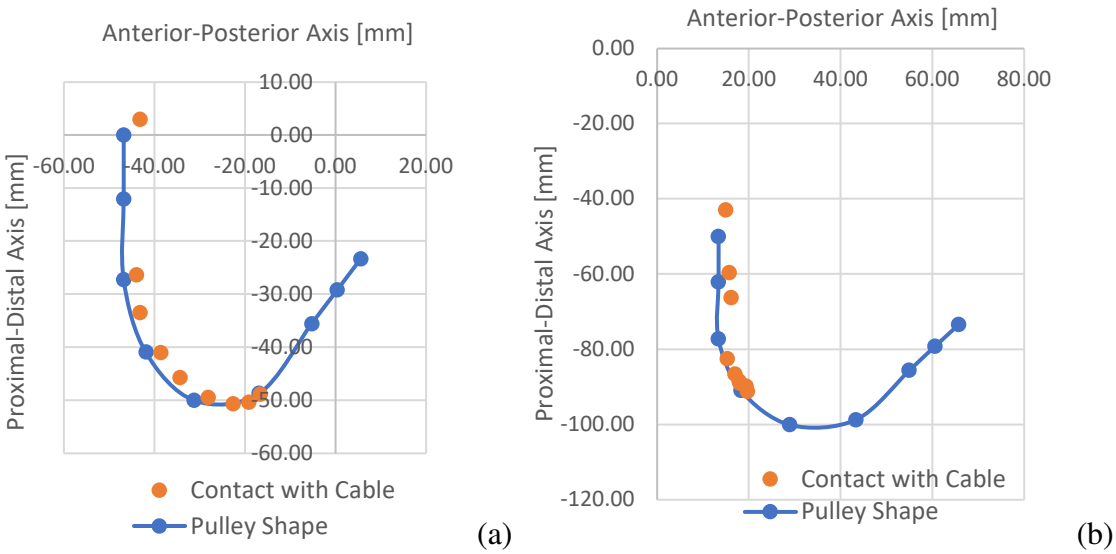

Figure 6.11. Cable contact experimental results. Last points of contact between the cable and the pulley shown by orange points. Pulley shape shown by blue curves. (a) Joint with no offset. (b) Joint with offset.

Visibly, the cable contact locations were not as described by simulations. Due to the physical structure of the joints and the location of eyelets, the cable stayed wrapped around the anterior portion of the pulley for the entire ROM.

Intuitively, when plotted, the points of contact between the cable and pulley follow the shape of the pulley. It is also clear that there is a degree of error with the translation of reference frames for this experiment. This is evident because the orange curves are anterior and proximal to the blue curves. It is physically impossible that the cable's last points of contact are inside the pulley. This can likely be attributed to the manual selection of points in MATLAB using the data cursor, which introduces human error. It is also possible that photographs were taken at an angle and that the process used to normalize images was insufficient to handle this factor.

Throughout simulations, the moment arm generated by the cable was measured from the ICR. Thus, the following equation was used to generate moment arm plots visible in Figure 6.12.

$$M = \sqrt{(x_{contact\ new} - x_{TRnew})^2 + \left(y_{TLnew} - y_{TRnew}\right)^2} \tag{6.7}$$

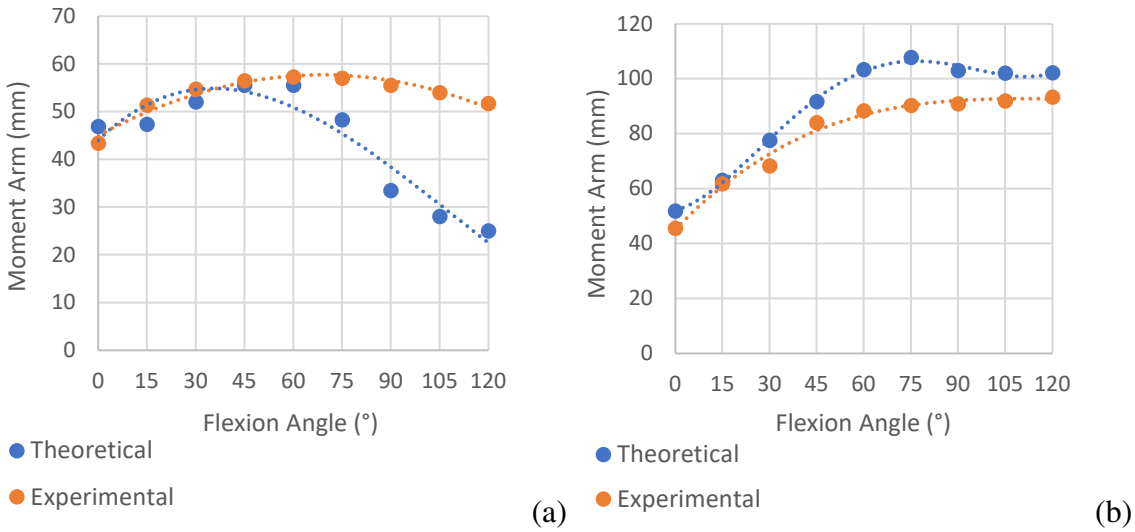

Figure 6.12. Knee moment arm experimental results. (a) Joint with no offset. (b) Joint with offset.

To quantify the degree of error between experimental and theoretical moment arms, percent and absolute errors were calculated for both joints. Figures 6.13 and 6.14 present these results.

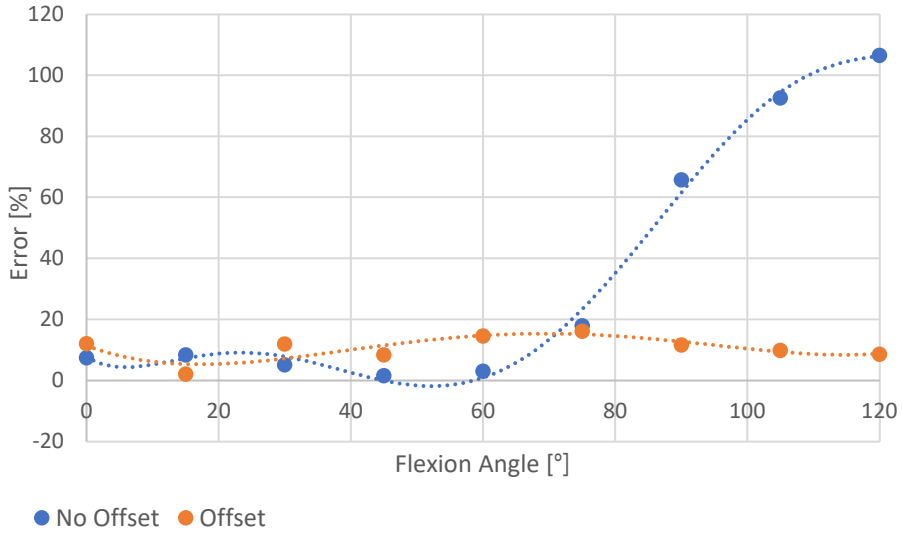

Figure 6.13. Moment arm experimental percent error for both joint prototypes.

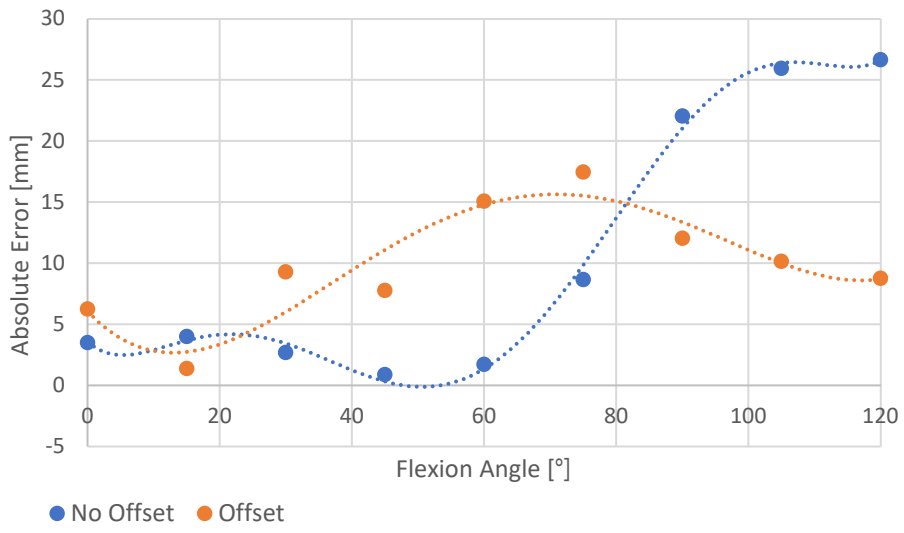

Figure 6.14. Moment arm experimental absolute error for both joint prototypes.

Though both joints achieve the full ROM of flexion and extension desired, the moment arms generated by the joints were not expected. This is reflected in the percent error values obtained; the joint with no offset had an average error value of 34.33%, and the joint with offset had an average error value of 10.65%.

Pulley shapes were designed based on a geometrical angle measurement from 0° to 120°, but experimental results showed that other factors influence the cable's ability to adhere to the desired points of contact. In the joint with no offset, the experimental data follows an inverted parabolic shape consistent with the first 75° of reference data. This is logical since the contact points between the cable and the pulley only reached the point on the pulley designed for 75°.

A second iteration of design could be generated in the future, knowing that the cable cannot create moment arms at locations past this point. A second iteration of the pulley shape would need to consider the location of eyelets to ensure that all designed portions of the pulley become the last point of contact with the cable throughout the ROM. This could be achieved by retracing the experimental results in Figure 6.12 and adjusting the coordinates of the points that make up the pulley shape to achieve the desired fluctuation in moment arm magnitude.

The primary purpose of the offset joint was to validate the kinematics of the device, which proved to be successful. The same pulley shape was implemented on both joints to see if their behaviour would differ. As visible in the simulated curve, the offset pulley shape was not similar to the reference data. Thus, it is rational that the experimental data also does not follow

the desired moment arm curve. It is indeed possible to alter the shape of this pulley in the same way that it would be for the joint with no offset. The main difference is that in this design, the points of contact of the cable only reached the pulley's designed points between 45° and 60°, compared to 75° as with the joint with no offset.

Though the moment arms achieved do not closely follow the reference data, this experimental testing proves that the design can successfully change the moment arm throughout flexion and can be adjusted and adapted to work with many types of actuators.

6.3 Degree of Freedom Analysis

In order to verify that both joints only have one solution to flex and extend between 0° and 120°, a second testing rig was used. Results are visually inspected to check that only a single curve is drawn over the ten cycles of flexion/extension. The curves obtained through this experiment can be seen in Figures Figure *6.15* and Figure *6.16*.

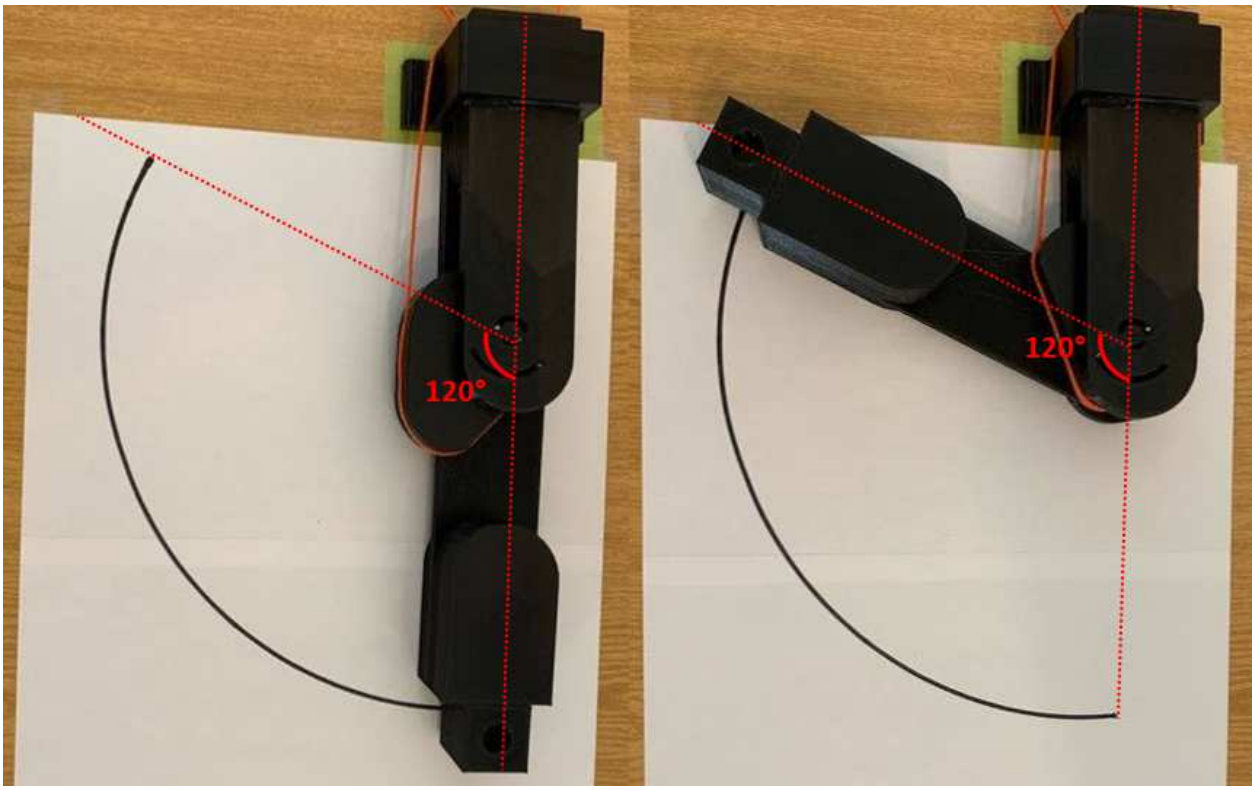

Figure 6.15. Experimental DOF results for joint with no offset. Permanent marker removed for clarity.

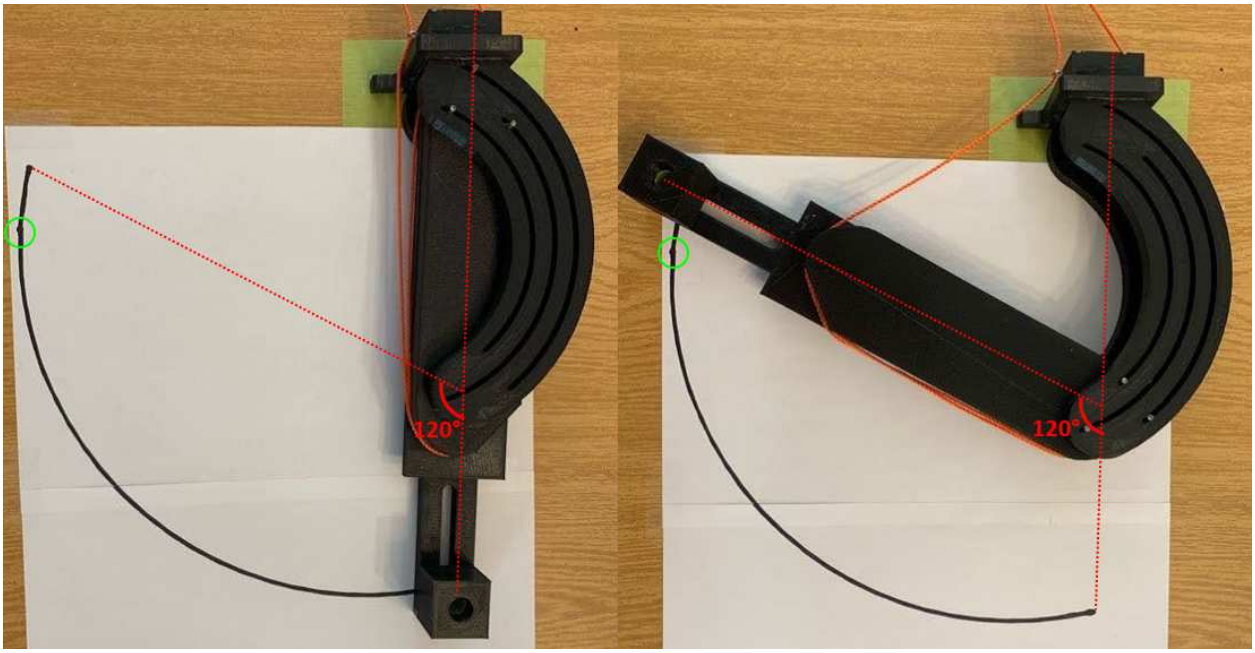

Figure 6.16. Experimental DOF results for joint with offset. Permanent marker removed for clarity. Imperfection circled in green.

Though it was not the purpose of this experiment, the ability of both joints to effectively transfer force was validated. As expected, pulling on the two posterior and anterior ends of each cable caused the joints to flex and extend, respectively.

It is clear from Figure 6.15 and Figure 6.16 that only a single kinematic solution is available throughout the movement of both joints. The only identifiable point where the curve is not continuously smooth was present in the results from the joint with offset. At a point between 105° and 120° flexion, the metal pins were experiencing too much friction against the paths. This is likely due to the imperfect shape of the pins and the fact that the 3D-printed components are not perfectly smooth. An introduction of bushings on the pins could prove beneficial to resolve this problem. It would also reduce the relative clearance between the pins and their slots, as this is a limitation of the test and introduces additional DOFs. In different loading situations, the pins may be gliding along one side of the slots or the other.

Otherwise, both joints visibly have a single smooth curve drawn throughout the entire ROM after ten test cycles, proving that the joints have one DOF. This was desired and is characteristic of the type of joints designed: polycentric joints that follow pre-defined rotation paths.

6.4 Discussion

The two main objectives of this research, as presented in section 1.3, were to improve the kinematic compatibility between a WAE user and the device knee joint and improve performance by optimizing the actuation system force and moment delivery to the knee joint.

Overall, the problem of improving ergonomics was addressed by using a pin-in-slot design. This type of design improved the kinematic compatibility of the joint while maintaining an appropriate ROM of 0° to 120° flexion. It also prevents hyperextension and hyperflexion without needing an additional mechanism or stopper and can accommodate an offset in the sagittal plane and maintain kinematic compatibility.

Throughout the design process, several alterations and simplifications were made. These ranged from adding a third pin and slot to improve stability and reliability to carefully selecting the combination of pin paths to ensure a single kinematic solution.

When it comes to the issue of performance, the use of a noncircular pulley showed a successful proof of concept. The moment arm can indeed be varied throughout flexion by this design, and future iterations could optimize the pulley shape.

Chapter 7. Conclusions and Recommendations

7.1 Conclusion

A design for a polycentric knee joint that can accommodate an offset, optimize force delivery and contraction distance, and be integrated into a powered WAE was proposed. Based on a literature review and simulations of existing joint designs, the joint type with a pre-defined path of ICR was selected. Two preliminary prototypes, one without and one with offset, were fabricated primarily out of PLA with steel pins. To experimentally validate the joints, photos were taken at 15° intervals from 0° to 120° flexion. The cable was manually pulled taut and clipped in place between movements. The resulting images were analyzed in MATLAB, and the locations of pins and last point of contact between the cables and pulleys were manually identified. Results showed that the pins on both joints appear to follow their simulated paths. The joint with no offset had an average kinematic absolute error of 0.32 mm, and the joint with offset had an average of 1.68 mm absolute error. The pins were not centered along their paths were not distributed at equal distances at 15° intervals as expected. This error can be attributed to the fabrication of the prototypes. Though both joints achieve the full ROM of flexion and extension desired, experimental moment arms were not as seen in simulations. The joint with no offset had a substantial percent error of 34.33%, and the joint with offset had an error of 10.65%. Regardless, this experimental testing proves that the design can successfully provide a change in moment arm throughout flexion and can be adjusted and adapted to work with many types of actuators.

A second experimental setup was used to validate that the joints only have one DOF. The femoral components of both joints were fixed to a plywood board, and tension was applied to the posterior and anterior cables to flex and extend the joint, respectively. Ten cycles of flexion and extension were carried out, and a single curve was drawn for each joint. Based on visual inspection, the joints were confirmed to have a single kinematic solution, which is desired in polycentric joints that follow pre-defined rotation paths.

The proposed design makes significant contributions to research on powered WAE knee joints that pay attention to ergonomics. This is an invaluable research endeavour as the elderly are becoming increasingly dependent on mobility assistance. In order to preserve the independence of elderly individuals, it is essential to continue research efforts to optimize these devices.

7.2 Scope and Limitations

The scope of this thesis includes a review of existing literature followed by design and modelling. Preliminary prototypes were created and tested in experimental conditions, but the strength and durability of the prototypes were not considered. This research has limitations relating to the lack of robust prototypes, actuator integration, and human testing.

7.3 Future Work

This research has shown that there is room for improvement in both prototype design and experimental testing methods.

7.3.1 Design Model

The physical construction of the prototypes caused a significant amount of error in the results. Future iterations of the joints should be machined entirely out of steel, as this would ensure that any rough edges experienced in the 3D-printed prototypes are not present. In addition, the prototype bodies and pins could be machined together. In contrast to manually adhering steel pins to PLA bodies with CA, this type of fabrication would eliminate pins not being perfectly perpendicular to the component surfaces. To further reduce any friction and allow minimal clearance between the paths and pins, bushings could be added to the pins. This would allow smoother flexion and extension.

The shapes of the pulleys should also be altered to reflect the experimental testing results. Ideally, these pulleys would closely match the reference moment arm data. Extensor and flexor moment arms should both be represented throughout extension and flexion, respectively. The location of eyelets also impacted how closely the experimental data reflected the moment arm simulations. If the length of the femoral components is extended, the eyelets could be placed more proximally up the leg, providing the cable more freedom to reach anterior portions of the pulley. The screw-in eyelets should be replaced by pretensioner pulleys in future prototypes, as described in section 3.5.

7.3.2 Testing Improvements

Further testing would also be beneficial to this research effort. Instead of manually pulling on the cable to flex and extend the joint by 15° at a time, it would be beneficial to introduce a crank mechanism. A crank and cable drum could be added proximally to the femoral component and connected to both ends of the cable. When rotated by a given degree, the cable would be under tension on one side, and slack would be provided on the other, resulting in flexion or extension of the joint.

Video could be captured throughout the entire ROM instead of relying on images taken at 15° intervals. Then, video processing in MATLAB would be used to analyze the data and would not require the manual identification of points.

Once the prototype is fabricated using a material such as steel, strength testing should also be carried out. Designing and building an actuation system would also be beneficial in the testing process of the proposed joints, as it would allow for kinetic tests. Using an actuator to flex and extend the joints would reduce human intervention in the experiments, thereby reducing human error and resulting in repeatable experiments.

The strapping and human-device interface will also need to be designed and evaluated thoroughly. Further research on appropriate methods of attaching the joint to a user would eventually lead to human trials.

References

[1] S. C. Government of Canada, "Population estimates on July 1st, by age and sex," Sep. 29, 2020. https://www150.statcan.gc.ca/t1/tbl1/en/tv.action?pid=1710000501 (accessed Apr. 30, 2021).

[2] E. and S. D. Canada, "Report on housing needs of seniors," *aem*, Jul. 11, 2019. https://www.canada.ca/en/employment-social-development/corporate/seniors/forum/report-seniors-housing-needs.html (accessed Nov. 12, 2019).

[3] J. Shafrin, J. Sullivan, D. P. Goldman, and T. M. Gill, "The association between observed mobility and quality of life in the near elderly," *PLoS One*, vol. 12, no. 8, Aug. 2017, doi: 10.1371/journal.pone.0182920.

[4] M. E. Dallas, "Weak Knees Large Cause of Falls in Older People," *WebMD*, 2016. https://www.webmd.com/healthy-aging/news/20160211/weakened-knees-a-big-cause-of-falls-for-older-people-study (accessed Feb. 21, 2020).

[5] L. Saccares, I. Sarakoglou, and N. G. Tsagarakis, "It-knee: An exoskeleton with ideal torque transmission interface for ergonomic power augmentation," 2016, vol. 2016-November, pp. 780–786. doi: 10.1109/IROS.2016.7759140.

[6] B. Choi *et al.*, "A self-aligning knee joint for walking assistance devices," in *2016 38th Annual International Conference of the IEEE Engineering in Medicine and Biology Society (EMBC)*, Aug. 2016, pp. 2222–2227. doi: 10.1109/EMBC.2016.7591171.

[7] L. Levesque, S. Pardoel, Z. Lovrenovic, and M. Doumit, "Experimental comfort assessment of an active exoskeleton interface," in *2017 IEEE International Symposium on Robotics and Intelligent Sensors (IRIS)*, Oct. 2017, pp. 38–43. doi: 10.1109/IRIS.2017.8250095.

[8] B-Temia, "Keeogo," *B-Temia Keeogo+*. https://b-temia.com/keeogo/ (accessed Oct. 15, 2021).

[9] Indego, "Personal Use | Indego Exoskeleton," *Indego Personal Exoskeleton*. http://www.indego.com/indego/us/en/indego-personal (accessed Oct. 15, 2021).

[10] "CYBERDYNE," *HAL for Well-Being Lower Limb Type Pro*. https://cyberdyne.jp/english/products/fl05.html (accessed Oct. 15, 2021).

[11] A. H. A. Stienen, E. E. G. Hekman, F. C. T. van der Helm, and H. van der Kooij, "Self-Aligning Exoskeleton Axes Through Decoupling of Joint Rotations and Translations," *IEEE Transactions on Robotics*, vol. 25, no. 3, pp. 628–633, Jun. 2009, doi: 10.1109/TRO.2009.2019147.

[12] M. B. Näf, K. Junius, M. Rossini, C. Rodriguez-Guerrero, B. Vanderborght, and D. Lefeber, "Misalignment Compensation for Full Human-Exoskeleton Kinematic Compatibility: State of the Art and Evaluation," *Appl. Mech. Rev*, vol. 70, no. 5, pp. 050802-050802–19, Feb. 2019, doi: 10.1115/1.4042523.

[13] D. Wang, J. Guo, K. Lee, C. Yang, and H. Yu, "An adaptive knee joint exoskeleton based on biological geometries," *2011 IEEE International Conference on Robotics and Automation*, pp. 1386–1391, 2011, doi: 10.1109/ICRA.2011.5979761.

[14] P. Komdeur, F. E. Pollo, and R. W. Jackson, "Dynamic knee motion in anterior cruciate impairment: a report and case study," *Proc (Bayl Univ Med Cent)*, vol. 15, no. 3, pp. 257–259, Jul. 2002.

[15] M. A. Ergin and V. Patoglu, “A self-adjusting knee exoskeleton for robot-assisted treatment of knee injuries,” in *2011 IEEE/RSJ International Conference on Intelligent Robots and Systems*, Sep. 2011, pp. 4917–4922. doi: 10.1109/IROS.2011.6095073.
[16] V. A. Cai, P. Bidaud, V. Hayward, F. Gosselin, and E. Desailly, “Self-adjusting, isostatic exoskeleton for the human knee joint.,” *Conference proceedings : ... Annual International Conference of the IEEE Engineering in Medicine and Biology Society. IEEE Engineering in Medicine and Biology Society. Conference*, vol. 2011, pp. 612–618, 2011.
[17] B. Celebi, M. Yalcin, and V. Patoglu, “AssistOn-Knee: A self-aligning knee exoskeleton,” 2013, pp. 996–1002. doi: 10.1109/IROS.2013.6696472.
[18] K.-M. Lee and J. Guo, “Kinematic and dynamic analysis of an anatomically based knee joint,” *Journal of Biomechanics*, vol. 43, no. 7, pp. 1231–1236, May 2010, doi: 10.1016/j.jbiomech.2010.02.001.
[19] J. J. O’Connor, T. L. Shercliff, E. Biden, and J. W. Goodfellow, “The Geometry of the Knee in the Sagittal Plane,” *Proc Inst Mech Eng H*, vol. 203, no. 4, pp. 223–233, Dec. 1989, doi: 10.1243/PIME_PROC_1989_203_043_01.
[20] F. Russell, R. Vaidyanathan, and P. Ellison, “A Kinematic Model for the Design of a Bicondylar Mechanical Knee,” in *2018 7th IEEE International Conference on Biomedical Robotics and Biomechatronics (Biorob)*, Aug. 2018, pp. 750–755. doi: 10.1109/BIOROB.2018.8487734.
[21] P. J. Rowe, C. M. Myles, C. Walker, and R. Nutton, “Knee joint kinematics in gait and other functional activities measured using flexible electrogoniometry: how much knee motion is sufficient for normal daily life?,” *Gait Posture*, vol. 12, no. 2, pp. 143–155, Oct. 2000, doi: 10.1016/s0966-6362(00)00060-6.
[22] S. Sipilä and H. Suominen, “Knee extension strength and walking speed in relation to quadriceps muscle composition and training in elderly women,” *Clinical Physiology*, vol. 14, no. 4, pp. 433–442, 1994, doi: 10.1111/j.1475-097X.1994.tb00402.x.
[23] L. Levesque and M. Doumit, “Study of Human-Machine Physical Interface for Wearable Mobility Assist Devices,” *Medical Engineering & Physics*, May 2020, doi: 10.1016/j.medengphy.2020.03.008.
[24] M. O. Heller *et al.*, “A new model to predict in vivo human knee kinematics under physiological-like muscle activation,” *Journal of Biomechanics*, vol. 40, pp. S45–S53, Jan. 2007, doi: 10.1016/j.jbiomech.2007.03.005.
[25] P. S. Walker, H. Kurosawa, J. S. Rovick, and R. A. Zimmerman, “External knee joint design based on normal motion.,” *Journal of rehabilitation research and development*, vol. 22, no. 1, pp. 9–22, 1985, doi: 10.1682/jrrd.1985.01.0009.
[26] H. Terada, Y. Zhu, M. Suzuki, C. Cheng, and R. Takahashi, “Developments of a Knee Motion Assist Mechanism for Wearable Robot with a Non-circular Gear and Grooved Cams,” in *Mechanisms, Transmissions and Applications*, Dordrecht, 2012, pp. 69–76. doi: 10.1007/978-94-007-2727-4_6.
[27] G. M. Bapat and S. Sujatha, “A Method for Optimal Synthesis of a Biomimetic Four-Bar Linkage Knee Joint for a Knee-Ankle-Foot Orthosis,” *JBBBE*, vol. 32, pp. 20–28, May 2017, doi: 10.4028/www.scientific.net/JBBBE.32.20.
[28] N. Dhameliya, “The Quadriceps muscle Anatomy, Location, Function, Exercise, Injury,” *SAMARPAN PHYSIOTHERAPY CLINIC AHMEDABAD*, Aug. 31, 2021. https://samarpanphysioclinic.com/the-quadriceps-muscle-the-king-of-muscular-systom/ (accessed Oct. 30, 2021).

[29] C. W. Spoor and J. L. Van Leeuwen, “Knee muscle moment arms from MRI and from tendon travel,” *Journal of Biomechanics*, vol. 25, no. 2, pp. 201–206, Feb. 1992, doi: 10.1016/0021-9290(92)90276-7.
[30] A. Fick, “Ueber zweigelenkige Muskeln,” *Anatomie Entwicklungsgeschichte*, vol. 3, pp. 201–239, 1879.
[31] L. F. Draganich, T. P. Andriacchi, and G. B. J. Andersson, “Interaction between intrinsic knee mechanics and the knee extensor mechanism,” *Journal of Orthopaedic Research*, vol. 5, no. 4, pp. 539–547, 1987, doi: https://doi.org/10.1002/jor.1100050409.
[32] E. S. Grood, W. J. Suntay, F. R. Noyes, and D. L. Butler, “Biomechanics of the knee-extension exercise. Effect of cutting the anterior cruciate ligament,” *J Bone Joint Surg Am*, vol. 66, no. 5, pp. 725–734, Jun. 1984.
[33] J. Murillo, M. Doumit, and N. Baddour, “Validation of Pneumatic Artificial Muscle for Powered Transfemoral Prostheses,” *CMBES Proc.*, vol. 36, May 2013, Accessed: Apr. 27, 2021. [Online]. Available: https://proceedings.cmbes.ca/index.php/proceedings/article/view/374
[34] D. J. Hyun, H. Park, T. Ha, S. Park, and K. Jung, “Biomechanical design of an agile, electricity-powered lower-limb exoskeleton for weight-bearing assistance,” *Robotics and Autonomous Systems*, vol. 95, pp. 181–195, 2017, doi: 10.1016/j.robot.2017.06.010.
[35] J. L. Lewis, W. D. Lew, C. M. Patrnchak, and G. T. Shybut, “A New Concept in Orthotics Joint Design—The Northwestern University Knee Orthosis System,” p. 9.
[36] A. Schiele and F. C. T. van der Helm, “Kinematic Design to Improve Ergonomics in Human Machine Interaction,” *IEEE Transactions on Neural Systems and Rehabilitation Engineering*, vol. 14, no. 4, pp. 456–469, Dec. 2006, doi: 10.1109/TNSRE.2006.881565.
[37] S. Kittisares, H. Nabae, G. Endo, K. Suzumori, and R. Sakurai, “Design of knee support device based on four-bar linkage and hydraulic artificial muscle,” *Robomech J*, vol. 7, no. 1, Art. no. 1, Dec. 2020, doi: 10.1186/s40648-020-00165-2.
[38] R. K. P. S. Ranaweera *et al.*, “Anthro-X: Anthropomorphic lower extremity exoskeleton robot for power assistance,” in *2018 4th International Conference on Control, Automation and Robotics (ICCAR)*, Apr. 2018, pp. 82–87. doi: 10.1109/ICCAR.2018.8384649.
[39] G. Alrezage, M. Tokhi, and S. Ali, *DESIGN AND CONTROL OF EXOSKELETON FOR ELDERLY MOBILITY*. 2015, p. 74. doi: 10.1142/9789814725248_0012.
[40] T. de A. Busch *et al.*, “Factors associated with lower gait speed among the elderly living in a developing country: a cross-sectional population-based study,” *BMC Geriatrics*, vol. 15, no. 1, p. 35, Apr. 2015, doi: 10.1186/s12877-015-0031-2.
[41] J.-Y. Kuan, K. A. Pasch, and H. M. Herr, “Design of a knee joint mechanism that adapts to individual physiology,” in *2014 36th Annual International Conference of the IEEE Engineering in Medicine and Biology Society*, Aug. 2014, pp. 2061–2064. doi: 10.1109/EMBC.2014.6944021.
[42] Y. Lee *et al.*, “Biomechanical Design of a Novel Flexible Exoskeleton for Lower Extremities,” *IEEE/ASME Transactions on Mechatronics*, vol. 22, no. 5, pp. 2058–2069, Oct. 2017, doi: 10.1109/TMECH.2017.2718999.
[43] R. C. Browning, J. R. Modica, R. Kram, and A. Goswami, “The effects of adding mass to the legs on the energetics and biomechanics of walking,” *Med Sci Sports Exerc*, vol. 39, no. 3, pp. 515–525, Mar. 2007, doi: 10.1249/mss.0b013e31802b3562.
[44] “2554 / KNEE BRACE - HINGED BARS,” *OTCBrace*. https://otcbrace.com/products/2554-otc (accessed Jun. 19, 2021).

[45] B. P. Doyle and C. Road, “KNEE ORTHOSIS AND HINGE JOINT,” US 6,402,713 B1, Jun. 11, 2002 [Online]. Available: https://patentimages.storage.googleapis.com/85/2d/95/78257a19530c2d/US6402713.pdf

[46] K. Kim, M. Kang, Y. Choi, H. Jang, J. Han, and C. Han, “Development of the exoskeleton knee rehabilitation robot using the linear actuator,” *International Journal of Precision Engineering and Manufacturing*, vol. 13, no. 10, pp. 1889–1895, 2012, doi: 10.1007/s12541-012-0248-3.

Appendix A – Supplementary Design Information

A.1 First Iteration of the Joint with Offset

The first experimental prototype created for the joint with offset identified an opportunity for improvement.

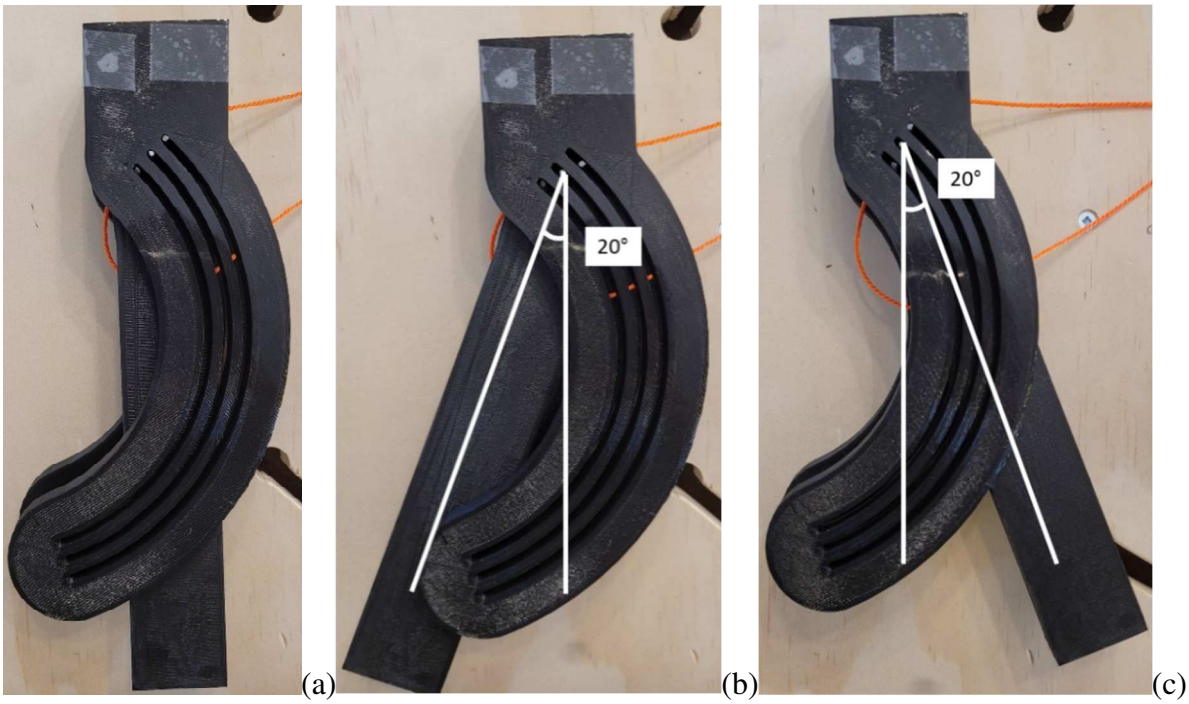

Figure A.1. First iteration of the joint with offset with pins at 0°. (a) Joint at 0° flexion, (b) 20° flexion, (c) 20° extension.

One of the design criteria was that the joint must have a single DOF, meaning that throughout cycles of flexion and extension, identical kinematics are recreated. Conversely, it is evident that the two external pins (1 and 3) can rotate around pin 2. This motion causes pin 2 to become the new ICR, which is undesirable. This added DOF allowed approximately 20° of flexion and extension for a total of 40°, which was deemed not negligible. Thus, a second design iteration was required.

Appendix B – MATLAB Code


```
clc;
clear;
fig1 = figure;
%% INPUT CONSTANT PARAMETERS
syms theta;
F = 20; %force applied by cable [N]
pathWidth = 3; %width of pin paths [mm]
degOffset1 = 131; %offset between path 1 and path 2 with no misalignment
n = 8; %number of lines desired -1
n2 = 3; %index for simulation of double-hinge gear joint
thetaValue = 0; %theta for joint with and without misalignment
thetaValue2 = 0; %theta for double-hinge gear joint
r = 2; %radius of gears for double-hinge gear joint[mm]
r1 = 4.5; %radius of gears for double-hinge gear joint[mm]
r2 = 7; %radius of gears for double-hinge gear joint[mm]

%Defining range of motion
thetaMin=0;
thetaMax=120;

%Prescribed misalignment of the device with respect to true ICR
%This gives the location of the device's origin, on the coordinate system
%of the biological ICR
xM= 40;
yM= 0;

%% DEFINE PATHS - NO MISALIGNMENT
%Path 1 (displacement of ICR in x and y)
%Using data from: Walker et al. https://pdfs.semanticscholar.↙
org/d11d/382cf415aeaa3037c38f3b82dc1a49ef75fc.pdf
x1=-0.0602*theta + 0.0000178*theta^2;
y1=-0.05125*theta + 0.000308*theta^2;
%Path 2
x2Diff = 10; %location of pin 2 wrt pin 1
y2Diff = -10;
d12 = sqrt((abs(x2Diff))^2+(abs(y2Diff))^2); %distance from pin 1 to pin 2
theta2 = abs(rad2deg(atan(x2Diff/y2Diff))); %angle between d12 and y-axis
x2 = x1 + d12*sin(deg2rad(theta2 - theta));
y2 = y1 - d12*cos(deg2rad(theta2 - theta));
%Path 3
x3Diff = -10; %location of pin 3 wrt pin 1
y3Diff = 5;
d13 = sqrt((abs(x3Diff))^2+(abs(y3Diff))^2); %distance from pin 1 to pin 3
theta3 = abs(rad2deg(atan(x3Diff/y3Diff))); %angle between d13 and y-axis
x3 = x1 - d13*sin(deg2rad(theta3 - theta));
y3 = y1 + d13*cos(deg2rad(theta3 - theta));
%% DEFINE PATHS - MISALIGNMENT
%Path 1 with misalignment
x1Diff_M = 50; %location of pin 1 wrt origin
```

```
y1Diff_M = 60;
db1_M = sqrt((abs(x1Diff_M))^2+(abs(y1Diff_M))^2); %distance from origin to pin 1
theta1_M = abs(rad2deg(atan(y1Diff_M/x1Diff_M)));
x1M = x1 + db1_M*cos(deg2rad(theta1_M - theta));
y1M = y1 + db1_M*sin(deg2rad(theta1_M - theta));
%Path 2 with misalignment
x2Diff_M = 20; %location of pin 2 wrt origin
y2Diff_M = 65;
d12_M = sqrt((x2Diff_M)^2+(y2Diff_M)^2);
theta2_M = abs(rad2deg(atan(y2Diff_M/x2Diff_M)));
x2M = x1 + d12_M*cos(deg2rad(theta2_M - theta));
y2M = y1 + d12_M*sin(deg2rad(theta2_M - theta));
%Path 3 with misalignment
x3Diff_M = 30; %location of pin 3 wrt origin
y3Diff_M = 85;
d13_M = sqrt((abs(x3Diff_M))^2+(abs(y3Diff_M))^2);
theta3_M = abs(rad2deg(atan(y3Diff_M/x3Diff_M)));
x3M = x1 + d13_M*cos(deg2rad(theta3_M - theta));
y3M = y1 + d13_M*sin(deg2rad(theta3_M - theta));


for index = 1:n+1 %(evaluating at 20 degree intervals)
    %% Original path 2 (no misalignment taken into account)
    %evaluate coordinates of pin 1
    point_x1 = -0.0602*thetaValue + 0.0000178*thetaValue^2;
    point_y1 = -0.05125*thetaValue + 0.000308*thetaValue^2;
      % pin 1 at 1 degree further down the track - used for calculating gamma
        point_x1B = -0.0602*(thetaValue+1) + 0.0000178*(thetaValue+1)^2;
        point_y1B = -0.05125*(thetaValue+1) + 0.000308*(thetaValue+1)^2;
    %evaluate coordinates of pin 2
    omegaValue = (180 - thetaValue)/2;
    point_x2 = point_x1  + (d12*sin(deg2rad(theta2-thetaValue)));
    point_y2 = point_y1  - (d12*cos(deg2rad(theta2-thetaValue)));

    %evaluate coordinates of pin 3
    epsilonValue = (180 - thetaValue)/2;
    point_x3 = point_x1 - (d13*sin(deg2rad(theta3 - thetaValue)));
    point_y3 = point_y1 + (d13*cos(deg2rad(theta3 - thetaValue)));
    L = sqrt((point_x1 - point_x3)^2+(point_y1 - point_y3)^2);

    %calculating phi = the angle of R wrt the horizontal ( (+) above, (-) below)
    phi = atand((point_y2 - point_y1)/(point_x2 - point_x1));

    %calculating gamma = the angle between path 1 and horizontal
    gamma = (atand ((point_y1B - point_y1)/(point_x1B - point_x1)));

    %declaring arrays for location of pins 1, 2 and 3
    xLinePart1 = [point_x2, point_x1]; %line from pin 2 to pin 1
    yLinePart1 = [point_y2, point_y1];
```

```
    xLinePart2 = [point_x1, point_x3]; %line from pin 1 to pin 3
    yLinePart2 = [point_y1, point_y3];


    %% New path 2 (misalignment taken into account)
    %evaluate coordinates of pin 1
    point_x1_M = point_x1 + dbl_M*cos(deg2rad(theta1_M - thetaValue));
    point_y1_M = point_y1 + dbl_M*sin(deg2rad(theta1_M - thetaValue));

    %evaluate coordinates of  pin 2
    point_x2_M = point_x1 + d12_M*cos(deg2rad(theta2_M - thetaValue));
    point_y2_M = point_y1 + d12_M*sin(deg2rad(theta2_M - thetaValue));

    %evaluate coordinates of  pin 2
    point_x3_M = point_x1 + d13_M*cos(deg2rad(theta3_M - thetaValue));
    point_y3_M = point_y1 + d13_M*sin(deg2rad(theta3_M - thetaValue));

    %declaring arrays for location of pins 1, 2 and 3
    xLine_M1 = [point_x1_M, point_x2_M]; %line from pin 1 to pin 2
    yLine_M1 = [point_y1_M, point_y2_M];
    xLine_M2 = [point_x1_M, point_x3_M]; %line from pin 1 to pin 3
    yLine_M2 = [point_y1_M, point_y3_M];

    %% Plotting lines at 20 degree intervals
    %Figure 1 NO MISALIGNMENT
    subplot(1,2,1);
    hold on
    %plot(xLinePart1, yLinePart1);
    %plot(xLinePart2, yLinePart2);

    %Figure 2 WITH MISALIGNMENT
    subplot(1,2,2);
    hold on
    %plot(xLine_M1, yLine_M1);
    %plot(xLine_M2, yLine_M2);
thetaValue = thetaValue + 120/n;
end  %end of for loop

%% FORMATTING FIGURES
%Extract axes handles of all subplots from the figure
axesHandles = findobj(get(fig1,'Children'), 'flat','Type','axes');
%Set the axis property to
axis(axesHandles,'square')

%% PLOT PATHS ON FIGURES 1 AND 2
subplot(1,2,1); %figure 1 - No misalignment
    hold on
    %title('Design Concept')
    xlabel('Anterior-posterior axis [mm]')
```

```
    ylabel('Proximal-distal axis [mm]')
    axis([-30 30 -30 30]) %scale
    grid on
    fplot(x1, y1, [thetaMin thetaMax], 'b') %pin 1 (ICR)
    fplot(x2, y2, [thetaMin thetaMax], 'r') %pin 2
    fplot(x3, y3, [thetaMin thetaMax], 'K') %pin 3

subplot(1,2,2); %figure 2 - With misalignment
    hold on
    %title('Design Concept with Misalignment')
    xlabel('Anterior-posterior axis [mm]')
    ylabel('Proximal-distal axis [mm]')
    axis([-100 100 -100 100]) %scale
    fplot(x1, y1, [thetaMin thetaMax], 'b') %ICR
    fplot(x1M, y1M, [thetaMin thetaMax], 'c') %path 1
    fplot(x2M, y2M, [thetaMin thetaMax], 'r') %path 2
    fplot(x3M, y3M, [thetaMin thetaMax], 'k') %path 3

    grid on

%% Simulation of double-hinge joint (spur gears)
%generate second figure window
fig2 = figure;

subplot(1,2,1); %Figure 1
    hold on
    xlabel('Anterior-posterior axis [mm]')
    ylabel('Proximal-distal axis [mm]')
    axis([-60 60 -60 60]) %scale
    syms x y
    fimplicit((x).^2 + (y-r).^2 -r^2);
    grid on

subplot(1,2,2); %Figure 2
    hold on
    xlabel('Anterior-posterior axis [mm]')
    ylabel('Proximal-distal axis [mm]')
    axis([-10 2 -4 10]) %scale
    grid on

for index2 = 1:n2+1
%% Simulation of double-hinge joint (spur gears)
a = 2*r;
b = r;
aAngle = 180 - thetaValue2;
bAngle = rad2deg(asin((sin(deg2rad(aAngle)))/2));
cAngle = 180 - bAngle - aAngle;
c = (a^2 + b^2 - 2*a*b*cos(deg2rad(cAngle)))^(1/2);
thighGearX = 0;%-1*c*sin(deg2rad(thetaValue2));
```

```
thighGearY = r;%-l*c*cos(deg2rad(thetaValue2));
shankGearX = -l*c*sin(deg2rad(thetaValue2));
shankGearY = -l*c*cos(deg2rad(thetaValue2));

%Draw line from center of one gear to the other
%Shank gear center
point_xHingeMid_1 = shankGearX; %0;
point_yHingeMid_1 = shankGearY; %-r;
%Thigh gear center
point_xHingeMid_2 = 0; % thighGearX;
point_yHingeMid_2 = r; %thighGearY;
%Line coordinates
xHingeMid = [point_xHingeMid_1, point_xHingeMid_2];
yHingeMid = [point_yHingeMid_1, point_yHingeMid_2];

%Draw line from center of shank gear down shank
point_xHingeShank = 200*sin(deg2rad(thetaValue2+180));
point_yHingeShank = 200*cos(deg2rad(thetaValue2+180));
xHingeShank = [point_xHingeMid_1, point_xHingeShank];
yHingeShank = [point_yHingeMid_1, point_yHingeShank];

%Draw line from center of thigh gear up thigh
xHingeThigh = [point_xHingeMid_2, 0];
yHingeThigh = [point_yHingeMid_2, 200];

%Find ICR
icrX = -l*r*sin(deg2rad(cAngle));
icrY = -l*r*cos(deg2rad(cAngle))+r;

subplot(1,2,1); %Figure 1
%title('Simulation of Double-Hinge Gear Joint')
axis([-10 10 -10 10]) %scale
syms x y
fimplicit((x-shankGearX).^2 + (y-shankGearY).^2 -r^2);
plot(xHingeShank, yHingeShank);
plot(xHingeMid, yHingeMid);
plot(xHingeThigh, yHingeThigh);
plot(icrX, icrY, 'o');

thetaValue2 = thetaValue2 + thetaMax/n2;
end

aAngleGen = 180 - theta;
bAngleGen = rad2deg(asin((sin(deg2rad(aAngleGen)))/2));
cAngleGen = 180 - bAngleGen - aAngleGen ;
hingeIcrX = -l*r*sin(deg2rad(cAngleGen));
hingeIcrY = -l*r*cos(deg2rad(cAngleGen))+r;
hingeIcrX1 = -l*r1*sin(deg2rad(cAngleGen));
hingeIcrY1 = -l*r1*cos(deg2rad(cAngleGen))+r1;
```

```
hingeIcrX2 = -1*r2*sin(deg2rad(cAngleGen));
hingeIcrY2 = -1*r2*cos(deg2rad(cAngleGen))+r2;
subplot(1,2,2); %Figure 2
%title('ICR Comparison')
plot(0, 0, 'o');
fplot(hingeIcrX, hingeIcrY, [thetaMin thetaMax], 'r')
fplot(hingeIcrX1, hingeIcrY1, [thetaMin thetaMax], 'c')
fplot(hingeIcrX2, hingeIcrY2, [thetaMin thetaMax], 'g')
fplot(x1, y1, [thetaMin thetaMax], 'b')
lgnd = legend ('single-axis joint ICR', 'double-hinge gear joint ICR r = 2mm',↙
'double-hinge gear joint ICR r = 4.5mm','double-hinge gear joint ICR r =↙
7mm','biological ICR');
legend('boxoff');
set(lgnd,'color','none');
%Extract axes handles of all subplots from the figure
axesHandles2 = findobj(get(fig2,'Children'), 'flat','Type','axes');
%Set the axis property to square
axis(axesHandles2,'square')

%% Simulation of External Knee Joint Design Based on Normal Motion
%generate third figure window
fig3 = figure;
xDiff = 10;
yDiff = -70;
d = sqrt((abs(xDiff))^2+(abs(yDiff))^2); %distance from ICR to arbitrary point
thetaArb = abs(rad2deg(atan(xDiff/yDiff))); %angle between d12 and y-axis
xArb = x1 + d*sin(deg2rad(thetaArb - theta));
yArb = y1 - d*cos(deg2rad(thetaArb - theta));
subplot(1,2,1); %Figure 1
    hold on
    xlabel('Anterior-posterior axis [mm]')
    ylabel('Proximal-distal axis [mm]')
    %title('Simulation of External Knee Joint Design Based on Normal Motion')
    axis([-80 30 -80 30]) %scale
    fplot(x1, y1, [thetaMin thetaMax], 'b') % plot ICR
    fplot(xArb, yArb, [thetaMin thetaMax], 'r') % plot arbitrary point
    grid on
    lgnd3 = legend ('ICR', 'Point on Tibial Component x = 10mm y = -70mm');
    legend('boxoff');
    set(lgnd3,'color','none');
subplot(1,2,2); %Figure 2
    hold on
    xlabel('Anterior-posterior axis [mm]')
    ylabel('Proximal-distal axis [mm]')
    %title('Simulation of Joint with No Misalignment')
    axis([-80 30 -80 30]) %scale
    fplot(x1, y1, [thetaMin thetaMax], 'b') % plot ICR
    fplot(xArb, yArb, [thetaMin thetaMax], 'k') % plot arbitrary point
    grid on
```

```
    lgnd4 = legend ('ICR', 'Point on Tibial Component x = 10mm y = -70mm');
    legend('boxoff');
    set(lgnd3,'color','none');

%Extract axes handles of all subplots from the figure
axesHandles3 = findobj(get(fig3,'Children'), 'flat','Type','axes');
%Set the axis property to square
axis(axesHandles3,'square')

%% Simulation of Misalignment Limits
%generate fourth figure window
fig4 = figure;
%Max x - cyan
    x1Diff_test1 = 124; %location of pin 1 wrt origin
    y1Diff_test1 = 80;
    dbl_test1 = sqrt((abs(x1Diff_test1))^2+(abs(y1Diff_test1))^2); %distance from↙
origin to pin
    theta1_test1 = abs(rad2deg(atan(y1Diff_test1/x1Diff_test1)));
    x_test1 = x1 + dbl_test1*cos(deg2rad(theta1_test1 - theta));
    y_test1 = y1 + dbl_test1*sin(deg2rad(theta1_test1 - theta));
%Max y - red
    x1Diff_test2 = 30; %location of pin 1 wrt origin
    y1Diff_test2 = 150;
    dbl_test2 = sqrt((abs(x1Diff_test2))^2+(abs(y1Diff_test2))^2); %distance from↙
origin to pin
    theta1_test2 = abs(rad2deg(atan(y1Diff_test2/x1Diff_test2)));
    x_test2 = x1 + dbl_test2*cos(deg2rad(theta1_test2 - theta));
    y_test2 = y1 + dbl_test2*sin(deg2rad(theta1_test2 - theta));
%Min x - black
    x1Diff_test3 = -127; %location of pin 1 wrt origin
    y1Diff_test3 = -75;
    dbl_test3 = sqrt((abs(x1Diff_test3))^2+(abs(y1Diff_test3))^2); %distance from↙
origin to pin
    theta1_test3 = abs(rad2deg(atan(y1Diff_test3/x1Diff_test3)));
    x_test3 = x1 - dbl_test3*cos(deg2rad(theta1_test3 - theta));
    y_test3 = y1 - dbl_test3*sin(deg2rad(theta1_test3 - theta));
%Min y - green
    x1Diff_test4 = -8; %location of pin 1 wrt origin
    y1Diff_test4 = -144;
    dbl_test4 = sqrt((abs(x1Diff_test4))^2+(abs(y1Diff_test4))^2); %distance from↙
origin to pin
    theta1_test4 = abs(rad2deg(atan(y1Diff_test4/x1Diff_test4)));
    x_test4 = x1 - dbl_test4*cos(deg2rad(theta1_test4 - theta));
    y_test4 = y1 - dbl_test4*sin(deg2rad(theta1_test4 - theta));

hold on
grid on
    %title('Evaluation of Misaligned Joint Limits')
    xlabel('Anterior-posterior axis [mm]')
```

```
    ylabel('Proximal-distal axis [mm]')
    %axis([-150 150 -150 150]) %scale
    axis([-200 200 -200 200])
    fplot(x1, y1, [thetaMin thetaMax], 'b') %ICR
    fplot(x_test1, y_test1, [thetaMin thetaMax], 'c') %path
    fplot(x_test2, y_test2, [thetaMin thetaMax], 'r') %path
    fplot(x_test3, y_test3, [thetaMin thetaMax], 'k') %path
    fplot(x_test4, y_test4, [thetaMin thetaMax], 'g') %path
    lgnd2 = legend ('ICR', 'Maximum x', 'Maximum y', 'Minimum x', 'Minimum y');
    legend('boxoff');
    set(lgnd2,'color','none');

%Extract axes handles of all subplots from the figure
axesHandles4 = findobj(get(fig4,'Children'), 'flat','Type','axes');
%Set the axis property to square
axis(axesHandles4,'square')
%% Simulation of Single-Axis Joint
%generate fifth figure window
fig5 = figure;
xArb = x1 + d*sin(deg2rad(thetaArb - theta));
yArb = y1 - d*cos(deg2rad(thetaArb - theta));
x_SA = 0 + d*sin(deg2rad(thetaArb - theta));
y_SA = 0 - d*cos(deg2rad(thetaArb - theta));
x_DH = hingeIcrX1 + d*sin(deg2rad(thetaArb - theta));
y_DH = hingeIcrY1 - d*cos(deg2rad(thetaArb - theta));

hold on
grid on
%title('Simulation of Single-Axis Joint')
xlabel('Anterior-posterior axis [mm]')
ylabel('Proximal-distal axis [mm]')
axis([-100 40 -100 40]) %scale
fplot(x1, y1, [thetaMin thetaMax], 'b') %ICR
fplot(xArb, yArb, [thetaMin thetaMax], 'k') %path
fplot(x_SA, y_SA, [thetaMin thetaMax], 'r') %path
fplot(x_DH, y_DH, [thetaMin thetaMax], 'g') %path
%lgnd5 = legend ('ICR', 'Biological Point at x = 10mm y = -70mm ', 'Point on Single-
Axis Joint at x = 10mm y = -70mm');
lgnd5 = legend ('ICR', 'Biological', 'Single-Axis Joint','Double-Hinge Gear Joint r =
4.5mm');
    legend('boxoff');
    set(lgnd5,'color','none');

%Extract axes handles of all subplots from the figure
axesHandles5 = findobj(get(fig5,'Children'), 'flat','Type','axes');
%Set the axis property to square
axis(axesHandles5,'square')
```

```
clc;
clear;
%%NO MISALIGNMENT
%0 deg
    %read image into workspace
    im_0 = imread('0 deg.jpg');
    %KINEMATICS
        %im_0 = imrotate(im_0, 90+2.31364);
    %MOMENT ARM
        im_0 = imrotate(im_0, 90+2.95347);
    %display the image in an axes
    hIm = imshow(im_0);
%15 deg
    im_15 = imread('15 deg.jpg');
    %KINEMATICS
        %im_15 = imrotate(im_15, 90-1.30835);
    %MOMENT ARM
        im_15 = imrotate(im_15, 90+12.24369);
    %hIm = imshow(im_15);
%30 deg
    im_30 = imread('30 deg.jpg');
    %KINEMATICS
        %im_30 = imrotate(im_30, 90-0.26283);
    %MOMENT ARM
        im_30 = imrotate(im_30, 90+28.11620);
    %hIm = imshow(im_30);
%45 deg
    im_45 = imread('45 deg.jpg');
    %KINEMATICS
        %im_45 = imrotate(im_45, 90-0.26163);
    %MOMENT ARM
        im_45 = imrotate(im_45, 90+42.37359);
    %hIm = imshow(im_45);
%60 deg
    im_60 = imread('60 deg.jpg');
    %KINEMATICS
        %im_60 = imrotate(im_60, 90-1.05142);
    %MOMENT ARM
        im_60 = imrotate(im_60, 90+58.6061);
    %hIm = imshow(im_60);
%75 deg
    im_75 = imread('75 deg.jpg');
    %KINEMATICS
        %im_75 = imrotate(im_75, 90-0.26283);
    %MOMENT ARM
        im_75 = imrotate(im_75, 90+74.29901);
    %hIm = imshow(im_75);
%90 deg
    im_90 = imread('90 deg.jpg');
```

```
    %KINEMATICS
        %im_90 = imrotate(im_90, 90+0.5266);
    %MOMENT ARM
        im_90 = imrotate(im_90, 90+88.97238);
    %hIm = imshow(im_90);
%105 deg
    im_105 = imread('105 deg.jpg');
    %KINEMATICS
        im_105 = imrotate(im_105, 90+1.04661);
    %MOMENT ARM
        %im_105 = imrotate(im_105, 180+16.55036);
    %hIm = imshow(im_105);
%120 deg
    im_120 = imread('120 deg.jpg');
    %KINEMATICS
        %im_120 = imrotate(im_120, 90+2.35595);
    %MOMENT ARM
        im_120 = imrotate(im_120, 180+29.13056);
    %hIm = imshow(im_120);
```

```
clc;
clear;
%%WITH MISALIGNMENT
%0 deg
    %read image into workspace
    im_0 = imread('M 0.jpg');
    %KINEMATICS
       %im_0 = imrotate(im_0, 90-8.02006);
    %MOMENT ARM
       im_0 = imrotate(im_0, 90-2.35595);
    %display the image in an axes
    hIm = imshow(im_0);
%15 deg
    im_15 = imread('M 15.jpg');
    %KINEMATICS
        %im_15 = imrotate(im_15, 90-3.77491);
    %MOMENT ARM
        im_15 = imrotate(im_15, 90+13.19895);
    %hIm = imshow(im_15);
%30 deg
    im_30 = imread('M 30.jpg');
    %KINEMATICS
        %im_30 = imrotate(im_30, 90-1.89790);
    %MOMENT ARM
        im_30 = imrotate(im_30, 90+27.52189);
    %hIm = imshow(im_30);
%45 deg
    im_45 = imread('M 45.jpg');
    %KINEMATICS
        im_45 = imrotate(im_45, 90-3.44188);
    %MOMENT ARM
        %im_45 = imrotate(im_45, 90+38.91147);
    %hIm = imshow(im_45);
%60 deg
    im_60 = imread('M 60.jpg');
    %KINEMATICS
        %im_60 = imrotate(im_60, 90-3.03838);
    %MOMENT ARM
        im_60 = imrotate(im_60, 90+55.56101);
    %hIm = imshow(im_60);
%75 deg
    im_75 = imread('M 75.jpg');
    %KINEMATICS
        %im_75 = imrotate(im_75, 90-4.94497);
    %MOMENT ARM
        im_75 = imrotate(im_75, 90+69.41209);
    %hIm = imshow(im_75);
%90 deg
    im_90 = imread('M 90.jpg');
```

```
    %KINEMATICS
        %im_90 = imrotate(im_90, 90-5.74875);
    %MOMENT ARM
        im_90 = imrotate(im_90, 90+85.39370);
    %hIm = imshow(im_90);
%105 deg
    im_105 = imread('M 105.jpg');
    %KINEMATICS
        %im_105 = imrotate(im_105, 90-6.90869);
    %MOMENT ARM
        im_105 = imrotate(im_105, 180+9.55164);
    %hIm = imshow(im_105);
%120 deg
    im_120 = imread('M 120.jpg');
    %KINEMATICS
        %im_120 = imrotate(im_120, 90-3.77491);
    %MOMENT ARM
        im_120 = imrotate(im_120, 180+24.01755);
    %hIm = imshow(im_120);
```